MAGNETIC RESONANCE MOLECULAR IMAGING

USING IRON OXIDE NANOPARTICLES

A Dissertation
Presented to
The Academic Faculty

by

Omar Zurkiya

In Partial Fulfillment
of the Requirements for the Degree
Doctor of Philosophy in the
Department of Biomedical Engineering

Georgia Institute of Technology
December 2006

MAGNETIC RESONANCE MOLECULAR IMAGING

USING IRON OXIDE NANOPARTICLES

Approved by:

Dr. Xiaoping Hu, Advisor
Department of Biomedical Engineering
Georgia Institute of Technology

Dr. Gang Bao
Department of Biomedical Engineering
Georgia Institute of Technology

Dr. Niren Murthy
Department of Biomedical Engineering
Georgia Institute of Technology

Dr. John Oshinski
Department of Radiology
Emory University School of Medicine

Dr. Diego Martin
Department of Radiology
Emory University School of Medicine

Date Approved: October 4th, 2006

ACKNOWLEDGEMENTS

I would like to thank all of my many collaborators at Georgia Tech and Emory University who have made this experience so enriching. In particular, Drs. Gang Bao, Leslie LaConte, and Nitin Nitin were instrumental throughout my time at Georgia Tech. They are responsible for designing the experimental coating protocols and performing the synthesis of the nanoparticles described in Chapter 2. Dr. Anthony Chan at Yerkes National Primate Research Center was our primary collaborator in the magnetosome project described in Chapter 4, and of course, my advisor Xiaoping Hu, and everyone at the Biomedical Imaging Technology Center were important in all aspects of this work. Katrina Gourdet at Emory University deserves a special mention for her support to me and everyone in our lab. Finally, I would like to thank my parents and Delphine for their continuing support and patience throughout all these many years of study and preparation for what I hope will be a long and exciting career.

TABLE OF CONTENTS

LIST OF TABLES

LIST OF FIGURES

LIST OF SYMBOLS

μ	magnetic moment
ω	frequency
B_0	main magnetic field of MRI system
B_1	radio frequency field of MRI system
D	diffusion constant
Gd	gadolinium
r1	longitudinal relaxivity (units of $time^{-1} \cdot concentration^{-1}$)
r2	transverse relaxivity (units of $time^{-1} \cdot concentration^{-1}$)
R1	longitudinal relaxation rate
R2	transverse relaxation rate
T	Tesla
T1	longitudinal relaxation constant
T2	transverse relaxation constant
TE	echo time
TR	repetition time
W	weight fraction

LIST OF ABBREVIATIONS

CLIO	cross-linked iron oxide
CPMG	Carr-Purcell-Meiboom-Gill
DLS	dynamic light scattering
GFP	green fluorescent protein
MION	monocrystalline iron oxide
mMION	micelle-coated MION
MPS	mononuclear phagocyte system
MRI	magnetic resonance imaging
MT	magnetization transfer
ORS	off-resonance saturation
PEG	polyethylene glycol
SPIO	superparamagnetic iron oxide
USPIO	ultrasmall superparamagnetic iron oxide

SUMMARY

Magnetic resonance imaging (MRI) is regularly used to obtain anatomical images that have greatly advanced biomedical research and clinical health care today, but the full potential of MRI in providing functional, physiological, and molecular information is only beginning to emerge. The goal of magnetic resonance molecular imaging is to further understand and develop approaches to MRI to acquire information on the molecular level. This work is focused on ways to enhance the effect of iron oxide based nanoparticles on the MR signal, to study alternative approaches to generating contrast with superparamagnetic iron oxide nanoparticles (SPIO), and to develop a genetic marker for MRI which results in the biological production of magnetic nanoparticles. The work presented in this dissertation is divided into three main sections:

Elucidation of the contribution of size and coating properties to magnetic nanoparticle induced proton relaxation.

In order to maximize the contrast generated from such particles without increasing their size, new methods to increase their effect on relaxivity must be developed. Experimental data obtained on a new class of biocompatible particles are presented, along with simulated data. The effects on relaxivity of coating size, proton exchange, and altered diffusion are examined. Simulations are presented confirming the effect of particle coatings on clustering-induced relaxivity changes, and an experimental system demonstrating the clustering effect is presented.

Development of a diffusion-dependent, off-resonance imaging protocol for magnetic nanoparticles.

This work demonstrates an alternative approach, termed off-resonance saturation (ORS), for generating contrast sensitive to SPIO nanoparticles. This method leads to a calculated contrast that increases with SPIO concentration. Experimental data demonstrate that in the presence of these particles, an off-resonance effect exists, that is distinct from the magnetization transfer (MT) effect, and is highly dependent on diffusion. Data show that the dependence on water diffusion becomes most significant at rates of 0.5×10^{-9} m^2/s and slower. The dependence of the off-resonance effect on off-resonance frequency and particle concentration are also investigated. The data suggest a useful frequency offset range of 500 Hz < $|\Delta\omega|$ < 1500 Hz at 3T. This approach may be especially useful in organs and diseases in which diffusion may be altered by pathologies.

Development of a genetic MRI marker via in vivo magnetic nanoparticle synthesis

This work seeks to provide a gene expression marker for MRI based on bacterial magnetosomes, tiny magnets produced by naturally occurring magnetotactic bacteria. Here, *magA* is expressed in a commonly used human cell line, 293FT, resulting in the production of magnetic, iron oxide nanoparticles by these cells. MRI shows that these particles can be formed *in vivo* utilizing endogenous iron and can be used to visualize cells positive for *magA*. These results demonstrate that *magA* alone is sufficient to produce magnetic nanoparticles and that it is an appropriate candidate for an MRI reporter gene.

CHAPTER 1

INTRODUCTION

Magnetic resonance imaging (MRI) is regularly used to construct an image based on the intrinsic contrast provided from the relaxation of spin of hydrogen atoms. These images provide an accurate anatomical picture that has greatly advanced health care today. Clinically, the images produced by MRI are invaluable, but the full potential of using MRI in acquiring functional, physiological, and molecular information is only beginning to be realized. The goal of this work is to further understand and develop approaches to magnetic resonance imaging to acquire information on the molecular level, a field termed molecular imaging.

Molecular imaging refers to the study of cellular and molecular events through noninvasive investigation [1]. Bringing molecular imaging to MRI requires generating contrast specific to information on the molecular level that is also sensitive enough to be observed at the voxel level. Gadolinium ion-based contrast agents are required to be present in relatively high concentrations, on the order of millimoles. Targeted *in vivo* imaging with MRI, however, often requires contrast agent compounds to be effective at concentrations on the order of 10 μM [2]. It is therefore desirable to obtain contrast agents in which a small number of bindings to targets will be sufficient to generate contrast. Iron oxide nanoparticles provide the possibility of detection at the single particle

level [3]. These particles, however, are at the micrometer size. Such large particles are likely to interfere with normal cellular processes limiting their application to cellular and molecular imaging. It is therefore important to devise methods for imaging small particles, on the order of nanometers in size. This is especially important for intracellular studies.

Here we will begin by looking at contrast in MRI. The parameters described that are responsible for generating the intrinsic contrast between tissues in MRI are the same parameters affected by synthetic contrast agents. This will help to understand the mechanism of contrast agents and the reason superparamagnetic iron oxide nanoparticles are an appropriate choice for molecular imaging.

Following this chapter, Chapter 2 will discuss studies involving synthetic nanoparticles and the effect of their coatings on relaxivity. Chapter 3 will discuss an alternative approach to imaging with superparamagnetic particles utilizing off-resonance saturation, and Chapter 4 will discuss the development of an MRI reporter gene, *magA*, that can be used to enable cells to produce iron oxide nanoparticles capable of causing a contrast in the MR image.

Contrast in MRI

The principles of MRI follow from the same principle of exciting spins as found in nuclear magnetic resonance (NMR) [4, 5]. In most cases, the MRI machine is tuned to image the most abundant spin population found in the body, that of the protons of bulk water. Contrast in MRI arises from the difference in signal in adjacent pixels or voxels due to three basic parameters, spin density, T1, and T2 (Figure 1.1). The spin density, proportional to M_0, reflects the total number of spins available to be imaged within a given tissue (or pixel). The system of spins is excited by radiofrequency (RF) energy, followed by a period of spatial encoding and then a period of signal acquisition during which the spin system is emitting energy as it relaxes to its equilibrium state. This energy is received as the signal for the MRI image.

The signal therefore depends not only on the spin density, but also upon two decay parameters, T1 and T2, which describe the rates at which the spin system is changing. T1 is rate at which the system returns to equilibrium following excitation by RF energy. The faster the system returns to equilibrium, the more spins available to be excited by the next imaging pulse. The effect of T1 on the signal is indicated in Figure 1.1b. For a given amount of time, a pixel with a shorter T1 would result in greater signal.

T2, often called spin-spin relaxation, refers to decay time of the signal received. During signal acquisition, the effect of field inhomogeneity, mostly arising from nearby spins affecting each other, causes the coherence of the signal to be lost. This decay rate is

indicated in Figure 1.1c where, for a given amount of time, a pixel with a shorter T2 would result in less signal compared to an identical pixel in which all other parameters were the same.

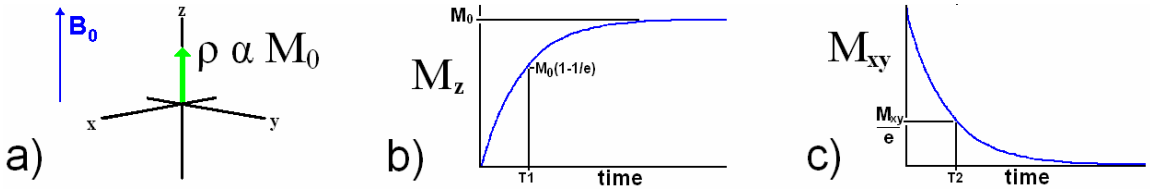

Figure 1.1: Three basic parameters of MRI. a) The spin density, proportional to M_0, is related to the net amount of spins aligned along the main magnetic field, b) a T1 curve indicating that shorter T1 times result in a quicker return to the equilibrium state, resulting in a greater magnetization available for imaging, **c)** a T2 curve indicating that shorter T2 times result in a quicker loss of signal in the transverse plane, resulting in a lower received signal.

Putting these parameter together results in the most basic signal equation:

$$S \propto M_0(1-e^{-\frac{TR}{T1}})e^{-\frac{TE}{T2}} \qquad (1.1)$$

Here, TR is the repetition time and TE is the echo time of the imaging pulse sequence. This equation represents the effects described above. The signal (S) is

proportional to spin density (M_0). It is increased by a shorter T1 and decreased by a shorter T2. By choosing TR and TE carefully, images can be chosen to favor T1, T2 or spin density weighting. Table 1.1 shows the decay rates of several tissues at 1.5T and 37°C. The well-known utility of MRI in imaging soft tissue arises from the natural differences in decay rates of various tissues, as in the case of brain imaging where gray and white matter can be easily distinguished. Figure 1.2 shows some examples of the various weighting of typical MRI images.

Table 1.1: Typical decay rates for tissues at 1.5T and 37°C. R1≡1/T1, R2≡1/T2. (data from ref. [5])

Tissue	T1 (ms)	R1 (s^{-1})	T2 (ms)	R2 (s^{-1})
gray matter	950	1.05	100	10
white matter	600	1.67	80	12.5
Muscle	900	1.11	50	20
cerebrospinal fluid (CSF)	4500	0.22	2200	0.45
Fat	250	4.00	60	16.67
Blood	1200	0.83	100-200	5-10

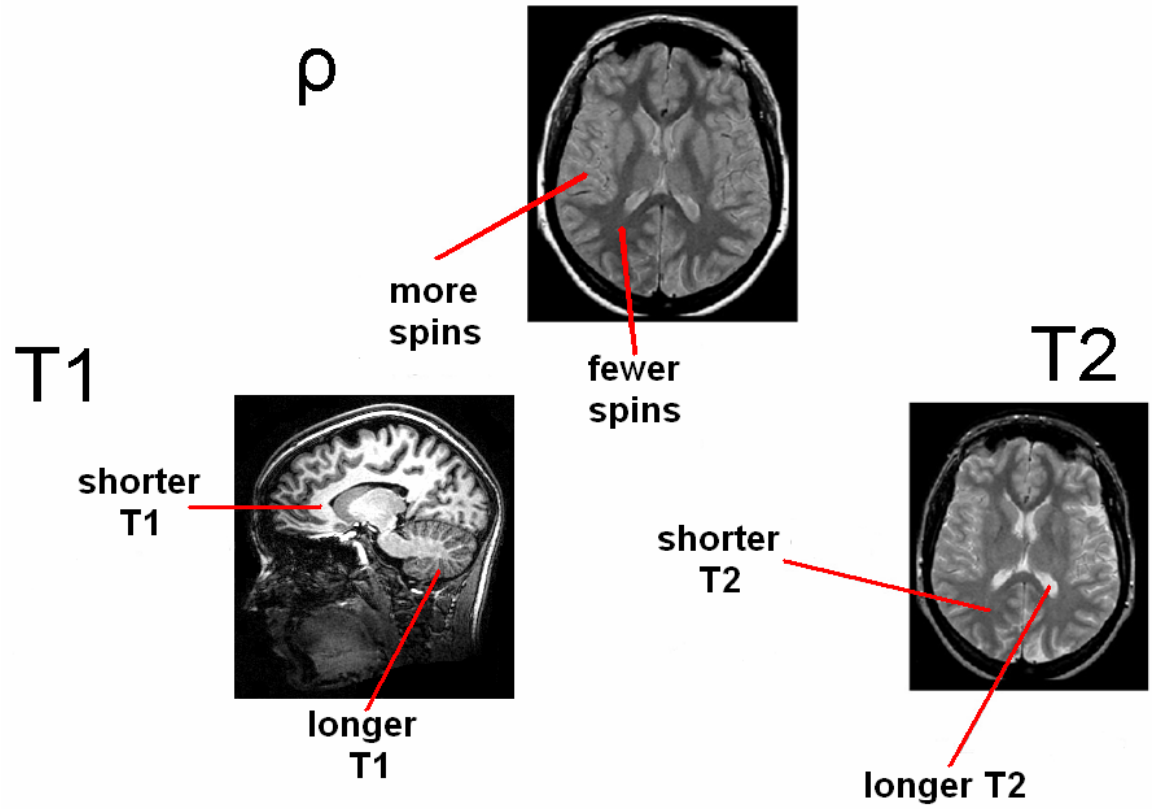

Figure 1.2: Examples of images obtained with different MRI weighting approaches. Spin density images show brighter pixels in correlation with increased presence of spins. T1 weighting, brings out differences in white and grey matter (see T1 times in Table 1.1) where white matter, with the shorter T1, appears brighter. T2 weighting allows fluids, such as cerebrospinal fluid, to appear bright due to the long T2.

Since these are the basic parameters of contrast in the MR image, it is these parameters that should be altered by any potential contrast agent. The most common MR contrast agents are paramagnetic gadolinium ion complexes and superparamagnetic iron

oxide particles (see Table 1.2). Gadolinium contrast agents are used primarily for their ability to shorten T1, although at high concentrations, they can have significant effects on T2 as well. Iron oxide agents, on the other hand, have less effect on T1 and are used primarily for their effect on T2. Based on equation 1.1, it can be seen that gadolinium enhanced T1 imaging would show bright pixels in locations where contrast is present, and iron oxide enhanced T2 imaging would show decreased signal where contrast agent is present. In either case, it is the contrast with adjacent pixels that is the desirable effect.

In practice today, these contrast agents are non-specific. They are taken up into tissues based on passive biodistribution. Oral agents are useful for picturing bowel, and organs that filter the blood such as the liver and kidneys, have high concentrations of contrast when agents are injected intravenously. In order to extend the use of contrast agents to other, specific tissues, it is necessary to develop targeted probes. Such probes have the advantage of targeting and delineating areas of specific molecular activity on an MR image. For instance, in clinical procedures, an anatomical image revealing a mass would be routinely biopsied. If, however, there were a way to deliver a contrast agent that is only activated under specific, controlled circumstances, such as the expression of a carcinogenic genotype, one could obtain an image that provides molecular, as well as anatomical information. The need for biopsy would be reduced. This example represents a great advancement in clinical diagnosis, yet it represents a relatively modest goal of the potential such research could provide.

Table 1.2: Relaxivity values of common contrast agents. Gadolinium-based agents are generally used for their ability to shorten T1, while iron oxide based agents are generally used for their effect on T2. (data from ref. [6])

MR Contrast Agent	Main use	Molecular weight or particle size	Relaxivity (mM s)-1	Target
Gd-DTPA	T1-agent	0.6 kDa	r1= 3.7	Extracellular
Dextran-Gd-DTPA	T1-agent	75 kDa	r1= 11	Blood-pool
Carboxydextran-coated SPIO SHU-555	T2-agent	62 nm	r1= 12 r2= 188 (0.94T)	Capillary permeability
Dextran-coated SPIO AMI-25	T2-agent	58 nm	r1=24 r2= 107 (0.47T)	MPS organs (liver)
Dextran-coated USPIO MION-46L	T2-agent	18-24 nm (CLIO 30-40 nm)	r1= 16 r2= 35 (0.47T)	MPS organs
Dextran-coated USPIO AMI-227	T2-agent	17-20 nm	r1=23 r2= 53 (0.47T)	Lymph nodes
MION-encapsulated liposomes	T2-agent	170-300 nm	r1= 23 r2= 130 (0.47T)	MPS organs (liver)
PEGylated magnetoliposomes	T2-agent	40 nm	r1= 3 r2= 240 (1.5T)	Bone marrow
(Protein-coated) magnetoferritin	T2-agent	12 nm	r1= 8 r2= 218 (1.5T)	Blood-pool

Targeted imaging applications raise the need for development of new contrast agents capable of being detected at low concentrations. Successful *in vivo* imaging with

MRI often requires target concentrations on the order of 10 μM [2]. In these applications, the contrast agent molecule is conjugated to the ligand which will bind the target, meaning the contrast agents must be effective at micromolar concentrations. The ability to use gadolinium for molecular imaging applications is therefore limited by its need to be present in millimolar quantities in order to cause a visible contrast. In Table 1.2, it can be seen that the r1 of gadolinium agents is on the order of tens of mM^{-1} s^{-1} (3.7-11 mM^{-1} s^{-1}), whereas for superparamagnetic iron oxide nanoparticles (SPIO), the r2 is larger, on the order one to two hundred mM^{-1} s^{-1}. The effect of SPIO nanoparticles is further magnified by the fact that these values are cited for mM Fe, but each nanoparticle contains several thousand iron atoms. Therefore, the relaxivity per particle is amplified by this factor, allowing SPIO to be an effective contrast agent even when molecular targets are present at low, micromolar concentrations.

Molecular Imaging

Molecular imaging, in general, refers to the study of cellular and molecular events through noninvasive investigation [1]. In MRI, molecular imaging is dependent on induced changes in proton relaxivity on the molecular and cellular level. Bringing molecular imaging to human MRI requires generating contrast on the molecular level that is not only specific, but also sensitive enough to be observed at the voxel level. MRI scanners at 3 Tesla, the current state of the art in human clinical scanning, offer submillimeter resolution. Although this resolution provides for detailed anatomical pictures, it presents challenges for molecular imaging. Probes must be able to generate contrast by specific molecular mechanisms, yet the change in signal must be large enough to be visible on the voxel level.

Over the last decade, biocompatible iron oxide particles have been linked to specific ligands for targeted molecular imaging applications [7-11]. However, due to their relatively large size and clearance by the reticuloendothelial system (RES), there is still a lack of widespread biomedical molecular application. Imaging of macrophage activity remains the most significant application, particularly for tumor staging of the liver and lymph nodes, and several commercial products are either approved or in clinical trials. Labeling non-phagocytic cells in culture using modified particles, followed by transplantation or transfusion in living organisms, has led to an active research interest to monitor cellular biodistribution *in vivo*, including cell migration and trafficking. While most of these studies have been more focused on establishing techniques, further use of

these approaches will be as tools to obtain deeper insights into the dynamics of *in vivo* cell biology and at monitoring therapies that are based on the use of stem cells and progenitors.

In order to tackle the various aspects of this problem, this work is divided into three main goals in developing a molecular imaging approach for MRI:

Elucidation of the contribution of size and coating properties to magnetic nanoparticle induced proton relaxation.

In order to maximize the contrast generated from magnetic nanoparticles without increasing their size, new methods to increase their effect on relaxivity must be developed. Experimental data obtained on a new class of biocompatible particles are presented, along with simulated data. The effects on relaxivity of coating size, proton exchange, and altered diffusion are examined with the goal of increasing proton relaxivity so that maximum contrast can be generated from small particles without increasing core size.

An important feature of targeted contrast agents for MRI is a controllable switching mechanism in which contrast agents are "activated" by a specific molecular interaction. In MRI, clustering of particles can have a significant effect on relaxivity [12]. The clusters must alter the MR signal in a way that is identifiable against a background of

unclustered particles. Simulations are presented showing the influence of particle coatings on clustering-induced relaxivity changes, and an experimental system demonstrating the clustering effect is presented. This work helps to advance this concept by exploring ways to maximize the effect of clustering on the MR signal. This ensures classification of clustering events, or "positive" identification is reliable, efficient, and quantifiable.

Development of a diffusion-dependent, off-resonance imaging protocol for magnetic nanoparticles.

Currently, superparamagnetic contrast agents are used for their effect on T2 or T2*. This results in a negative contrast, or a darkening in the resulting the image. Signal voids, however, can be caused for many reasons including field inhomogeneities and susceptibility-induced artifacts such as those at tissue interfaces. These issues make identification of positively labeled cells inconclusive. At high main magnetic field strengths, which are becoming clinical standards, the sensitivity to susceptibility-induced artifacts from such macroscopic field inhomogeneities is increased. Because the particles cause local field inhomogeneities, it is possible, by applying off-resonance irradiation, to exploit the effect of field inhomogeneity as an alternative contrast mechanism for these agents.

This work demonstrates an alternative approach, termed off-resonance saturation (ORS), for generating contrast sensitive to SPIO nanoparticles. This method leads to a calculated contrast that increases with SPIO concentration. Experimental data demonstrate that in the presence of these particles, an off-resonance effect exists, that is distinct from the magnetization transfer (MT) effect, and is highly dependent on diffusion. Data show that the dependence on water diffusion becomes most significant at rates of 0.5×10^{-9} m^2/s and slower. The dependence of the off-resonance effect on off-resonance frequency and particle concentration are also investigated. The data suggest a useful frequency offset range of 500 Hz < $|\Delta\omega|$ < 1500 Hz at 3T. This approach may be especially useful in organs and diseases in which diffusion may be altered by pathologies.

Development of a genetic MRI marker via in vivo magnetic nanoparticle synthesis

One major application SPIO nanoparticles is the *in vivo* tracking of cells, where cells are labeled in culture using modified particles, followed by transplantation or transfusion in living organisms. A limitation of this approach is the need to label cells *in vitro* with pre-synthesized nanoparticles prior to cell transplant. As a result, particle concentration within cells decreases over time as the cells grow, migrate, and divide, and particles cannot be readily linked directly to *in vivo* gene expression. One way to overcome this is to utilize a genetic approach. Green fluorescent protein (GFP) is perhaps the most well-known genetic marker for optical imaging.

This work seeks to provide a gene expression marker for MRI based on bacterial magnetosomes, tiny magnets produced by naturally occurring magnetotactic bacteria. Here, *magA* is expressed in a commonly used human cell line, 293FT, resulting in the production of magnetic, iron oxide nanoparticles by these cells. MRI shows that these particles can be formed *in vivo* utilizing endogenous iron and can be used to visualize cells positive for *magA*. These results demonstrate that *magA* alone is sufficient to produce magnetic nanoparticles and that it is an appropriate candidate for an MRI reporter gene.

CHAPTER 2

RELAXATION BY MAGNETIC NANOPARTICLES

Background and Significance

The coupling of proton spins with larger magnetic moments increases the relaxivity of water making them useful as contrast agents for MRI. In the presence of paramagnetic substances, such as iron oxide nanoparticles, water relaxation time constants, T1, T2 and T2*, of proton nuclear spins are shortened [5]. With regard to T2 and T2*, magnetic nanoparticles act as magnetic moments producing tiny field gradients through which protons diffuse. As each proton will take a separate path through the field gradients, phase differences among protons will accumulate. The result is a susceptibility-induced dephasing of the MR proton signal and a subsequent reduction in T2. This T2 shortening can be utilized in an imaging experiment when the nanoparticles are strongly magnetized. In this condition, $\tau\Delta\omega_r>1$, where τ is half the echo time for a single Hahn spin-echo sequence (τ = TE/2) or half the interval between 180˚ pulses in a Carr-Purcell-Meiboom-Gill (CPMG) [13] sequence and $\Delta\omega_r$ is the root-mean-square angular frequency shift at the particle surface. The work here is limited to spherical particles.

The most common MR contrast agents are paramagnetic gadolinium ion complexes and superparamagnetic iron oxide particles. Relaxation is caused by a time-

modulated interaction between the protons and the magnetic moment [4]. Coupling may be of dipolar and scalar nature, while time modulation arises from translational diffusion of the protons, rotational diffusion of the magnetic compound, and exchange of protons between binding sites and free water.

Currently, theories predicting T2 shortening by paramagnetic ions magnetic nanoparticles can be divided into two groups: inner sphere (IS) and outer sphere (OS) models [14]. Inner sphere theory accounts for the exchange between coordinated water molecules and bulk water. Outer sphere theory describes the relaxation induced by the diffusion of water molecules within the magnetic field gradients around the paramagnetic hydrated ion. The IS contribution consists of protons physically interacting with the paramagnetic ion. In this scenario, the distance between the ion and the coordinated water molecule is on an average smaller than that between the hydrated ion and a diffusing water molecule in the OS model. Additionally, coordinated protons reside on the binding site longer, exposing them to the magnetic ion for a longer time than in the case of the diffusing proton in the OS model. As a result, the IS contribution is generally larger than that of OS. However, for chelated ions and in the absence of water exchange, the OS mechanism dominates relaxation.

Relaxation induced by magnetite (Fe_3O_4) particles is generally attributed to the diffusion of water molecules around the superparamagnetic iron core. It can be generally described by an OS theory adapted to account for the anisotropy of magnetite crystals [15, 16]. The application of IS versus OS theories can be mathematically determined by

the criterion $\tau_D \Delta\omega_r$, where $\tau_D = r^2/D$ (r is the particles radius, D is the water diffusion coefficient, and ω_r is the rms angular frequency shift at the particle surface). For $\tau_D \Delta\omega_r < 1$, a motional-averaging regime is satisfied. The relaxation rate is then given by quantum-mechanical outer sphere theory:

$$1/T_2 = (4/9) v \tau_D (\Delta\omega_r)^2 \qquad (2.1)$$

where v is the volume fraction occupied by the nanoparticles. For $\tau_D \Delta\omega_r > 1$, a static dephasing regime is employed. This term refers to the dephasing of motionless magnetic moments but remains valid for slow motion where the dephasing experienced in a single encounter of proton and field shift amounts to larger than one radian. In this case, the relaxation rate for spherical particles is characterized by the equation:

$$1/T_2^* = \pi\sqrt{15} v \Delta\omega_r / 9 \qquad (2.2)$$

where $\Delta\omega_r$ is given by:

$$\Delta\omega_r = \sqrt{\frac{4}{5}} \gamma B_{eq} = \sqrt{\frac{4}{5}} \gamma\mu / r^3 = (8\pi/3)\gamma M / \sqrt{5} \qquad (2.3)$$

where γ is the proton gyromagnetic ratio, B_{eq} the equatorial magnetic field of the particle, μ the magnetic moment, and M its magnetization. In the case of synthetic iron oxide

nanoparticles, it is likely that a combination of processes occurs in the dephasing process. In a well-dispersed solution, protons will diffuse through magnetic gradients, accumulating a phase by $\Delta\omega = \gamma\Delta B$, where B is the magnetic field experienced by the proton due to the particle. However, at the interface between particle and water protons, it is likely that several types of events occur. Protons may physically exchange with protons in the molecules comprising the particle coating. Such interactions are generally known as chemical exchanges and have been utilized for imaging using magnetization transfer contrast (MTC) [17, 18] and in developing a class of compounds known as chemical exchange dependent saturation transfer (CEST) agents [19].

It is possible, however, that coating molecules may influence protons in ways other than direct chemical exchange. Proton diffusion may be slowed in regions near the particles due to molecular forces and in some cases, such as those of PEG-coated particles, it is possible that protons could diffuse in and out spaces between coating molecules (Figure 2.1). The result could be an effective alteration in proton diffusion around the particles resulting in a change in the nanoparticles relaxation characteristics based on specific coating properties.

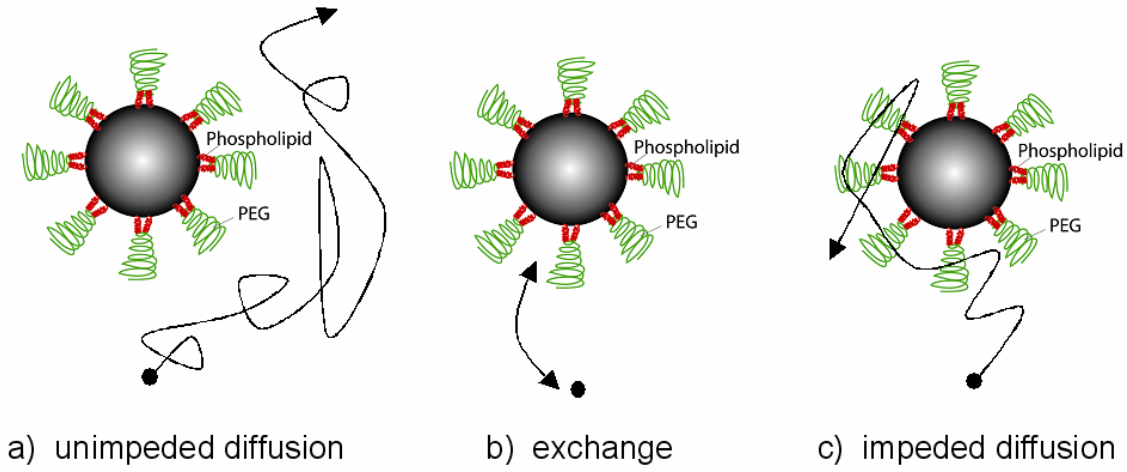

Figure 2.1: Various schemes of proton diffusion and interaction with nanoparticles and their coatings. a) diffusion of protons past the nanoparticle represent the dominant contribution in outer sphere (OS) theory, b) diffusing water protons may exchange with protons on the particle surface; the increased residence time and close proximity result in the inner sphere (IS) effect, c) diffusion may be restricted by the particle coating resulting in a scenario somewhere between OS and IS.

Present theories focus on either diffusion past a particle or chemical exchange as mechanisms for relaxation. Interaction between protons and nanoparticle coatings are not well understood, however, and could have significant influence on induced relaxation. Such interactions are not fully accounted for in present theories, and a further understanding of such influences can aid in developing more effective probes. This is especially important in *in vivo* imaging where maintaining small probe size is important and enhancing relaxation properties by simply increasing core particle size is not an option.

Superparamagnetic iron oxide nanoparticles are increasingly used in the development of MRI probes because of their effect on relaxivity [20]. These nanoparticles are already used regularly for applications such as high-density magnetic storage, catalytic and separation processes [21], and they are now playing an expanding role *in vivo* tracking of stem cells and tumor progression [22, 23], cell and DNA sorting [24], drug delivery [25] and cell mechanics studies [26].

Currently, the most common iron oxide nanoparticles for MRI are monocrystalline iron oxide nanoparticles (MION) that contain core crystals (4.6 nm diameter) of iron oxide generated in a solution of dextran. The resulting particles are soluble because of this dextran coating but have hydrodynamic diameter of 20-40 nm. Cross-linked iron oxide (CLIO) nanoparticles [27] have been developed as well for use in functionalizing the surface coating. The physiochemical properties of MION are well known [28, 29], and the surface properties of dextran-coated particles have been studied extensively [30, 31]. However, because the particles are generated at the same time the coatings are formed, there is little control over specific coating characteristics at the synthesis step. This makes these particles difficult to use in studies of proton relaxation effects since coating properties such as thickness and surface composition are difficult to alter. Therefore, it is desirable to develop particles in which the coating is formed in a separate, controllable process from the core crystallization.

Studies of a polyethylene-glycol coated magnetic nanoparticle

A variety of *in situ* and post-synthesis coating strategies have been developed for stabilization of magnetic nanoparticles. Post-synthesis coating processes include using monolayer ligand [32, 33], polymer [34, 35] and silica coatings [36-38]. The monolayer ligand coatings rely on effective adsorption or chemisorption of the ligand on the surface of the nanoparticle. These coatings tend to have limited colloidal stability, limited flexibility for functionalization, and the tendency to form incomplete coatings due to residual surfactant on the surface. The polymer- and silica-based coating processes are difficult to control, often resulting in multilayered coatings and multiple nanoparticles in the same encapsulation [37]. *In situ* coating approaches such as that with dextran [39] often lead to multilayered coatings, which can result in a heterogeneous size distribution. This can make quantification of clustering effects on relaxation unreliable. *In situ* synthesis conditions also limit the variety of functionalization methods that can be achieved.

In preparation for the long-term application of molecular imaging probes, experiments were conducted to produce particles with appropriate characteristics for *in vivo* delivery. One challenge of this application is to develop magnetic nanoparticle probes with a size comparable to the target proteins and nucleic acids (~2-15 nm). To facilitate cellular delivery and specific intracellular targeting, these particles need both a probe portion and targeting ligands on their surface. Such probes can then be used to generate an intracellular MRI contrast for cell tracking purposes. More sophisticated

probes can be designed to generate contrast based on molecular specificity through clustering of magnetic nanoparticles or other molecular switch mechanisms [40]. A critical step in developing such molecular probes is to functionalize the nanoparticles with a biocompatible coating.

In collaboration with Dr. Gang Bao (Dept. of Biomedical Engineering, Georgia Tech), functionalized magnetic nanoparticles for intracellular delivery were developed and tested for relaxation characteristics [41]. Specific coating and experimental protocols for the design and synthesis of these particles were developed by Drs. Gang Bao, Leslie LaConte and Nitin Nitin in this collaboration. These particles are water-soluble, monodispersed, biocompatible, and easily adaptable for multifunctional bioconjugation of probes and ligands. In this approach, superparamagnetic monocrystalline iron oxide nanoparticles (MIONs) are encapsulated in a PEG-modified phospholipid micelle structure. Similar encapsulation strategies have been used for various hydrophobic drug molecules and more recently, quantum dots [42]. The key principle of this coating procedure is to exploit the hydrophobic nature of the nanoparticle surface, which arises from residual synthesis surfactant. The hydrophobic portion of an amphiphilic structure such as the PEG-phospholipid used here interacts with the nanoparticle surface to create micelles, resulting in a self-assembled monolayer coating on the nanoparticle surface. The PEG portion of the molecule allows the MIONs to be soluble and biocompatible. The use of modified PEG molecules allows for bioconjugation [43] of protein or nucleic acid probes and multiple ligands. The magnetic iron oxide (Fe_3O_4) nanoparticle (MIONs) cores were provided by Dr. Charles O'Connor (University of New Orleans) and had an

average size of 6.6 nm with a size distribution of 11%, as determined by transmission electron microscopy. Specific coating protocols are described in [41].

Dynamic light scattering (DLS) was used to determine the size of the micelle-coated MIONs (mMIONs) using a DynaPro-LSR instrument (Protein Solutions, England) (Figure 2.2a). The average hydrodynamic radius of the mMIONs was 7.34 nm ± 0.71 nm (93.9% of mass). The size distribution as a function of % mass is shown in Figure 2.2a and is in agreement with results obtained by [42] for micelle-encapsulated quantum dots. DLS results also indicate a narrow range of polydispersity in mMIONs. The precise size range may provide a crucial advantage for imaging applications based on clustering of magnetic nanoparticles, as discussed below.

Electron microscopy was performed (Figure 2.2b) to verify the presence of coating and size of resultant particles. Negative staining revealed a dark iron core with an unstained micelle coating around the MIONs. The diameter of mMIONs as determined by this method is 12-14 nm, similar to results obtained by DLS. Some fraction of micelles without iron cores were also observed in the EM images and ultracentrifugation may be useful in the future to separate empty micelles from mMIONs. To determine concentration of Fe, a colorimetric assay using o-phenanthroline was carried out and Fe concentration after the coating procedure was determined to be 168 μg/ml.

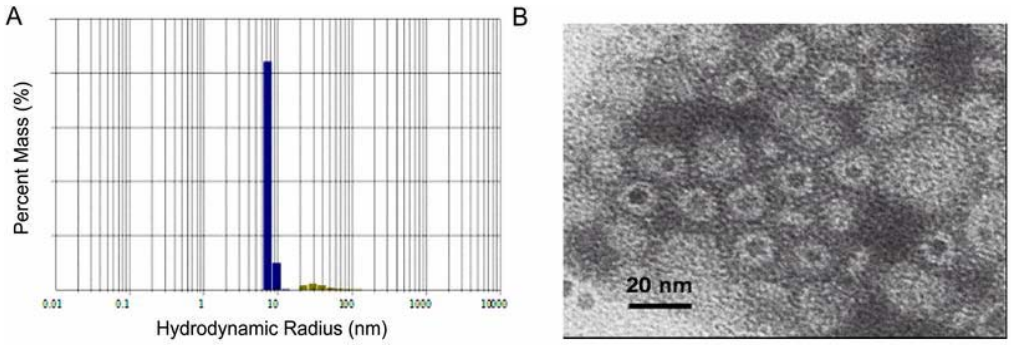

Figure 2.2: Characterization of mMIONs. a) Particle size distribution [% mass vs. hydrodynamic radius (nm) of particles] of mMIONs measured using dynamic light scattering. 93.9% of the sample mass has a hydrodynamic radius of 7.34 nm. b) Electron micrograph of negatively stained mMIONs at a magnification of 60,000 x. Dark iron cores can be seen encircled by unstained micellar coating against the stained carbon grid background. (With kind permission of Springer Science and Business Media from [41], fig.2, p709, © SBIC 2004)

A 0.47 T Bruker Minispec Analyzer MQ20 was used for T2 measurements. MDBK cells (derived from bovine kidney) were grown in culture and incubated with mMIONs and media. After incubation, cells were washed with PBS to remove extracellular and unbound mMIONs. Cells were collected in a final volume of 1.5 ml of media. 500 μl of this cell suspension were placed in a 10 mm sample tube for T2 measurements using the CPMG pulse sequence [13]. Images of cell samples were obtained on a 3T Siemens TRIO MRI system using a T2-weighted Turbo Spin Echo sequence.

Here, phospholipid-PEGs are modified with commercially available functional groups such as amines and sulfhydryls. These can be easily incorporated into micelles to coat MIONs. This provides flexibility in functionalizing the nanoparticles. To

demonstrate the ability of mMIONs to generate intracellular contrast, they were bioconjugated with the HIV Tat peptide via a reactive amine group to the surface of mMIONs for delivery into cells. The Tat peptide is known to direct intra-cellular delivery of proteins, nanoparticles, and other macromolecules [12, 44].

T2 relaxation times and MR images were obtained to validate the delivery of mMIONs into live MDBK cells. For T2 measurements, MDBK cells were incubated with Tat-mMIONs for 1 hour and then washed to remove extracellular and unbound mMIONs. A suspension of this preparation was used for T2 measurements. The T2 determined for cells with mMIONs was 623 ± 2 ms, and that for control cells without mMIONS, the T2 was 1503 ± 20 ms (see Figure 2.3a). In the mMION-treated cells, the T2 time is at least two times shorter than control cells, indicating internalization of magnetic nanoparticles. The shortened T2 time of cells with mMIONs can be visualized when imaged using a clinical MR system (Figure 2.3b), again indicating the presence of the contrast agent inside cells.

In future work, a variety of targeting mechanisms may be employed. Because their size is on the order of many intracellular biomolecules, including proteins and nucleic acid-protein complexes, these mMIONs may be suited for probing intracellular events with less interference than other currently used iron oxide-based molecular probes. The small diameter and uniform size distribution are also desirable for future work in clustering techniques. This work is a first step towards the development of more powerful intracellular molecular imaging agents.

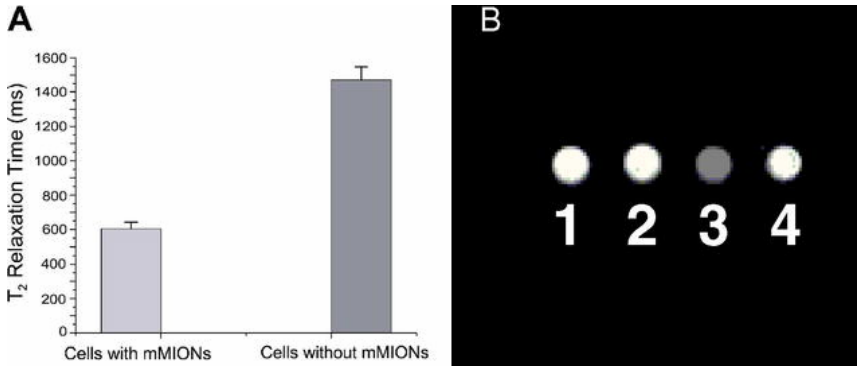

Figure 2.3: The effect of mMIONs on water relaxation inside living cells. a) T2 relaxation time (ms) measurements obtained using Bruker MQ20 Minispec. MDBK cells with mMIONs gave a T2 relaxation time of 604 ± 37 ms, while cells without mMIONs had a T2 time of 1473 ± 75 ms. b) MRI images of four different samples: (1) culture media only, (2) cells without mMIONs, (3) cells with mMIONs, (4) culture media only. Images were obtained using a 3T Siemens TRIO, turbo spin-echo, TR 4000, TE 310, in-plane pixel size 0.5 × 0.5 mm. (With kind permission of Springer Science and Business Media from [41], fig.5, p709, © SBIC 2004)

Effect of Particle Size Variation on Transverse Relaxivity

Background

There are many factors that could potentially affect the ability of the magnetic nanoparticle to induce T2 shortening. These include physical size of the particle and its coating, chemical properties of the coating and surrounding environment, motion of particles and protons, and inhomogeneities in the particles themselves. By adjusting the core size, coating thickness, surface chemistry, and targeting ligands, nanoparticle probes have been tailored to target specific organs, cells, or even molecular markers of different diseases *in vivo* [20, 45]. The relaxivity of magnetic nanoparticles has typically been modulated by their core size, often in the range of 4-20 nm in diameter [45]. There is, however, less known about the effect of coating properties on relaxivity induced by the nanoparticles. Because many of these factors can interact in complicated ways to affect relaxivity, elucidating the effect of coating properties on T2 shortening can provide a useful basis for the development of more powerful nanoparticle probes without the need for increasing probe size.

For a spherical particle of a particular core size, one can imagine field lines are distributed through space according to the dipole equation (Figure 2.4a). Here we are only concerned with the *z*-component of the field. Magnetic nanoparticles induce T2 relaxation as protons pass through these field gradients. The protons individually accumulate phase changes according to $\varphi=\gamma \cdot B_z \cdot \Delta t$ where Δt is the amount of time the proton spends in a field gradient. Since protons are initially in phase, the signal decay,

due to dephasing, occurs due to the field gradients of the particle and not the main magnetic field. In Figure 2.4a, a particle core (green) is producing a certain magnetic field through which particles may diffuse. In Figure 2.4b, the same core is surrounded by a coating, which physically excludes diffusing protons from some area around the core. Although the core produces the same field, protons have less access to the higher gradients near the particle. As a result, it is predicted that proton relaxation in the coated particle situation will be slower, leading to an observed decrease in R2 with increasing coating size.

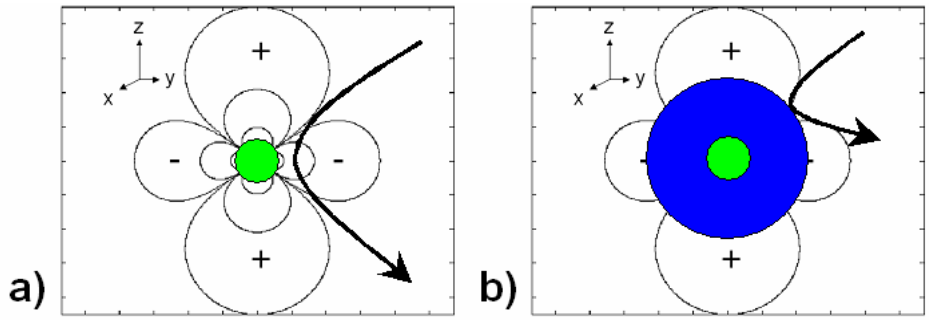

Figure 2.4: Particle coatings prevent protons from approaching the magnetic core. a) Protons diffuse through the dipole field of the nanoparticle in green. b) Due to a large coating (blue), protons cannot access space nearest the particle where the field gradients are the largest.

In most of the studies involving MIONs [32, 36, 38, 39, 46], it is not possible to independently alter the coating size without a significant change in the chemistry of the surface coating. In addition, with some of the existing coating methods, it is very difficult to obtain a narrow size distribution of coated particles. The variations in the overall size of coated particle can limit an independent analysis of the role of size and chemistry of coatings on relaxivity characteristics of MIONs, making it difficult to gain a fundamental understanding of the magnetic relaxation processes involved in contrast generation by MIONs.

In this study, micelle-based phospholipid-polyethylene glycol (PEG) coatings were used to encapsulate MIONs as described previously [41]. This coating allows control of coating thickness by simply varying the length of the PEG polymer that is on the outermost surface of the particles, while keeping both the chemical composition of the coating itself and the size of the core iron oxide nanoparticle constant. This allows an independent investigation of the contributions from coating thickness on the effective magnetic relaxivities of MIONs. A set of mMIONs were prepared (courtesy of Leslie LaConte and Nitin Nitin, Georgia Tech) with phospholipid-PEG conjugates of increasing molecular weights (PEG 550, PEG 750, PEG 1000, PEG 2000, and PEG 5000) which yield a corresponding increase in coating layer thickness as demonstrated by dynamic light scattering (DLS) and electron microscopy (EM).

To gain a more complete understanding of these effects on relaxation, a computer simulation was developed to predict how coating characteristics affect relaxivity. Simulations were carried out with two models. One assumes that the coating is impermeable to water and the other assumes that water has a slower diffusion constant when in contact with the outer layer of the phospholipid-PEG coating as compared to bulk water. When taken together, the experimental and simulated results contribute to an understanding of the relationship between coating thickness and changes in relaxivity and can provide important guidelines for the optimal design of magnetic nanoparticle probes for molecular imaging using MRI.

Methods

Coating of Magnetic Nanoparticles

Monocrystalline iron oxide (Fe_3O_4) nanoparticles (MIONs) were dispersed in toluene and insoluble in water prior to modification. PEG-encapsulated particles were prepared as before with the caveat that each preparation was made with one of five different phospholipid-PEG conjugates (Avanti Polar Lipids, Huntsville, AL). They each had the formula, 1,2-distearoyl-sn-glycero-3-phosphoethanolamine-N-methoxy(polyethylene glycol) X (DSPE-mPEG X), where X represents the molecular weight of the PEG portion of the lipid-PEG conjugate. PEG molecular weights (X) used in these experiments were 550, 750, 1000, 2000, and 5000. DSPE-mPEG X (in chloroform) was mixed with MIONs (50 µl of 3.3 mg/mL stock solution) and further

diluted with 3 mL of chloroform. This mixture was subsequently placed in a rotary evaporator with water bath temperature set to 60°C and left under vacuum (10 mTorr) for 30 minutes to remove all traces of organic solvents. The dried film was resuspended in 500 µl deionized water with agitation and sonication. The solution obtained was filtered using 0.1 µm Anotop inorganic membrane syringe filters (Whatman International Ltd., England). Concentrations of these stock MION solutions were determined as previously described [41].

Size Determination

Dynamic light scattering (DLS) using a Particle Sizing Systems-NICOMP 380ZLS, which allows specific measurement of the hydrodynamic radius of macromolecules in the size range of 1 nm-1 µm was used to determine the size of the micelle-coated MIONs (mMIONs). 500 µL of mMIONs were filtered using Anotop 0.1 µm inorganic membrane syringe filters (Whatman International), transferred into a 1 mL disposable glass tube, and spun at 10,000 g for 1 minute prior to DLS measurements. DLS scattering data was collected at room temperature for 1 hour. The number-weighted NICOMP analysis was used to obtain approximate hydrodynamic radii and population distributions for each sample.

To further determine the size of the mMIONs, transmission electron microscopy (TEM) was performed. Approximately 5 µL of mMION solution was placed on a carbon grid. 5 µL of 1% phosphotungstic acid was added and allowed to sit for 30 seconds for

negative staining. Liquid was then removed from the carbon grid, and the grid was imaged on a Hitachi H-7500 transmission electron microscope. Scanned images were then analyzed to determine approximate diameters.

Relaxation Measurements

A 0.47 T Bruker Minispec Analyzer MQ20 was used for T1 and T2 measurements. 500 μL of each sample (diluted from stock solution in phosphate buffered saline from Sigma, St. Louis, MO, pH 7.4 (PBS)) were placed in a 10 mm sample tube and allowed to equilibrate to 20°C in a circulating water bath. All the measurements were made at 20°C using a temperature-controlled probe cavity with an external water bath. Each measurement was repeated three times to measure variations within the readings. T2 curves were obtained using the Carr–Purcell–Meiboom–Gill (CPMG) pulse sequence and T1 values were obtained using an inversion recovery pulse sequence. T2 curves were fit to a monoexponential decay equation using CFTOOL in Matlab 7.0. Relaxivities ($mM^{-1} \cdot s^{-1}$) were calculated by taking the inverse of T1 and T2 times (s) and normalizing these values by the iron concentration (mM) for each sample as determined by the o-phenanthroline reaction [41]. Each relaxation measurement for a given coating thickness was repeated with three independent preparations of mMIONs.

pH Variation Measurements

pH was varied by using a sodium phosphate buffer composed of monosodium phosphate, monohydrate (Sigma) and disodium phosphate heptahydrate (Aldrich) necessary to achieve a 10 mM buffer at pH 5.0, pH 7.0, and pH 9.0.

Computer Simulations

Monte Carlo simulations of proton random walks have been used previously to estimate transverse relaxation induced by diffusion through inhomogeneous magnetic fields [47-50]. For this simulation, protons take random walks through a three-dimensional space containing fields representing iron oxide nanoparticles. In the simulation, protons accumulate phase changes as they diffuse through the fields created by these magnetic dipole moments. The normalized signal is computed from N different proton random walks as:

$$S(t) = \frac{1}{N}\sum_{n=1}^{N} e^{i\varphi_n(t)} \qquad (2.4)$$

Here $\varphi_n(t)$ is the phase of the n^{th} proton at time, t. The simulation proceeds as follows. Particles are randomly distributed in space. A sufficiently large space is chosen to eliminate edge effects. Protons take random walks through the particle fields. At each time step, the sum of B_z due to the particle dipolar fields is computed and the proton accumulates phase according to $\varphi=\gamma \cdot B_Z \cdot \Delta t$ (with γ the gyromagnetic ratio and Δt, the

time step). Simulations are performed with *N* protons, typically between five hundred and five thousand. Magnetic parameters used are chosen individually to be representative of the experimentally characterized particles. For instance, for MION 46-L particles [28], parameters are 2064 Fe atoms per particle, 65 emu/g Fe, average diameter 4.6 nm.

Phase changes are accumulated in regular intervals and R2 and R2* are calculated as follows. First, to calculate T2*, a decay curve is constructed. For each proton, the sum of phase up to each time point is calculated for that time point. Using equation 2.4, the signal for the time point can then be calculated. In order to calculate T2, a spin-echo is formed. For a given time-point, the phase change accumulated during the second half of the echo time is subtracted from the phase accumulated during the first half of the echo time. This simulates the effect of the 180° pulse in the spin-echo sequence. The decay curves used for T2* do not involve this subtraction and are analogous to the free induction decay. Figure 2.5 shows a typical decay curve. The decay constant, T2 or T2* respectively, is calculated by standard regression and used to obtain R2 and R2*.

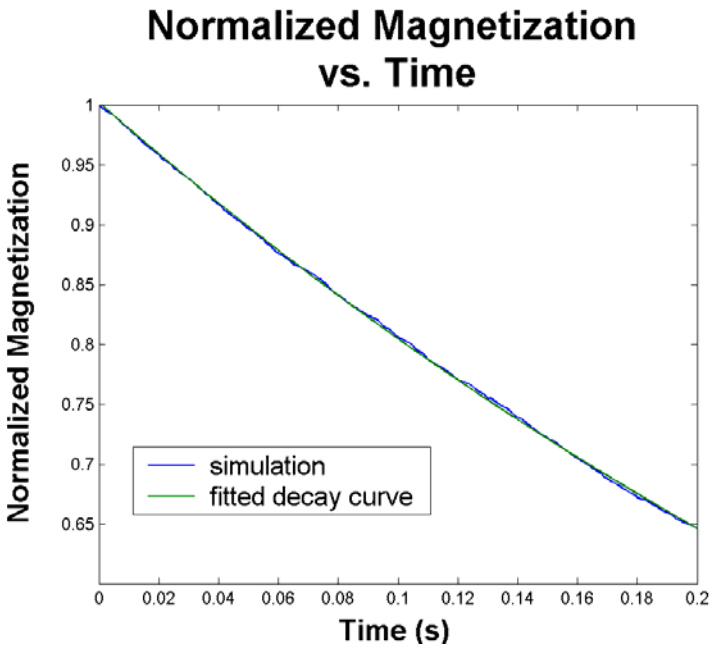

Figure 2.5: Standard decay curve showing both simulated data and fitted decay equation, exp(-t/T2) or exp(-t/T2*) . The relaxivities, R2 and R2* were found to be the same for given simulation parameters. This is expected for the motion-averaging regime for superparamagnetic particles of small radius.

Unlike previous simulations in which large time-steps on the order of 200 μs were used [47], here, a short time step of 1 ns was chosen to ensure its length was not artificially influencing simulation results. The time step was progressively shortened (down to 0.5 ns) until no effect was observed. Results were equivalent at 0.5 ns and 1 ns and thus the time step was set to 1 ns to reduce computation time. Simulations were performed using 500 protons, and magnetic parameters used were representative of nanoparticles with a 6.6 nm core diameter (6070 Fe atoms per particle). Phase changes were accumulated in 50 μs intervals. An additional parameter, exclusion radius, was

introduced as a spherically-shaped, excluded space into which protons were not allowed to diffuse, thus effectively controlling the minimal distance of approach for protons in solution. Simulations were performed varying exclusion radius from 4.5 to 50 nm to mimic variation in the thickness of the micelle coating.

In order to simulate slow/restricted diffusion, the model was further refined to include a coating layer in which the water diffusion coefficient was slower (2.5×10^{-10} m^2/s) than bulk water (2.5×10^{-9} m^2/s). The thickness of this layer was then varied from 1 to 16 nm, while the exclusion radius was held constant at 3.3 nm.

Results and Discussion

Size Determination by DLS and EM

The sizes determined by DLS and TEM are listed in Table 2.1. The results show the expected general trend of an increase in the particle diameter with an increase in PEG chain length.

Table 2.1: Variation of diameter of coated mMIONs. Changes in coating size were determined by DLS, EM, and from Ref. [51]. (Reprinted with permission from ref [52].)

Coating Type	Hydrodynamic Diameter (nm) (DLS)	Diameter (nm) (TEM)	Hydrodynamic Diameter (nm) (Ref. [51])
DSPE-PEG-550	12.5±1.3	10.96 ± 1.9	Not determined
DSPE-PEG-750	10.35±2.6	13.63 ± 1.3	10.2
DSPE-PEG-1000	12.0±0.8	13.23 ± 1.1	Not determined
DSPE-PEG-2000	16.4±3.1	14.6 ± 0.34	13.4
DSPE-PEG-5000	21.6±3.6	16.2 ± 1.3	21.4

DLS results show no significant difference in the hydrodynamic diameter of DSPE-PEG 550 and 750, possibly due to the low resolution of the DLS technique at this size range. The EM data show no significant difference between the diameters of DSPE-PEG 750 and DSPE-PEG 1000, likely due to difficulties in estimating diameters from the negatively stained images and only a small difference in polymer length when the particles are dried on carbon grids. It is expected that the particle hydrodynamic diameter would be larger than the dry particle diameter determined by EM, due to counterions or water itself forming a diffuse layer that moves with the mMION [53]. This is indeed the case with the larger diameter samples (DSPE-PEG 2000 and DSPE-PEG 5000) due to the fact that the negative staining technique and imaging conditions in EM do not preserve the extended structure seen in a hydrated sample in solution. These diameter data are in

general agreement with the hydrodynamic diameters of DSPE-PEG micelles previously reported [51].

Effect of Coating Thickness on r1 and r2 Relaxivities of mMIONs

The results for r2 relaxivity as a function of DSPE-PEG size (PEG 550, 750, 1000, 2000 and 5000) are shown in Figure 2.6.

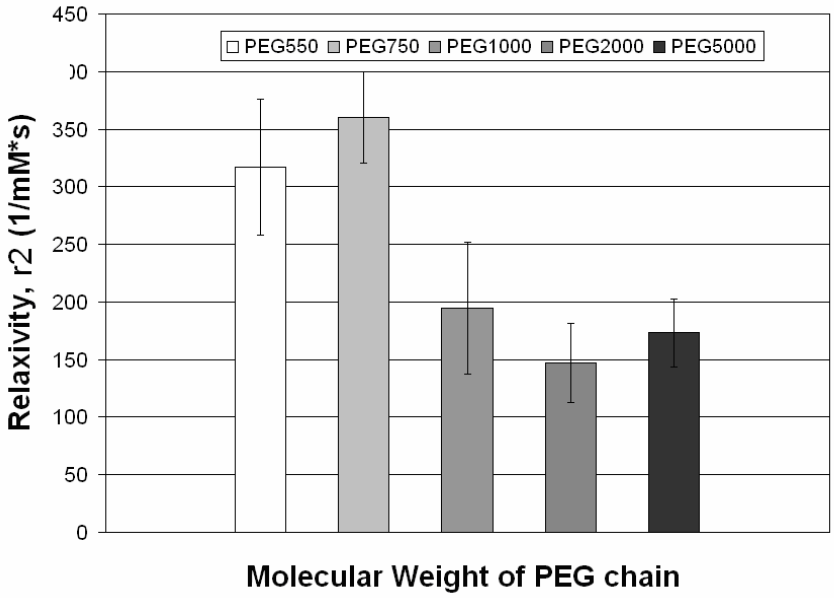

Figure 2.6: Effect of coating thickness on r2. Measurement of r2 for mMIONs with coatings with different DSPE-PEG size (PEG 550, 750, 1000, 2000 and 5000) indicates that r2 decreases as the molecular weight of the PEG portion of the phospholipid-PEG coating increases. (Reprinted with permission from ref [52].)

These results indicate that the r2 value decreases as the size of the DSPE-PEG polymer, and thus the mMION diameter (see Table 2.1), increases. As seen in the plot, there is a significant (almost 2-fold) increase in the r2 with the decrease in coating size from DSPE-PEG 5000 to DSPE-PEG 550. However, for the polymer sizes ranging from PEG 1000 to PEG 5000, there was no significant change in the relaxivity value (194 ± 57 $mM^{-1}s^{-1}$, 147 ± 34 $mM^{-1}s^{-1}$, and 173 ± 30 $mM^{-1}s^{-1}$, for PEG 1000, PEG 2000, and PEG 5000, respectively). These results clearly indicate the significant role that coating size plays in determining the net magnetic relaxivity of mMIONs. The highest r2 values are observed for the mMIONs coated with DSPE-PEG 550 and 750 (317 ± 58.8 $mM^{-1}s^{-1}$ and 360 ± 40 $mM^{-1}s^{-1}$, respectively), which have the smallest diameters. This indicates that by reducing the coating size, the negative contrast produced by mMIONs can be significantly increased. This is important for medical applications, as higher contrast typically leads to a higher sensitivity and a reduced amount of contrast agent required for imaging.

Another important consideration for the effect of coating thickness on relaxivity is the recent trend in molecular imaging, which relies on the conjugation of targeting molecules to the surface of contrast agents such as mMIONs [20]. In molecular imaging, it is important to maximize the contrast generated by each nanoparticle probe, since target concentrations are often quite low (for example, on the order of 10,000 binding sites per cell for the atherosclerosis target VCAM-1 [54] and 10,000 folate receptors in brain glioma cells [55]) and *in vivo* binding affinities can vary greatly. Successful *in vivo* imaging with MRI often requires target concentrations on the order of 10 μM [2]. The

engineering of nanoparticles with high relaxivity is thus highly advantageous for specific targeting of low-abundance receptors or antigens. Furthermore, the conjugation of large biomolecules such as antibodies (average diameter ~10 nm) to the surface of nanoparticles for specific targeting may have a large effect on the r2 characteristics due to the increase of overall apparent thickness of the coating. Depending on the effect of these biomolecules on surrounding water and its diffusion around the particle, such attachments may result in a decrease in the r2 of the contrast agent, thus making a thinner coating highly desirable.

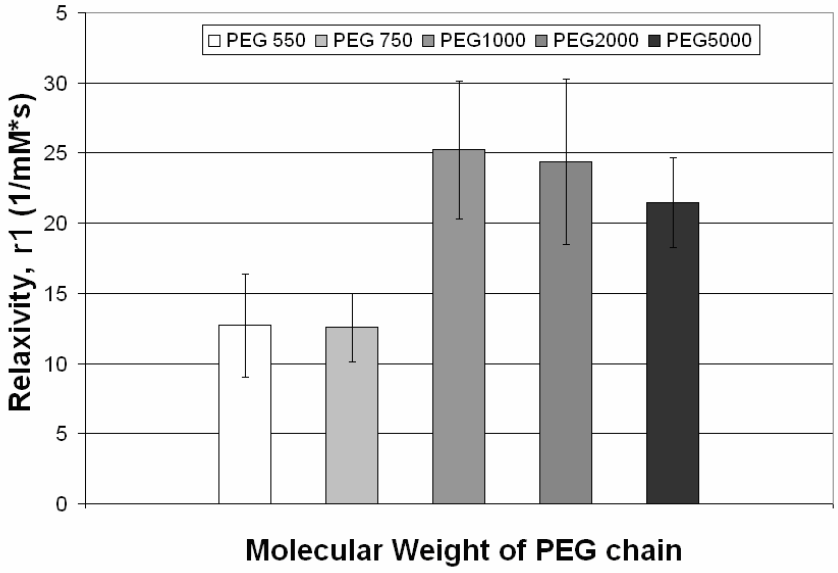

Figure 2.7: Effect of coating thickness on r1. Measurement of r1 for mMIONs with coatings with different DSPE-PEG size (PEG 550, 750, 1000, 2000 and 5000) indicates that r1 increases as the molecular weight of the PEG portion of the phospholipid-PEG coating increases. (Reprinted with permission from ref [52].)

The changes in r1 as a function of PEG size are shown in Figure 2.7. It was found that the r1 values increased as the molecular weight of PEG (and thus the coating thickness) increased. As indicated by the results in Figure 2.7, the nanoparticles with different coatings have two distinct ranges of r1 values: low relaxivity with DSPE-PEG 550 and 750 (12.7 ± 3.7 $mM^{-1}s^{-1}$ and 12.6 ± 2.4 $mM^{-1}s^{-1}$) and higher relaxivity with thicker coatings (25.2 ± 4.9 $mM^{-1}s^{-1}$, 24.4 ± 5.88 $mM^{-1}s^{-1}$, and 21.5 ± 3.22 $mM^{-1}s^{-1}$ for PEG 1000, PEG 2000, and PEG 5000 respectively). These results demonstrate that the size variation of the DSPE-PEG coatings also has a significant effect on r1 of the mMIONs, although the effect has different characteristics; as coating thickness increases, so does the r1.

MIONs have been predominantly used as negative contrast agents (R2 relaxivity) in clinical applications [45], but there has been some interest in engineering contrast agents with decreased R2/R1 ratios for use as blood pool agents [56, 57]. Although chelated Gd^{3+} and Gd^{3+}-linked albumin have been the dominant blood pool contrast agents, they need to be used at high concentrations, have relatively short circulation times, and can have toxic side effects. Therefore, the use of MIONs (or other superparamagnetic iron oxide nanoparticles) as blood pool agents has been explored as an alternative. This study indicates that it is possible to tailor the coating size to affect the R2/R1 ratio. Specifically, the results shown in Figures 2.6 and 2.7 suggest that when coating thickness increases, the ratio of R2/R1 decreases. Thus, the use of a thicker coating on MIONs may be desirable to achieve a smaller R2/R1 ratio, making these

nanoparticles more suitable for blood pool applications. By modifying the coating chemistry in addition to the thickness, it may be possible to further optimize the R2/R1 ratio of MIONs as blood pool agents in MR imaging.

Effect of pH on r1 and r2 of DSPE-PEG 2000 mMIONs

The water relaxation processes induced by the presence of contrast agents are mediated by both the diffusion of protons through the magnetic field generated by each particle and the chemical exchange of protons with bulk water. It is likely that the processes involved in mMION-induced magnetic relaxation not only depend on the magnetic core but also on the coating layer, since the effect of the nanoparticle's magnetic moment is stronger within the coating layer, because of its close proximity to the iron oxide core, than in the surrounding bulk water. In addition to coating thickness, the specific chemistry of the coating, the packing of the coating material and the overall structure of the coated particle may all play a significant role in the total contrast achieved with a specific nanoparticle-based agent.

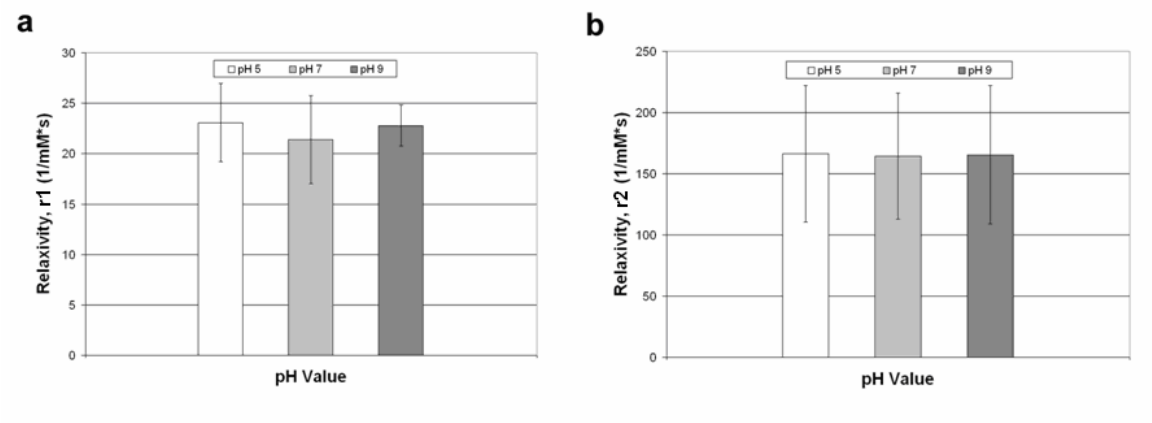

Figure 2.8: Effect of pH on relaxivity. Using buffer with different pHs (pH 5.0, pH 7.0, and pH 9.0) for mMIONs had no significant effect on either (a) r1 or (b) r2. (Reprinted with permission from ref [52].)

Depending on the thickness and their chemical characteristics, coating materials may influence both the diffusion of protons and the chemical exchange processes. Previous studies have shown that for the case of hydrated iron oxides such as ferrihydrite crystals found in ferritin (iron-storing protein) and akaganeite in dextran-coated agents such as Fercayl, structural protons at the surface of the iron oxide play a central role in water relaxation because they are readily exchangeable [58]. However, magnetite does not have such structural protons bound at the iron oxide surface, and therefore this type of proton exchange has been shown previously not to dominate the observed water relaxation [59]. In an effort to rule out substantial contributions of chemical exchange to the relaxation process observed with mMIONs, the relaxivities of mMIONs at different pH values were measured. Specifically, r1 and r2 were determined at three different pH values (pH 5.0, pH 7.0, and pH 9.0, all other conditions held constant) for a single coating (DSPE-PEG2000) and the results are shown in Figure 2.8. There were no

significant differences between the relaxivities at any of the pH values, suggesting that the predominant factor determining water relaxation by mMIONs is the diffusion of protons through the magnetic field generated by each MION particle, as discussed in more detail below.

Computational Simulations of the Effect of Coating Thickness on Relaxivity

Numerical modeling of the relaxivity of mMIONs using Monte Carlo simulation was performed to gain insight into the mechanisms by which coatings can alter relaxivity of nanoparticles. In the simulation, protons take random walks through a field containing nanometer-sized magnetic inhomogeneities representing mMIONs. Specifically, the mMIONs were assumed to have three regions (Figure 2.9a): (a) the Core, i.e., the iron oxide core that generates a magnetic field, with a closely associated hydrophobic coating region; (b) the layer immediately surrounding the core, composed of a portion of the DSPE-PEG coating that effectively excludes water, and (c) an outer layer composed of the PEG portion of the coating in which proton diffusion is assumed to be slower than in bulk water. This model is based on a model proposed by Arleth et al. [60] for DSPE-PEG micelles with no cargo in their core. Based on small-angle X-ray and neutron scattering data, Arleth et al. [60] concluded that DSPE-PEG micelles have a hydrophobic core composed of the hydrocarbon chains from the phospholipids. This core is surrounded first by a dense hydrophilic shell consisting of the polar headgroups of the DSPE and a fraction of the PEG chains and then by a loosely structured, highly hydrated corona made of the outermost portion of the PEG chains.

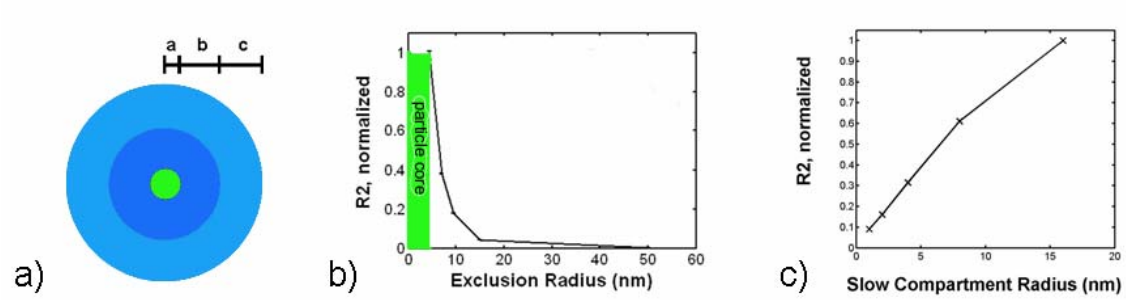

Figure 2.9: Modeling and computer simulation of mMION relaxivity. In panel **(a),** a core-shell model of an mMION is shown, in which the iron oxide core (green) is surrounded by a portion of the coating which excludes water (dark blue), and a second layer (light blue) in which there is slow diffusion. Computer simulation shows that: **(b)** R2 decreases as the water exclusion radius (core + first layer) increases, where the core size was held constant; and **(c)** as the thickness of the outer layer is increased, R2 increases due to the increased volume of slow diffusion of water surrounding the particle.

To simulate the effect of coating on water relaxivity, two approaches were employed. In the first approach, only water exclusion from the Core and the inner, exclusion layer in Figure 2.9a is considered; protons in the outer layer are assumed to behave like bulk water protons. Therefore, in the model, the water exclusion radius (Core + inner layer) determines the minimum distance of approach (measured from the center of the iron oxide core) for water protons. Numerical simulation results for this model show a sharp decrease in effective R2 as the thickness of this impermeable coating layer is increased (Figure 2.9b). As is evident in the plot of relative R2 relaxivity vs. the

radius from which water is excluded (Figure 2.9b), there is a strong dependence on size for particles with thinner coatings, which rapidly tapers off as the coating thickness increases above about 10 nm. The actual mMIONs have approximate coating thicknesses ranging from 5 nm (for PEG550, PEG750, and PEG1000) to 15 nm (for PEG2000 and PEG5000). Although the trend agrees qualitatively with the measured relaxivities, it does not explain the observed jump that occurs in relaxivity values between PEG750 and PEG1000. This discrepancy suggests a possible opposing effect which is explored in the second model below.

The second modeling approach assumes that there is a layer of coating (outer layer Figure 2.9a) that slows down water diffusion without excluding protons. In this model, protons in this layer would spend a longer period of time in close proximity to the magnetic field produced by the iron oxide core because the diffusion coefficient of water is assumed to be slower than in bulk water. Evidence exists for such an assumption from the structural study of DSPE-PEG micelles by Arleth et al. [60], in which the tightly packed hydrophilic shell of their micellar model contains a number of constrained water molecules. Measurements of water diffusion coefficients in solutions of PEG of varying molecular weights also indicate that water moves more slowly in such an environment. Data collected by Vergara et al. [61] of a range of PEG molecular weights show that as the weight fraction of a given PEG solution increases, the mutual diffusion coefficient tends to converge to approximately 2.5×10^{-10} m^2/s. Based on this data, a value of 2.5×10^{-10} m^2/s for the diffusion coefficient of water in outer, "slow" layer was chosen. This

value is an order of magnitude slower than in bulk water. The effect of an increasingly thick outer layer on R2 relaxivity was thus simulated.

Results from this simulation (Figure 2.9c) show that as the thickness of the outer layer is increased, R2, in fact, increases. This is not surprising since protons that spend more time in the vicinity of the iron oxide core will relax more quickly than those in bulk water. This model thus suggests coating regions of slow diffusion have the opposite effect of coating regions that completely exclude water. In isolation, neither individual model can explain the trend observed in the experimental data; however, a combined water exclusion and slow diffusion model may account for the experimentally observed relationship between relaxivity and coating thickness. To develop a rigorous model to accurately simulate the changes in R2 with coating thickness, future simulation work will be needed to determine if a combination of these two models, using accurate measurements of each layer's thickness and the water diffusion coefficient in the outer layer, can explain the experimentally observed relationship between coating thickness and transverse relaxivity.

Conclusions

The experimental and simulation studies show that coating properties can have a significant impact on contrast agent relaxivity. While the surface coating's thickness can influence its effectiveness as a contrast agent, it is also important to study the effects of surface chemistry on signal enhancement and clearance in contrast agents used *in vivo*.

One specific example of such a study reveals that PEG chain length has a direct impact on the blood half-life of a gadolinium-based contrast agent [62]. This study shows that *in vivo* contrast enhancement induced by gadolinium complexes varies with the length of the PEG chain to which they are attached. In the blood pool, for instance, shorter PEG polymers (550 and 1000) showed less signal enhancement than PEG2000. Thus there is a complex interplay between coating thickness, coating chemistry, and overall MR contrast generated, and all these factors should be carefully considered for the optimization of MION-based contrast agents.

From this study, it can be concluded that the coating thickness of magnetic nanoparticle probes can significantly affect their relaxivity. As coating thickness increases, there is a dramatic decrease in r2 of the mMIONs, accompanied by less dramatic influence on the r1. The results of this study thus have considerable impact on the design of magnetic nanoparticle-based contrast agents and their applications in medical diagnostics. The numerical simulations provide further insight into the effect of coating on magnetic relaxivity of MIONs, suggesting that there are competing factors (physical exclusion of protons from the magnetic field source versus longer residence time for protons within a certain sphere of coating due to slower diffusion) that determine the ultimate r2 value.

Future Directions: Application to Switchable Nanosensors

Effect of particle clustering on relaxivity

Although the magnetization of ferromagnetic colloids was first described in 1938 [63], it was not until the work of Weissleder, Josephson and others in the early 1990's that the application of iron oxide particles to MRI became widespread [28, 64]. Superparamagnetic iron oxide (SPIO) and ultra-small superparamagnetic iron oxide (USPIO) particles are valuable because of their ability to be detected by T2 and T2*-weighted imaging at micromolar concentrations.

Cellular imaging using iron oxide particles was first applied to hepatic imaging [65, 66] where particles are taken up by Kupffer cells. In the normal tissue of the liver, these specialized macrophages take up the particles, resulting in hypointensity on MR images. The presence of altered tissue types, such as primary liver cancer or secondary metastasis, is detected as areas of normal intensity as these tissues do not take up the particles. Feridex®, a commercial product of SPIO particles received FDA approval in 1996 for this purpose. Because macrophages naturally take up SPIOs, imaging of structures containing phagocytic cells such as lymph nodes [67, 68] and bone marrow [69] were natural extensions of this approach. Although this approach to cellular imaging does reveal information about the location of macrophages and can be used to

differentiate normal and pathologic tissue, it does not reveal specific molecular information.

In order to achieve greater specificity to targeted cell types, SPIOs and USPIOs have been modified with specific ligands. The goal is to modify the surface layer of the particle so it binds a specific location on cellular membrane and induces internalization. Internalization of the particles, while not specifically necessary for inducing T2 relaxation, prevents particle interference with cellular interactions as well as particle detachment. Modifications to particle surfaces can have a range of specificities. Magnetoliposomes [70] non-specifically enhance uptake of particles into non-phagocytic cells. The HIV Tat peptide provides a membrane translocation signal that increases uptake of particles [23, 46]. Ligands, such as that of transferrin (Tf), have been used to target cells expressing the transferrin receptor (Tfr) [9, 71, 72], and dendritic cells have been targeted using the CD-11 monoclonal antibody [73].

These studies, which involve imaging of cells and cellular processes, are often termed cellular imaging. Molecular imaging, however, refers to the study of specific molecular events. In some cases such as imaging of macrophages, which non-specifically take up particles, there is a distinction. Here the imaging is best described as cellular since little molecular information is revealed by non-specific, phagocytic uptake. Imaging cells via receptor-mediated uptake is both cellular and molecular imaging since the uptake reveals specific molecular information about the cell. Although these contrast agents are targeted, they do not specifically change their relaxation characteristics upon

cellular uptake. As a result, unbound, background particles cannot be easily differentiated from probes that have successfully bound. This also makes quantification difficult. There remains a desire for molecular imaging contrast agents to "switch" between states when triggered by a specific molecular event. Such a system would result in a change in contrast, or relaxation effects, upon specific molecular interactions. In this way, images can directly reveal molecular information that can be observed against a background of unbound particles.

Josephson and Weissleder [12] described a system in which DNA binding causes a nanoparticle assembly. The concept is based on the outer-sphere theory prediction that the relaxation rate (1/T2) is proportional to r^2 (r, the radius of the spherical particle). They reasoned that when individual superparamagnetic nanoparticles assemble into clusters, they effectively act as larger particles leading to an increase in relaxation rate. They started with material consisting of monodisperse, fluid-phase nanoparticles containing an icosahedral core of superparamagnetic, crystalline Fe_2O_3/Fe_3O_4 (3 nm), caged by epichlorohydrin cross-linked dextran and functionalized with amine groups (CLIO-NH_2). Particles were coupled to thiolated oligonucleotides via a N-succinimidyl 3-(2-pyridyldithio)propionate (SPDP) linker. R2 relaxation was enhanced by oligonucleotide hybridization. This change in R2 could be used as a way of "sensing" hybridization.

One potential limit of the work described in the previous approaches to switchable contrast systems is the inability to precisely correlate the "switch" or change in R2 with a

defined clustering event. The respective oligonucleotides (ODNs), P1 and P2, each had an average of three oligonucleotides per MION particle. Figure 2.10a depicts the commonly proposed scenario of a single DNA oligonucleotide linking a pair of nanoparticles. The "switching" in this case consists of the change in signal caused by single ODNs binding DNA and resulting in pairs. However, because there is an average of three ODNs per particle, it is possible and likely that larger clusters will form as depicted in Figure 2.10b. In this case, the "switching" is a change in signal that occurs when single particles cluster into various, unpredictable configurations. This sort of variable and extensive clustering has been visualized by atomic force microscopy [44].

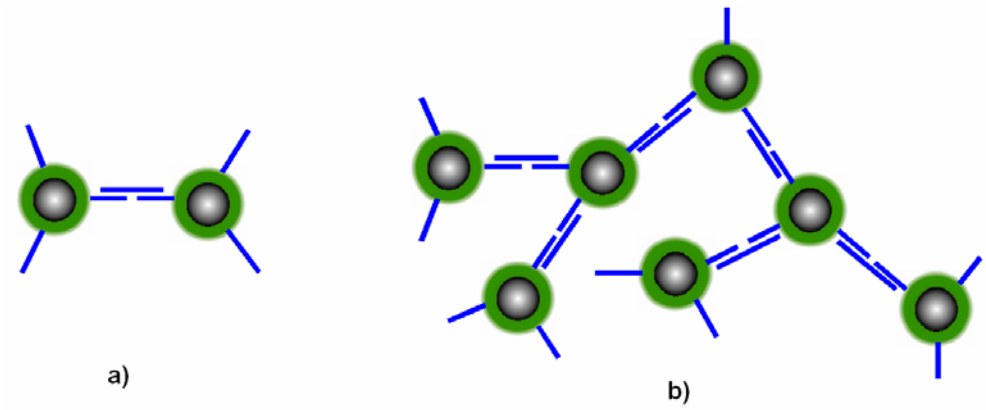

Figure 2.10: Clustering of magnetic nanoparticles. The scenario depicted in (a) represents a single DNA oligonucleotide linking two magnetic nanoparticles. This, however, represents only one of the possibilities of clustering. Since each particle has an average of three oligonucleotides attached to its surface, larger clusters are likely to form as depicted in (b). The size and frequency of these clusters is likely to vary in an unpredictable manner.

Since the number and extent of clustering is unpredictable, it will be difficult to reliably assign a particular change in signal to a specific clustering event. This limits the ability to utilize this approach for quantitative molecular imaging applications. Additionally, it cannot be expected that all particles will successfully participate in hybridization in an actual imaging experiment. This is especially true of *in vivo* experiments. Inevitably, a more realistic picture of binding will be one in which hybridization occurs only in some percentage of particles which could have potentially clustered. The change in signal due to switching must be detected against a background of unbound particles. Not only does this make detection more difficult, but again it limits the possibility of using this system in quantitative molecular imaging experiments.

In order to develop an alternative nanosensor configuration, the concept of the "molecular beacon" was employed. In optics, much work has been done to create controllable contrast agents using fluorophores and quenchers in configurations known as molecular beacons. In 1996, Tyagi and Kramer described novel hairpin-shaped nucleic acid detection probes, called "molecular beacons", which undergo a conformational transition when they bind to their target that enables them to fluoresce brightly [74]. The loop portion of a molecular beacon is a probe sequence that is complementary to a predetermined target sequence and the stem is formed by the annealing of complementary

arm sequences that are present on either side of the probe sequence. A fluorophore is covalently attached to the end of one arm and a non-fluorescent quencher is covalently attached to the end of the other arm. In the absence of target, the stem keeps the fluorophore and the quencher in close proximity to each other, preventing fluorescence. However, when molecular beacons bind to their target, they undergo a conformational change that restores the fluorescence of the previously quenched fluorophore.

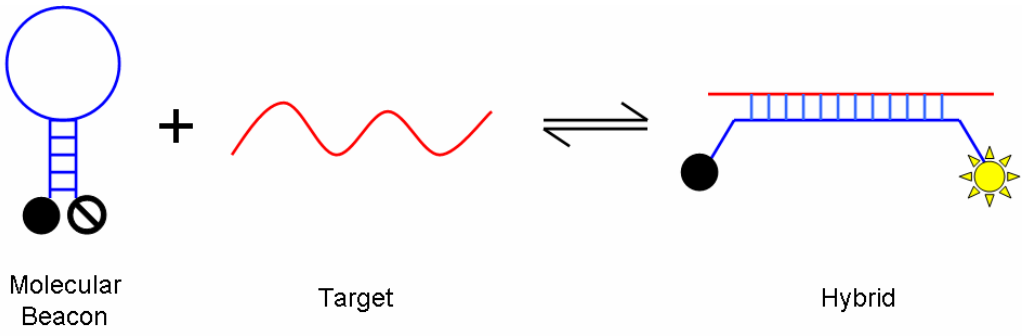

Figure 2.11: Interaction of a molecular beacon with its target. Binding to the target increases the distance between the quencher (black sphere) and the fluorophore, allowing it to fluoresce only in situations where a binding event has occurred. (Adapted by permission from Macmillan Publishers Ltd: Nature Biotech [74], copyright 1996.)

Although quenchers for magnetic nanoparticles do not exist, this concept can still be utilized in the development of switchable nanosensors for MRI. The important feature of Figure 2.11 is that there is a change in the signal due to the hybridization event. It can

be envisioned that in a molecular beacon approach for MRI, a change in relaxation due to hybridization can occur if two or more magnetic particles are either brought together or taken apart by the binding event. Although such changes in relaxation are not precisely the same on/off event seen in optics, any change in signal is a contrast that may be utilized for molecular imaging applications.

An initial test of the molecular beacon approach was developed in collaboration with Dr. Gang Bao at Georgia Tech. The goal was to create a novel MION-based probe for the detection of oligonucleotide hybridization. A PEG-phospholipid micelle-based coating was used. In this design, DNA oligonucleotides of varying length were conjugated to the functionalized MIONs at both 5' and 3' ends using chemical crosslinkers to create a stem-loop hairpin (Figure 2.12a). Hybridization to complementary oligonucleotides induced a conformational change from a closed structure (MIONs predicted to be in close proximity) to the open, double-stranded structure, resulting in a decrease in relaxivity ($r2 = (1/T2)/[Fe]$; $mM^{-1} \bullet s^{-1}$) as measured by a 0.47 T Bruker Minispec Analyzer MQ20. Decreases in relaxivity upon increase of distance between bound particles were observed experimentally (Figure 2.12b). By varying the length of the hairpin DNA in future work, the contribution of changes in distance between the MIONs and oligonucleotide can be elucidated.

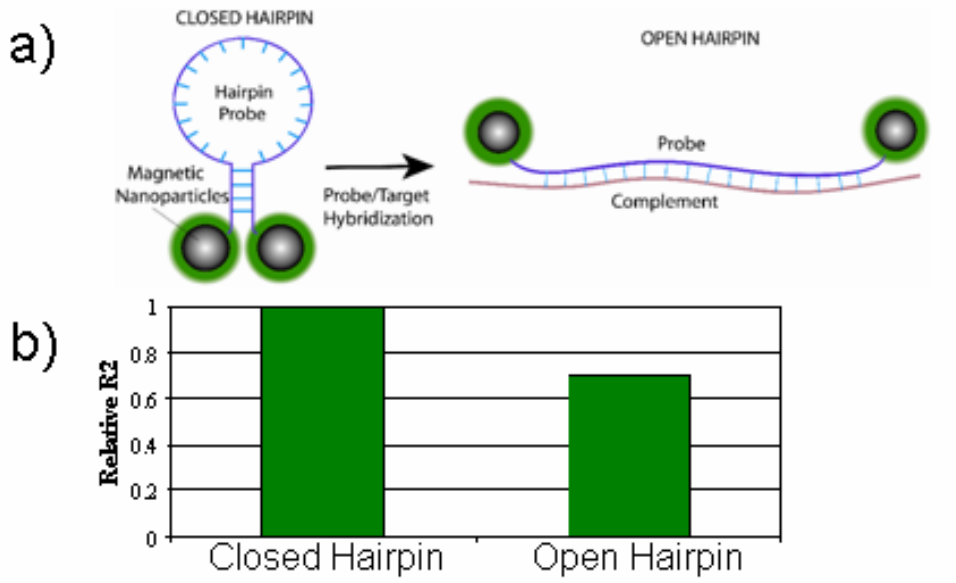

Figure 2.12: Experimental system demonstrating clustering effect on relaxivity. a) Upon hybridization to a complementary target, a 40-nucleotide hairpin (sequence = 5'-thiol AAA AAG CAG CCA GCC AGT CTA GTC TAG TTT GCT GCA AAA A thiol-3') changes from the closed conformation (left) to an open conformation (right), increasing the distance between the two magnetic particles and decreasing their r2 ($mM^{-1}s^{-1}$). b) A decrease in r2 was observed by the structural opening of the hairpin as expected.

Simulations applied to switchable systems

While clustering systems have been experimentally demonstrated to alter relaxivity, their effects have not been systematically examined theoretically. Here, computer simulations have been used to study the clustering effect. Monte Carlo simulations were performed as described above. In this case, however, particles were allowed to come together in various configurations (Figure 2.13). Issues explored included the effect of number of particles involved in clustering and binding distance

between particles. Additionally, it can be anticipated that systems will be imperfect, resulting in a limited number of particles coming together. Limited clustering must be detectable against a background of unclustered particles. Therefore, binding efficiency was incorporated as an additional parameter.

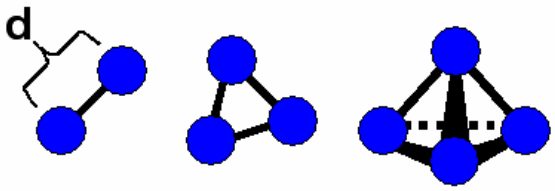

Figure 2.13: Clustering configurations. Two, three, and four particle configurations with d, distance between particle centers. Simulation parameters include d, binding efficiency, core size, coating size, coating properties, motion of particles, and diffusion of protons.

Here, an additional parameter, binding efficiency, (b.e.) was defined to represent the percentage of successful clustering. For instance, for 1000 particles, in the case of two particle clustering, a b.e. of 1.0 corresponds to 500 pairs. A b.e. of 0.5 corresponds to 250 pairs and 500 free particles. For the four particle case, a b.e. of 1.0 corresponds to 250 clusters whereas a b.e. of 0.5 corresponds to 125 clusters and 500 free particles. Simulations were performed varying binding efficiency, binding distance and number of particles involved in clustering.

In all cases, values for R2 and R2* are the same. This is expected for the motion averaging regime for superparamagnetic particles of small radius. Figure 2.14a shows an approximately linear effect of binding efficiency on R2. A binding efficiency as low as 25% can be distinguished from the case of no binding. Figure 2.14b shows the increase in R2 with particle number involved in clustering. Figure 2.14c shows the effect of binding distance on R2. The results show the decrease in R2 with increasing binding distance.

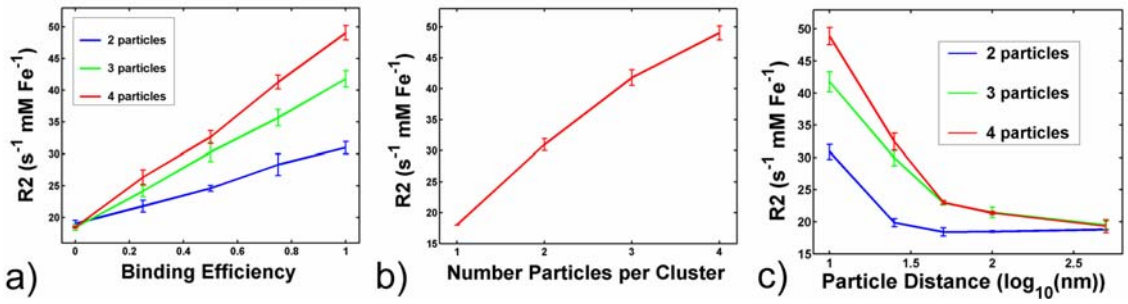

Figure 2.14: Simulated clustering effects. a) Effect of Binding Efficiency on R2. b) Number of particles involved in clustering vs. R2. Data plotted for constant binding efficiency of 1.00. c) Effect of Particle Binding Distance on R2. Data plotted for 2 (bottom), 3 (middle), and 4 (top) particle clusters.

There results indicate that significant changes in R2 can be achieved in cases of limited clustering. Low binding efficiencies can be expected in *in vivo* applications of molecular imaging, thus requiring the identification of positive binding in a background

of unbound particles. The results also indicate that clusters involving small numbers of particles can be distinguished, as may be desired in "molecular beacon" type applications. The flexibility in binding distances allow for the assembly of complex structures of particles with various sensing and targeting molecules. These results are useful for designing switchable magnetic nanosensors and applications where a limited number of particles may be involved in clustering.

Simulations of effect of coating size on clustering

Particle size and hydrodynamic radius appear to have significant effects as discussed above and may become important considerations in probe design for clustering applications. To further address this issue, changes in particle and coating sizes were incorporated into further work to investigate their effects on R2 due to clustering, $\Delta R2$.

Core diameter (nm)	4 particle clustering ΔR2 ($mM^{-1} s^{-1}$)	8 particle clustering ΔR2 ($mM^{-1} s^{-1}$)
4.6	1.1	2.1
6.6	2.7	5.6
10.0	5.5	10.9

a)

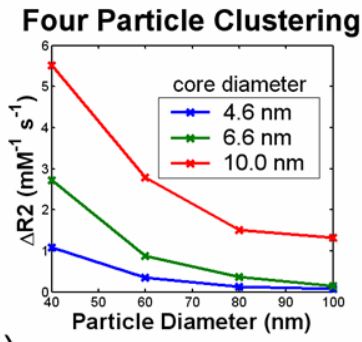

b)

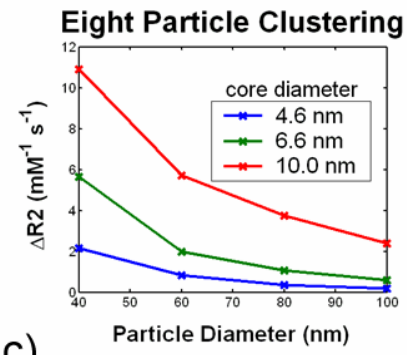

c)

Figure 2.15: Simulated effect of particle size and coating on the clustering effect. Table (a) showing increased clustering effect (ΔR2) with larger core size and graphs (b and c) showing that for constant core size, increased particle diameter (by increased coating size) results in a decrease in maximum effect due to clustering. In (a), the total particle diameter is 40 nm, but the magnetic core size is varied. In (b) and (c), each line represents a fixed magnetic core size, but the overall particle diameter is varied by increasing the coating thickness surrounding the magnetic core.

Figure 2.15a demonstrates that for a fixed particle diameter of 40 nm (core plus coating), larger core sizes and greater number of particles increase the clustering effect. In the table, all particles were 40 nm in overall diameter, meaning that particles with smaller cores had relatively larger coatings. The clustering was performed by allowing these particles to come together as close as possible (40 nm center-to-center distance). For particles with smaller cores (larger coatings), the change due to clustering (ΔR2) is reduced since the magnetic fields of the particle cores cannot overlap as much as in the case of larger cores where the larger magnetic crystal and relatively smaller coating allows for magnetic fields to overlap, creating a greater clustering effect.

Figures 2.15b and 2.15c demonstrate that while clustering effects are larger when core size is increased, these effects diminish rapidly when overall particle size increases as is the case when coating size is increased. Clusters involving larger core sizes, with minimal coating thickness are optimal for maximizing the effect of clustering. The results show that the coating thickness is an important consideration in the design of activatable probes for MRI.

Conclusions

The development of the computer simulation used for these studies provides a useful tool for many other contrast agent studies. Computer simulations allow for the controlled study and testing of individual factors in determining overall relaxation properties. By incorporating individual properties into simulation and systematically reviewing their effect, a picture of the relative contribution of factors to the overall observed T2 can be obtained. This is especially useful in planning future design of nanoparticle probes, as complicated chemical preparations can be time consuming and difficult to synthesize. By first testing hypothetical probes in simulation, potential configurations can be evaluated and the most promising candidates then selected for laboratory preparation.

The main value of such a simulation is that it allows for testing hypotheses on the effects of nanoparticle parameters relatively quickly and independently, without synthesizing each particle. Additionally, in actual synthesis, it may be difficult to change a single parameter without affecting others, thereby making the relative contribution of each factor in overall R2 change difficult to assess experimentally.

While simulation can provide a tool for understanding T2 relaxation, the validity of results cannot be verified without laboratory testing of actual nanoparticle designs. Additionally, the interplay of environmental factors in experiment can prove to be too complicated to be fully incorporated in simulations involving nanometer sized objects.

Nevertheless, future simulations can be used to refine these models to gain a more comprehensive mechanistic understanding of the processes determining the proton relaxation characteristics of MIONs. By carefully studying all the factors that influence the relaxation properties of a contrast agent, it will be possible to optimize the design of magnetic nanoparticle probes for specific applications, including the imaging of the blood pool and molecular imaging of disease states.

CHAPTER 3

OFF-RESONANCE SATURATION AS A MEANS FOR GENERATING CONTRAST WITH SUPERPARAMAGNETIC NANOPARTICLES

Background

Typically, superparamagnetic iron oxide (SPIO) contrast agents are used for their effect on T2 or T2* [20]. They have been applied to liver imaging and are increasingly being investigated as tools for *in vivo* tracking of stem cells and tumor progression [22, 23]. Additionally, biocompatible particles have been linked to specific ligands for targeted molecular imaging applications [7-11]. While most of these studies have met with some success, a significant limitation has been the inability to positively identify iron oxide contrast agents. This is largely because in T2 or T2* weighted images, magnetic nanoparticles lead to signal reduction and sometimes signal voids. In such images, it is difficult to estimate nanoparticle concentration, and quantification would require T2 or field mapping. When particles are present in high concentrations, the border of signal void can extend out, causing overestimation of particle extent.

In addition, signal voids can be caused by other factors including field inhomogeneities and susceptibility-induced artifacts from macroscopic field inhomogeneities such as those at tissue interfaces. In molecular imaging applications using iron oxide nanoparticles, these issues make identification of labeled cells inconclusive. At high magnetic fields, which are becoming widely used in clinical practice, the sensitivity to susceptibility-induced artifacts from such macroscopic field inhomogeneities is increased.

Given that the particles cause local field inhomogeneities, it is also possible, by the application of off-resonance irradiation, to exploit the effect of field inhomogeneity as an alternative contrast mechanism for these agents. There has been recent work seeking to generate positive contrast for superparamagnetic particles [75-77]. In the white-marker method [75, 76], positive contrast labeling is used to track catheter-based paramagnetic markers, such as those used during endovascular interventions. This technique relies on the dipolar field surrounding paramagnetic markers by introducing a dephasing gradient on the slice-select axis to spoil signal across the sample. In regions where the local gradients surrounding the paramagnetic marker are of the right amplitude and orientation, however, the signal becomes refocused. The resulting image shows a signal void everywhere except in the voxels containing paramagnetic marker. In off-resonance excitation [77], a spectrally selective pulse is used to excite only those protons influenced by the magnetic field of particle-loaded cells.

These methods generate images that contain signal only in areas corresponding to locations of magnetic particles. Furthermore, the white-marker method is only sensitive to macroscopic field inhomogeneity caused by paramagnetic material and both methods are only sensitive to a volume surrounding the paramagnetic material having the correct field variation or field. Due to the latter point, the amount of signal that can be generated is limited.

Here, a diffusion-mediated off-resonance saturation method for generating contrast using ultrasmall SPIO (USPIO) nanoparticles is demonstrated and examined. In this method, bulk water protons are imaged with and without the presence of an off-resonance saturation pulse. Unlike chemical exchange dependent saturation transfer (CEST) contrast agents [19], which function by reducing the water proton signal through a chemical exchange site, this method relies on diffusion of water molecules around the iron oxide nanoparticle. Compared with the white-marker method and the off-resonance excitation method, the present method is sensitive to microscopic effects of USPIO and to all water protons that are affected by the USPIO due to diffusion.

The effect of the off-resonance saturation (ORS) on the image intensity in the presence of magnetic nanoparticles is examined experimentally. It is demonstrated to be distinct from the exchange-mediated magnetization transfer (MT) effect [17] and can be seen even in the presence of MT. Additionally, the dependences of this ORS effect on off-resonance irradiation, nanoparticle concentration, pH, and diffusion rate are investigated.

Theory

In the presence of an external magnetic field, superparamagnetic particles alter the magnetic field surrounding each particle in a manner approximated by the dipole field,

$$B_z = \frac{\mu_0 \mu}{4\pi r^3}(3\cos^2\theta - 1) \quad (3.1)$$

The resulting magnetic isosurfaces define shells surrounding the particle (Figure 3.1a). Figure 3.1b shows the relative compartment size of a 100 Hz volume for different sized particles. Application of appropriate off-resonance irradiation saturates protons in some shell surrounding the particle, and diffusion leads to an apparent partial saturation of a volume near the shell determined by offset frequency, bandwidth, and diffusion in the time of the off-resonance irradiation, causing a signal reduction. From the spatial distribution of a dipole field, it is anticipated that larger off-resonance ($\Delta\omega$) occurs in small shells near the particle, leading to smaller effect, and smaller $\Delta\omega$ occurs in larger volumes, corresponding to greater effects.

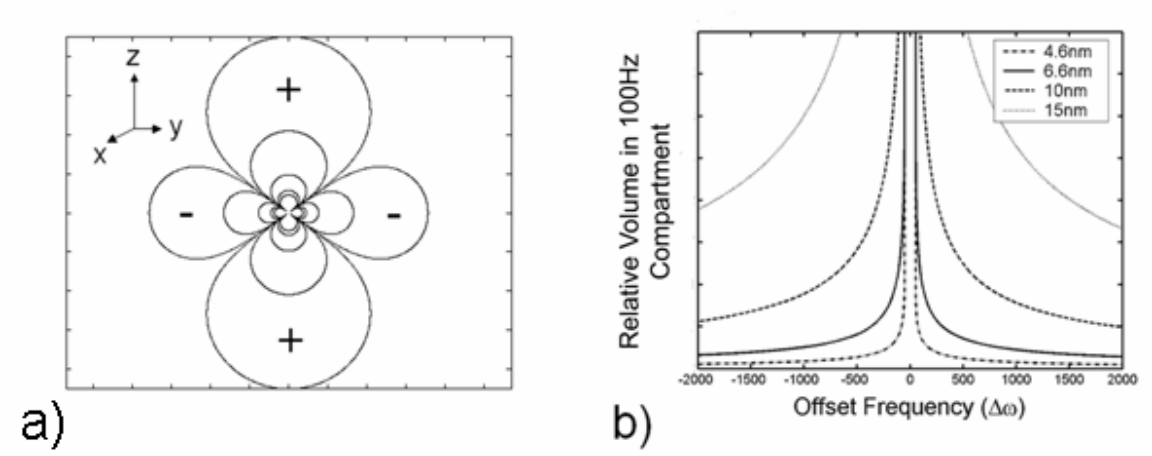

Figure 3.1: Particle dipole field lines create shells surrounding the particle. a) Plot of field isolines surrounding the particle as approximated by a dipole. + and – indicate positive and negative values for the field. The magnitudes of plotted lines (from inner to outer lines) are: 235, 117, 23, 2.3, 0.2 μT. b) Relative volumes in 100 Hz compartments for particles of varying diameter. The center frequency of the compartment is plotted on the x-axis.

Diffusion Dependence

In addition to saturation volume defined by the shell influenced by the off-resonance irradiation, the ORS effect depends on diffusion rate as this relates to the amount of time a proton spends in the shell, δt. Although these shells are small, repeated replacement of protons by diffusion and consequent saturation of these new spins within each shell should result in amplification of the ORS effect. The spatial extent of protons affected by the ORS pulse is determined by the diffusion during the duration of the pulse, if we assume that the thickness of the shell is much less than the diffusion distance. On the other hand, flip angle of water protons in the targeted shells depends on δt by the

relation, $\alpha = \gamma B_1 \delta t$. These factors result in a nonlinear dependence on δt. This has been experimentally observed and will be discussed later.

Methods

Iron oxide particles with a core size of 6.6 nm and a PEG-phospholipid coating were prepared as previously described [41]. These micelle-coated MIONs (mMIONs) had an overall hydrodynamic diameter of 12-14 nm as determined by dynamic light scattering (DLS) and electron micrography. Dilutions were made using 1× Dulbecco's phosphate buffered saline (PBS) without Ca^{2+} or Mg^{2+} (ICN, Ohio). Dilutions of Feridex (Advanced Magnetics, Inc., Cambridge, MA) were made in citrate buffer. For pH experiments, imaging was performed on five sets of particle solutions at concentrations of 0.01, 0.02, 0.05, 0.1, 0.2, 0.5, and 1.0 mM Fe, adjusted to pH values of 6.0, 7.0, 8.0, 9.5, and 10.9, respectively, using NaOH and HCl.

Agarose gel phantoms were made by first preparing a 2% agarose plate. Cylindrical plugs were removed and molten 2% agarose with various concentrations of nanoparticles was poured into the vacant areas on the plate. The resulting 2% agarose plate contained no physical boundary between areas of particles and areas devoid of particles. For diffusion experiments, Feridex particles were prepared in three concentrations (0.2, 0.5 and 1 mM Fe) in various solutions of PEG-400. Vergara et al.

[61] have previously measured mutual diffusion coefficients in these solutions showing that increasing PEG-400 weight fraction corresponds to decreasing diffusion rate. Preparations were made using weight fractions, $W_i = 0.01$, 0.15, 0.25, and 0.45, corresponding to diffusion coefficients, $D_i = 0.44$, 0.41, 0.37, and 0.29×10^{-9} m^2/s respectively. The diffusion constant of bulk water, $W_i = 0$, is taken to be 2.5×10^{-9} m^2/s.

Imaging was performed on a 3T Siemens TRIO scanner (Siemens Medical Solutions, Malvern, PA) using a FLASH sequence (for solution images: TR/TE 35/4.8 ms, flip angle 20°, matrix size 256 × 256, FOV 128 mm, slice thickness 5 mm; for agarose images: TR/TE 40/4.8 ms, flip angle 15°, matrix size 256 × 256, FOV 200 mm, slice thickness 4 mm; and for diffusion measurements: TR/TE 36/4.8 ms, flip angle 15°, matrix size 128 × 128, FOV 150 mm, slice thickness 3 mm). Off-resonance irradiation was accomplished by applying a 6 ms Gaussian pulse in each TR prior to imaging pulses. Offset frequency ($\Delta\omega$) and power of off-resonance pulse were varied. All images were obtained within SAR limits on the 3T clinical scanner.

Results and Discussion

In order to quantify the magnitude of the ORS effect, the ratio, 1-(M_{sat}/M_0), where M_{sat} represents the image taken with off-resonance irradiation and M_0 represents the image without it, was calculated. This ratio is analogous to the magnetization transfer ratio (MTR) used in magnetization transfer contrast (MTC) imaging. The ORS ratio refers to the quantification of the off-resonance effect due to diffusion around SPIO particles. Increased ORS effect is reflected in higher ratios. It is conceivable that a contrast agent could be developed to employ both MT and ORS.

Concentration and ORS

In Figure 3.2, a FLASH image obtained without off-resonance irradiation (left) and a ratio image (right) are shown. In the ratio image, it can be seen that the control buffers show little signal and the ability to identify particle samples increases with iron concentration. Concentrations as low as 0.02 mM Fe can be visually distinguished from control samples that do not contain particles.

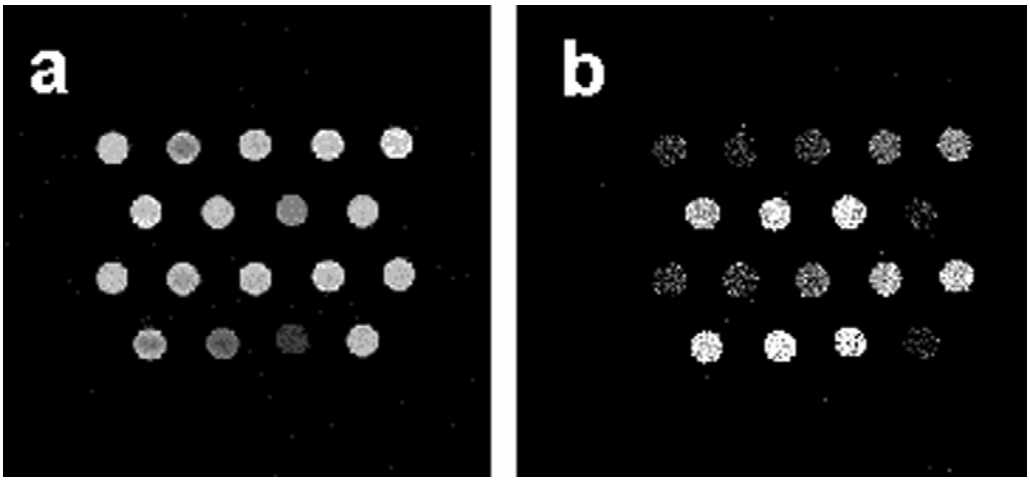

Figure 3.2: Standard and off-resonance MRI of particle solutions. a) FLASH image of Feridex (top two rows) and mMION (bottom two rows) samples in 2.0-ml tubes, b) ORS ratio image showing increasing ratio with concentration for both Feridex and mMION samples. The sample order for each set of two rows (in mM Fe) is: 0 (buffer only, citrate for Feridex and PBS for mMIONs), 0.01, 0.02, 0.05, 0.1, 0.2, 0.5, 1.0, 0. TR 35 ms, TE 4.8 ms, flip angle 20º, offset: – 650 Hz.

The off-resonance irradiation results in a decrease in signal and corresponding increase in ORS ratio that is dependent on concentration and power of off-resonance pulse (Figure 3.3). In the figure, each line corresponds to a plot for a single concentration of particles expressed as mM Fe. There is a maximum power above which further increases in ORS cannot be obtained. Subsequent data was obtained using a B_1 of 2.6 μT.

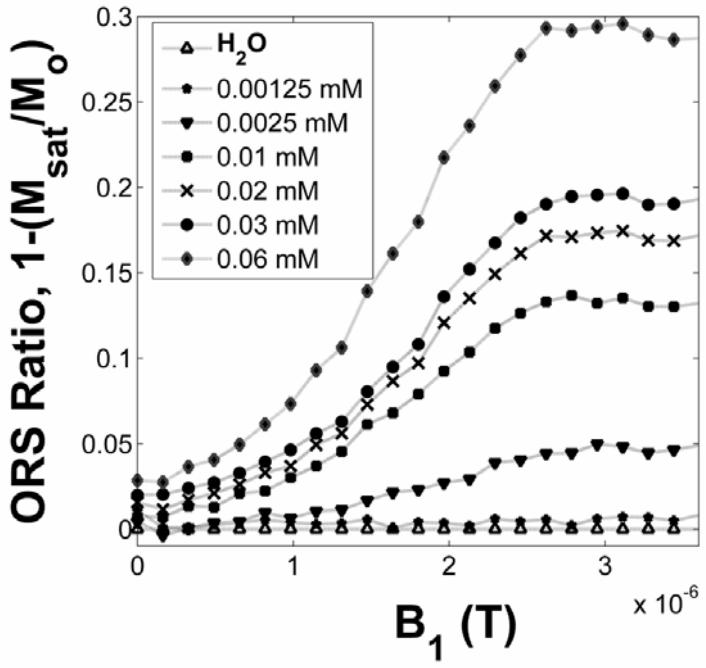

Figure 3.3: ORS ratio vs. power of off-resonance pulse. Plots are for several concentrations of iron indicated by the legend. The plots tend to flatten out at a B_1 of 2.6 μT, above which increasing power does not result in further off-resonance saturation.

As expected, increasing concentration results in an increase in ORS effect. Although this increase is linear for low concentrations, it becomes nonlinear at higher concentrations where the inter-particle distance shortens to a point that fields arising from adjacent particles overlap significantly, and ORS effects from adjacent particles do not simply add. Taking the expected magnetization as 65 emu/g Fe at 3T [28], it is estimated that at the offset frequencies used, the targeted shells are approximately 100 nm from the particle center. At 0.05 mM Fe, the interparticle distance is approximately 400 nm, making shells from adjacent particles on the order of 200 nm apart. At this distance,

taking the diffusion contribution into account, it is conceivable that contributions from neighboring particles are not independent and may be less than simple summation. Given this argument, it is not surprising that increases in concentration above 0.05 mM resulted in less than linear increases in ORS as shown in Figure 3.4.

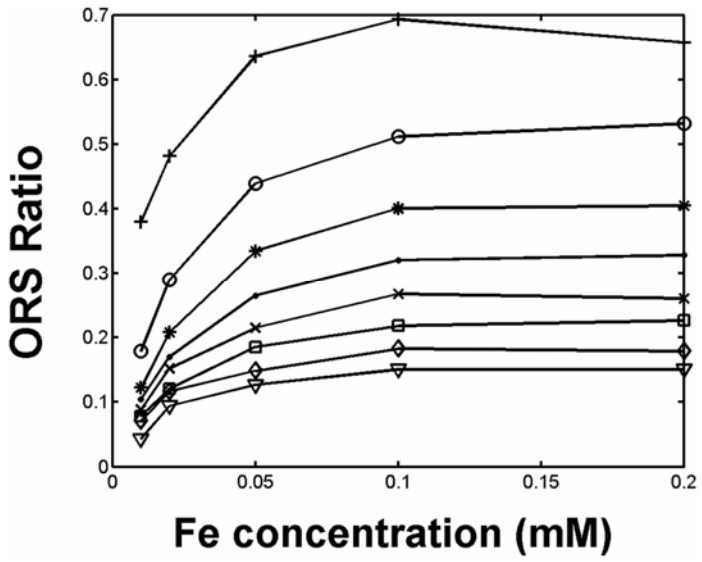

Figure 3.4: Plot of ORS Ratio vs. Iron concentration for varying offset frequencies in Hz (Δω). + 150, ○ 250, * 350, ● 450, × 550, □ 650, ◊ 750, ∇ 850.

As ORS ratio increases with concentration linearly at concentrations below saturation, the ORS approach can be used as a simple method for quantification of nanoparticles in an image. Correlating signal with concentration can reveal not only the

presence of a disease, but also its severity. For instance, Zimmer et. al. [78] showed a correlation between magnetic particle uptake and the number of thymidine kinase positive cells in a rat gliosarcoma model. Also Roberts et. al. [79] reported that concentration of contrast agent can be used to determine microvascular permeability, which correlates strongly with tumor grade. For intracellular applications, such as the detection of macrophage activity, the relationship of ORS and concentration may become more complicated as particles are clustered together and diffusion around the particles is restricted.

Figure 3.5 shows the dependence of the signal intensity on the frequency of the off-resonance pulse. The line for pure water represents signal loss due to direct saturation, and is therefore viewed as control for assessment. The difference between the pure water curve and that for samples containing particles reflects the ORS effect. The data suggests a useful offset range of 500 Hz < $|\Delta\omega|$ < 1500 Hz, below which direct saturation is too high and beyond which the off-resonance effect diminishes.

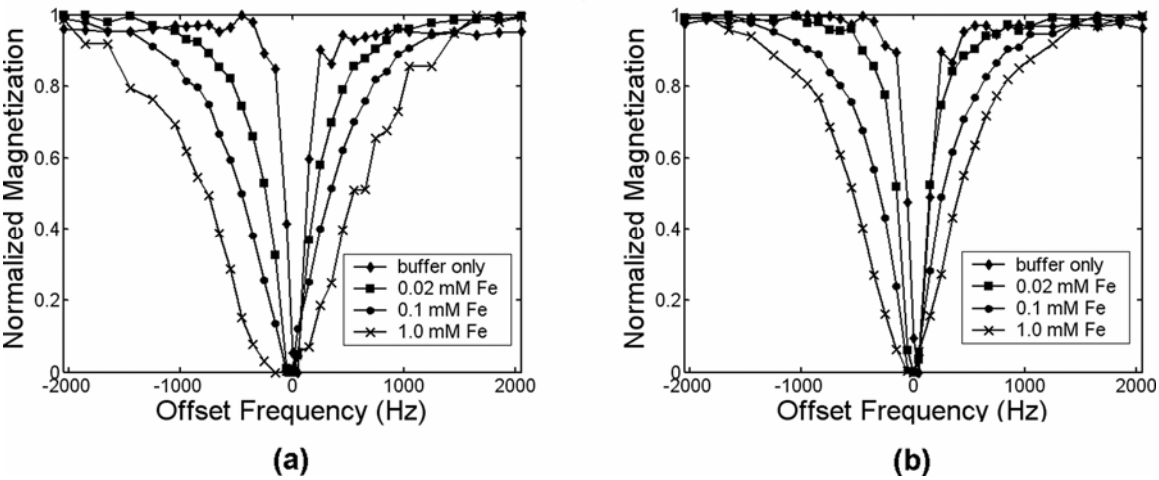

Figure 3.5: Normalized magnetization vs. offset frequency. a) mMIONs and b) Feridex.

Magnetization Transfer and ORS

At the off-resonance frequencies used, it is important to examine the ORS effect along with magnetization transfer (MT), as both are likely present in *in vivo* applications. The ORS effect is distinct from the MT effect in that it relies on the diffusion of water molecules among different compartments, the borders of which are defined by magnetic field isosurfaces and not necessarily by physical separation. In MT, a chemical or otherwise physical exchange of protons occurs [17]. In order to ascertain that the ORS effect is not due to MT, it was studied in solutions of varying pH. Gossuin et. al. [58, 80] have previously used this approach to distinguish between outer and inner sphere effects. OH groups located at the surface of hydrous particles exhibit amphoteric behavior (see Figure 3.6).

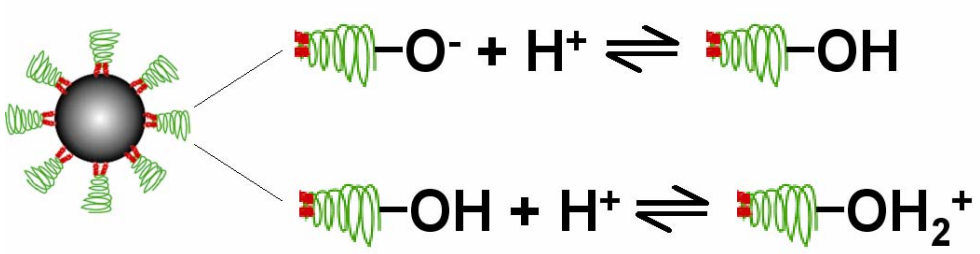

Figure 3.6: OH groups located at the surface of particles have differing numbers of exchangeable protons depending on pH. At low pH, the surface is more protonated, increasing the number of potentially exchangeable protons.

The surface is more protonated at low pH than at high pH. Relaxation is more pronounced at low pH due to the larger number of exchangeable protons. The proton exchange from these groups can be controlled by varying pH. Since changes in pH affect the rate of exchange, an MT like process will be affected by pH whereas the ORS effect, primarily dependent on diffusion, should remain constant over variations in pH for which the nanoparticles remain stable. Figure 3.7 plots the ORS ratio for Feridex obtained at different pH. The independence of the ORS ratio from pH suggests that it is a process due to diffusion rather than due to exchange as in magnetization transfer.

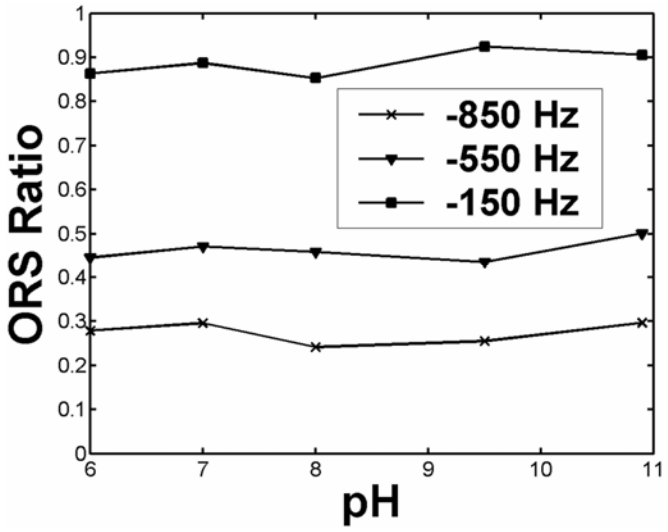

Figure 3.7: ORS Ratio vs. pH plotted for the different offset frequencies. The independence of the ORS effect from pH suggests diffusion rather than exchange as the primary mechanism.

In *in vivo* applications where MT is present, there is concern that the ORS effect may not be large enough to be observed. Magnetization transfer appears in tissues throughout the body, and agar is often used in phantoms to represent these tissues [81]. Therefore, a phantom was created made from 2% agar with embedded particles at various concentrations. In Figure 3.8, these particles can be seen in the left image as darkened areas within the phantom. On the ORS ratio image on the right, embedded particles can be identified within the agar (which also shows MT effect) indicating that this effect can be observed even in the presence of magnetization transfer. Since MT and ORS operate via different mechanisms, their effects are additive. For *in vivo* applications where it may be desired to separate these effects, it is possible to quantify MT prior to application of contrast agent where the MTR image can serve as a baseline.

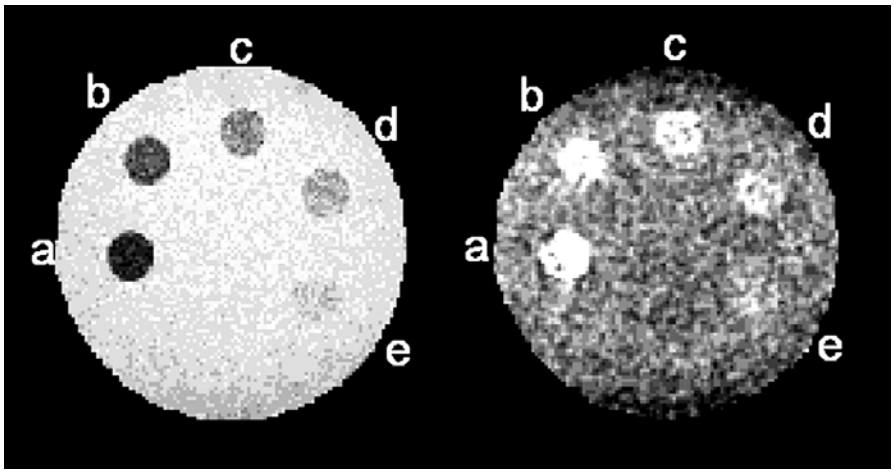

Figure 3.8: Agar phantom (2%) with embedded particles. Concentrations in mM Fe: a) 0.5 b) 0.25 c) 0.125 d) 0.063 e) 0.031. The left image is taken without off-resonance pulses, and the image on right is the ORS ratio. TR 40 ms, TE 4.8 ms, flip angle 15º, offset: – 700 Hz.

Given that the ORS approach is based on an off-resonance frequency, it will depend on the B_0 inhomogeneity. An additional concern is fat resonance, which at 3T is nearly 500 Hz. This should be considered, and it may be necessary to restrict *in vivo* applications to the positive portion of the dipole in order to avoid confusion with fat suppression.

Diffusion and ORS

Figure 3.9 shows an image of samples obtained without off-resonance irradiation (left) and an image corresponding to the ORS ratio (right), where M_{sat} was obtained with 1000 Hz offset irradiation. Each row of samples contains a single concentration of iron. Weight fraction of PEG-400 increases across the row, corresponding to decreasing diffusion rate from left to right in the images. Because of the increasing weight fraction of PEG-400, and corresponding decrease in water content, signal intensity decreases across the row in the standard image on the left side of the figure. In the ORS image, it can be seen that pure water shows little signal, and samples along each row show increasing ORS signal with decreasing diffusion rate.

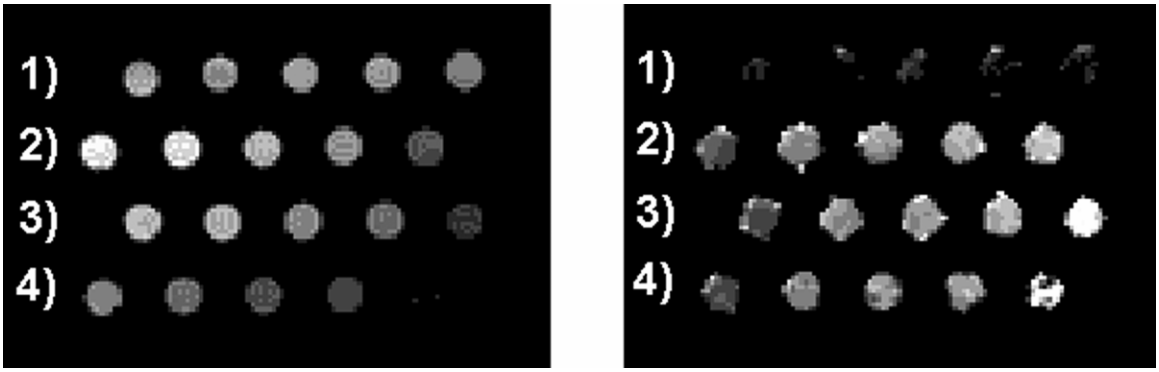

Figure 3.9: MRI showing diffusion dependence of ORS effect. FLASH image of samples obtained without off-resonance irradiation (left) and an image corresponding to the ORS ratio (right), where M_{sat} was obtained with 1000 Hz offset irradiation. Iron concentration is constant across each row: 1) no particles, 2) 0.2 mM Fe, 3) 0.5 mM Fe, 4) 1.0 mM Fe. Weight fraction of PEG-400 increases across the row: W_i=0, 0.01, 0.15, 0.25, and 0.45, corresponding to diffusion coefficients, D_i=2.5, 0.44, 0.41, 0.37, and 0.29 $\times 10^{-9}$ m^2/s respectively. TR 36 ms, TE 4.8 ms, flip angle 15º.

For a constant offset frequency of 600 Hz, the ORS ratio versus PEG-400 weight fraction is shown in Figure 3.10a and that versus diffusion constant determined according to reference [61] is illustrated in Figure 3.10b. Data show that the dependence on water diffusion becomes most significant at rates of 0.5×10^{-9} m^2/s and slower, although this dependence is expected to vary with the ORS pulse length and the off-set frequency. Lutsep et. al. [82] reported that the diffusion coefficient in ischemic lesions increased with time after symptom onset, from $0.29 – 0.33 \times 10^{-9}$ m^2/s for ischemic lesions at less than 8 hours, to $0.61 \pm 0.14 \times 10^{-9}$ m^2/s at 8-24 hours and $0.51 \pm 0.18 \times 10^{-9}$ m^2/s at 1-8 days, and eventually to a value of $2.63 \pm 0.37 \times 10^{-9}$ m^2/s at 5 months after symptom onset. Therefore, ORS may be useful in the follow-up of stroke recovery. Additionally, Desprechins et. al. [83] showed that brain abscesses result in diffusion coefficients in the range of $0.21 – 0.34 \times 10^{-9}$ m^2/s and that this can be used to distinguish them from intracerebral necrotic tumors which are frequently impossible to differentiate with conventional MR imaging, suggesting an application of the present technique in intracerebral tumor.

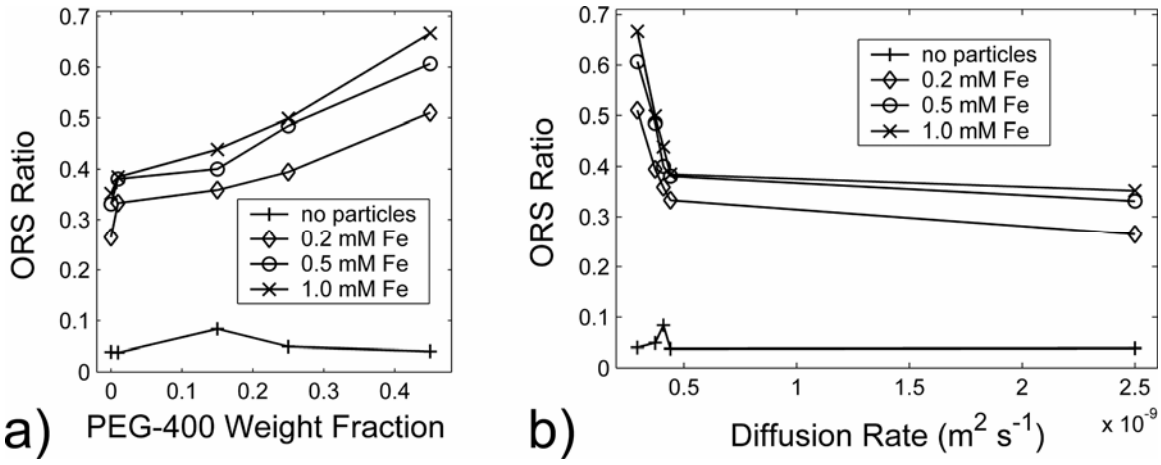

Figure 3.10: Plots of ORS ratio. a) ORS ratio vs. PEG-400 weight fraction and b) ORS ratio vs. diffusion constant for a constant offset frequency of 600 Hz. For PEG-400, increasing weight fraction results in decreasing diffusion constant.

As mentioned above, the ORS ratio should be related to δt, the amount of time needed for a proton to traverse a particular shell, in a non-linear manner. Here, δt should depend on shell size and diffusion rate. In order to test this, this ORS effect was studied at different offset frequencies ($\Delta\omega$). Decreasing $\Delta\omega$ corresponds to shells further from the particles and larger in size. The dependence on diffusion should vary with offset frequency. As can be seen in Figure 3.11, as $\Delta\omega$ decreases and hence the shell size increases, the ORS effect not only increases but also exhibits less dependence on diffusion rate as the diffusion mediated spread of the saturation effect relative to the shell size diminishes.

Taking the above together, it is likely that the dependence on the diffusion arises from opposing consequences of the diffusion rate. Slower diffusion rates result in longer residence times within targeted shells, allowing for greater energy absorption. At the same time, slower diffusion decreases the rate at which fresh spins are entering shells, and hence the spatial extent of the effect. These data suggest that the dependence on diffusion is dominated by the residence time.

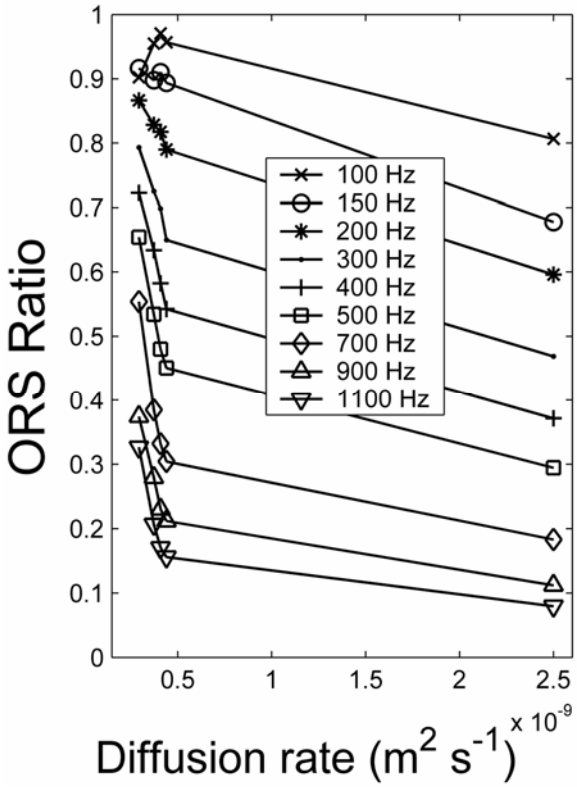

Figure 3.11: ORS vs. Diffusion Rate, obtained at various off-resonance frequencies. $\Delta\omega$ noted in the legend. These plots indicate the dependence on diffusion varies with offset frequency as well as diffusion rate.

A Model for ORS

In order to further understand the ORS effect, a simple model can be assembled based on the dependencies examined above. The effect increases with increasing iron concentration. It increases with shell size, but it is also highly dependent on diffusion. As discussed earlier, the dependence on diffusion can be related to δt, where δt represents the time a proton spends in a particular shell. While this should not be considered a complete representation of ORS, an approximate relation can be given as:

$$ORS = kTV_{shell}\frac{1-\cos(\gamma B_1 \delta t)}{\delta t} \qquad (3.2)$$

where k is a proportionality constant and V_{shell} is the volume fraction of targeted water shells which depends on the particle's magnetization characteristics, its concentration, and the frequency of offset-resonance irradiation. T represents duration of the off-resonance irradiation, on the order of milliseconds, while δt is on the order of tens of nanoseconds to microseconds, depending on the shell size. $TV_{shell}/\delta t$ therefore accounts for the diffusion-mediated saturation volume, which has a greater extent than the volume defined by the off-resonance frequency alone. A simple estimate of δt can be made using the volume of the shell and the diffusion relation $\Delta z_{rms} = \sqrt{2D\delta t}$ where Δz_{rms} is taken as the average thickness of a given shell. Equation 3.2 leads to curves in Figure 3.12, which show increased ORS for lower diffusion constants as well as lower offset frequencies, in agreement with the experimental data.

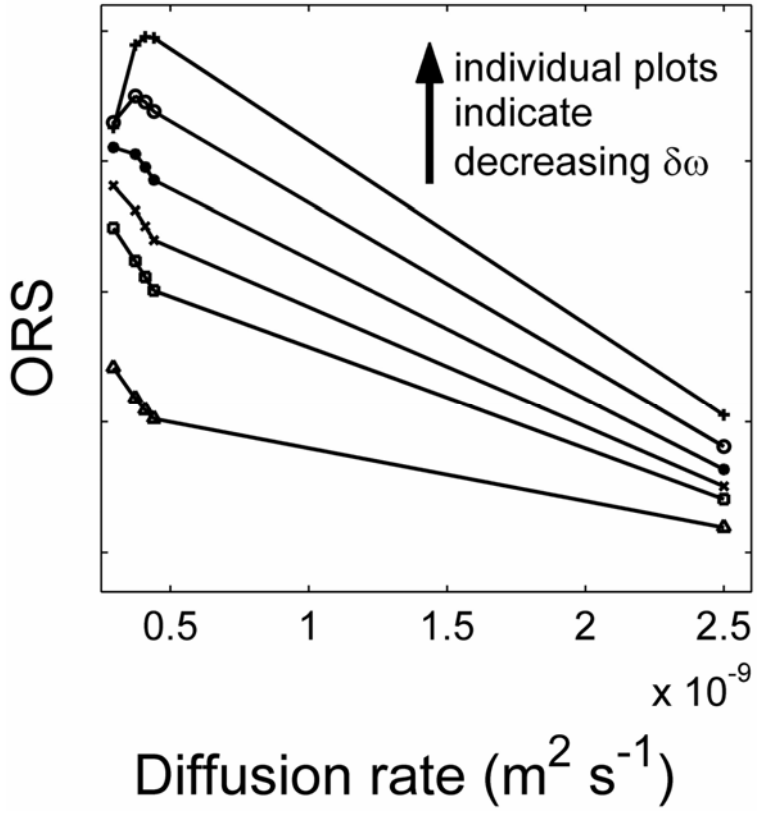

Figure 3.12: Plots of model showing nonlinear dependence of ORS on diffusion rate. Each plot corresponds to a single offset frequency. Increased ORS is observed for lower diffusion constants as well as lower offset frequencies. These trends are in agreement with experimental data.

The dependence on diffusion suggests the possible use of ORS as a method to estimate diffusion rates using SPIO. In clinical applications, this approach may be useful in organs and diseases where diffusion may be altered by pathology. As discussed earlier, these include ischemic lesion follow-up and differentiation between tumors and

abscesses. Further development of the above model, along with numerical simulation can be carried out to gain additional insight into this effect.

In order to achieve a higher offset frequency, the magnetic moment of the particle may be increased. There is a tradeoff, however, as larger particles are more likely to interfere with cellular functions rendering them less desirable for many molecular imaging applications, where targets may be clustered on cell-surfaces or within the cell itself.

In the present work, a Gaussian pulse was applied every TR and the steady state magnetization thus depends on the pulse width and energy of applied RF and magnetic characteristics of particles. Just as in the case of chemical exchange agents [84], this effect is dependent on power of irradiation. It is expected that optimal irradiation may depend on the particle characteristics because of both differing magnetic properties and differing coating characteristics, which influence diffusion around the particle. It is also possible that contrast agents employing both chemical exchange and ORS may be created to provide compound effects.

Conclusions

This work describes and demonstrates an off-resonance saturation approach to probe the effect of superparamagnetic particles. This method allows for the generation of an image in which there is a positive correlation between image intensity and superparamagnetic nanoparticle concentration. The ORS effect is not limited to the volume of the spins at a particular frequency offset, but is amplified by diffusion in the duration of the saturation pulse. Given that the full width at half maximum of the pulse (3 ms) is several folds longer than that (0.7 ms) of the off-resonance excitation pulse [77], the ORS effect is expected to be proportionally larger. In addition, the effect is highly dependent on diffusion suggesting that the approach may be useful in situations where diffusion may be altered by pathology.

CHAPTER 4

AN MRI REPORTER BASED ON THE BACTERIAL MAGNETOSOME

Background

The term “magnetotactic bacteria” refers to many different species of bacteria that make chains of magnetic crystals called “magnetosomes” inside their cells. These bacteria move along the lines of a magnetic field in a process called “magnetotaxis”. It was this unique property that led to the initial identification of these bacteria from Cape Cod marshes more than thirty years ago [86] and the subsequent discovery of the magnetosome. These structures are comprised of a magnetic iron oxide crystal core, surrounded by a phospholipid membrane. Each species of magnetotactic bacteria has a different, but specific, type and shape of magnetosome. However, due to their difficulty to isolate and maintain in culture, only a small portion of magnetotactic bacteria have been studied [87]. Although the complex biological process is not fully understood, there are numerous practical applications of such precise and uniform magnetic nanoparticles in research and industry.

These biologically produced, magnetic particles affect the MRI signal in the same way as synthetic superparamagnetic iron oxide (SPIO) nanoparticles [20] which have already been used for targeted molecular imaging applications [7-11]. One major application of these SPIO nanoparticles is the *in vivo* tracking of stem cells [22, 23] and tumor progression [11]. Labelling non-phagocytic cells in culture using modified particles, followed by transplantation or transfusion in living organisms, has made it possible to monitor cellular distribution *in vivo*, including cell migration and trafficking. A limitation of this approach is the need to label cells *in vitro* with pre-synthesized nanoparticles prior to cell transplant. As a result, particle concentration within cells decreases over time as the cells grow, migrate, and divide and particles cannot be readily linked directly to *in vivo* gene expression.

One way to overcome this is to utilize a genetic approach. GFP is perhaps the most well-known genetic marker for optical imaging. Magnetic resonance spectroscopy (MRS) has been used to detect creatine kinase [88] and chemical shift imaging (CSI) to observe beta-galactosidase [89] activity. MRI reporter strategies thus far have focused primarily on the detection of beta-galactosidase activity [90, 91] and expression of natural iron homeostasis proteins such as the transferrin receptor [92] and ferritin [93]. For the transferrin receptor approach, administration of exogenous transferrin coupled to magnetic particles is required. Thus far, only ferritin exists as a purely *in vivo* MRI marker, but its relaxivity is approximately 700 times lower than that of magnetite/maghemite (iron oxide) particle solutions [94], leading to the desire for a

genetic approach to produce iron oxide relaxation agents. This has led to the desire to seek out a gene reporter for MRI based on the genetics of the bacterial magnetosome.

The ability to produce magnetic nanoparticles, of the same composition as synthetic SPIO preparations, in a novel host cell type would open up the possibility of many additional biotechnological applications. For instance, many molecular imaging applications envision targeting contrast agents to specific receptors or cell surface ligands and disease specific markers. Iron oxide particles are also used in the manufacture of magnetic tapes and printing ink, magnetic targeting of pharmaceuticals, and for cell separation [95]. Synthetic particles, however, are often non-uniform, non-homogeneous in composition, and difficult to disperse evenly in solution. One possible solution could be to replace these particles with isolated bacterial magnetosomes. Advantages of this approach over synthetic nanoparticle production include uniformity and potential lower cost of the bacterial magnetosomes. Additionally, the phospholipid membrane surrounding the particles renders them water soluble, a difficult achievement for many synthetic nanoparticle processes. In fact, various applications of isolated magnetosome particles have already been explored. Magnetosomes have been conjugated to antibodies and used to detect and remove *E. coli* cells from bacterial suspensions [96] as well as in the detection and quantification of the immunoglobulin, IgG [97].

The major limitation of this approach, which would require growing magnetotactic bacteria in large quantities, is the sensitivity of magnetotactic bacteria to oxygen, making these strains difficult to isolate and maintain in culture [87]. Particles

formed in novel cell types, by engineered biological processes, could potentially replace these sources of particles without the need for extreme temperature, pH, and pressure protocols often required for industrial synthesis of iron oxide nanoparticles, nor the need for low-oxygen culture techniques for preparation of native magnetosomes.

It is likely that natural magnetosome production requires multiple genes. Recent work has identified a 98 kb genomic island [98], among other regions, in the *Magnetospirillum* sp. strain AMB-1 related to magnetosome regulation, and iron response studies have revealed 464 upregulated and 263 downregulated genes [99]. Our efforts here focus on *magA*, a gene known to be involved in the production of magnetosomes in *M. magneticum* [87, 100, 101]. Nakamura and co-workers [100, 101] found that *magA* encodes a protein with high sequence homology to the cation-efflux proteins, KefC, a K^+-translocating protein in E. coli, and NapA, a putative Na^+/H^+ antiporter from *Enterococcus hirae*. With *magA* expressed in *E. coli*, inverted membrane vesicles prepared from these cells were shown to transport Fe(II) in an energy-dependent manner, leading to accumulation of Fe(II) in the vesicle. These observations indicate that MagA functions as an H^+/Fe(II) antiporter in *M. magneticum* AMB-1 (Figure 4.1). Consistent with this, a recent full genomic analysis of *M. magneticum* AMB-1 found deletions in *magA* among a set of nonmagnetic mutants [102]. Although the complete process of magnetosome formation is not fully understood, it is clear that MagA plays a critical role.

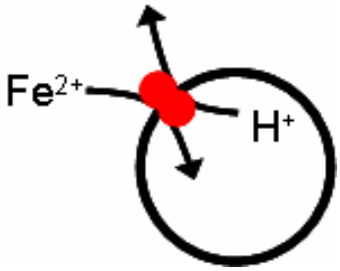

Figure 4.1: MagA is a transmembrane protein. MagA is thought to function as an iron transporter by exchanging Fe^{2+} with H^{+} thereby concentrating iron within vesicles.

Initial Transfection Results

In order to test the magnetosome concept, the gene was initially cloned into a test vector consisting of *magA* expressed under the constitutively expressed cytomegalovirus (CMV) promoter for transfection studies. These results show initial testing prior to cloning the gene into an inducible vector for long-term study. This test vector contained m*agA* under control of the CMV promoter with IRES-GFP so that positively transfected cells could be identified by fluorescence. A control vector contained the GFP protein under control of the constitutively expressed CMV promoter.

293FT cells were grown under standard culture conditions using Dulbecco's Modified Eagle Medium (DMEM) supplemented with 10% Fetal Bovine Serum (FBS), L-Glutamine, Penicillin, and Streptomycin. Calcium phosphate transfection was used to deliver the *magA* vector as well as the control vector. Untransfected cells were also

maintained as an additional control. Following transfection, media was replaced and the cells were allowed to incubate for an additional 24 hours. Transfection efficiencies of greater than 50% were observed by fluorescence microscopy. Cells were then divided into separate plates and one-half of each sample was incubated an additional 48 hours in media supplemented with 50 μM ferric citrate as a source of iron. The remaining half of each cell sample was incubated in standard media.

Cells were then trypsinized and collected. 10^7 cells were counted from each sample and spun for 2 minutes at 1000 rpm in 15 mL falcon tubes. Cells pellets were imaged using a Siemens 3T Trio MR scanner. T2 times were calculated using a Carr-Purcell-Meiboom-Gill (CPMG) sequence. Figure 4.2 shows the relaxivity results. There are eight total samples. Samples 1 and 2 show that iron supplied in the media cannot by itself alter relaxivity. This is expected since the free iron does not form a great enough magnetic moment in comparison with the magnetic domains formed by crystalline iron oxides. Samples 3-8 contain cells and all have increased relaxivity when compared to the media only samples. Samples 3 and 4 show that cells alone cannot form iron oxide crystals, even when supplemented with iron. Sample 5 shows that cells transfected with the *magA* gene do not form iron oxide crystals without the addition of a source of iron. Sample 6 shows that both *magA* gene transfection and iron supplement do result in the formation of structures capable of altering relaxivity. Samples 7 and 8 show that transfection with a control plasmid not containing *magA* is not sufficient to alter relaxivity.

1	Media only (no Fe supplement)
2	Media only (50μM Fe supplement)
3	293ft (no transfection, no Fe supplement)
4	293ft (no transfection, 50μM Fe supplement)
5	293ft (transfected MagA, no Fe)
6	293ft (transfected MagA, 50μM Fe supplement)
7	293ft (transfected EGFP only, no Fe supplement)
8	293ft (transfected EGFP only, 50μM Fe supplement)

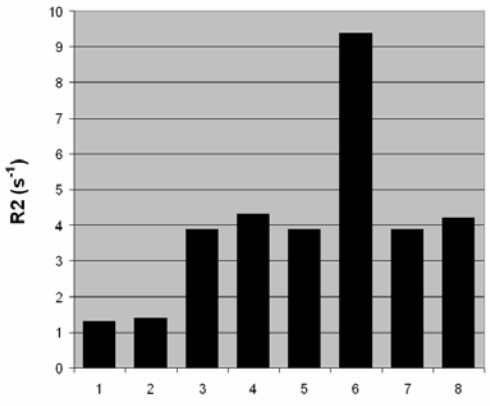

Figure 4.2: Initial relaxivity testing. Relaxivity for samples measured using CPMG sequence on 3T Siemens TRIO.

Figure 4.3 shows two images taken from the CPMG sequence used for T2 measurement. Figure 4.3b indicates that at an echo time of 125 ms, the sample containing cells transfected with *magA* and supplemented with iron has induced signal decay sufficient to differentiate it from all other samples. This indicates the feasibility of using T2 weighted imaging to identify cells prepared in the described method.

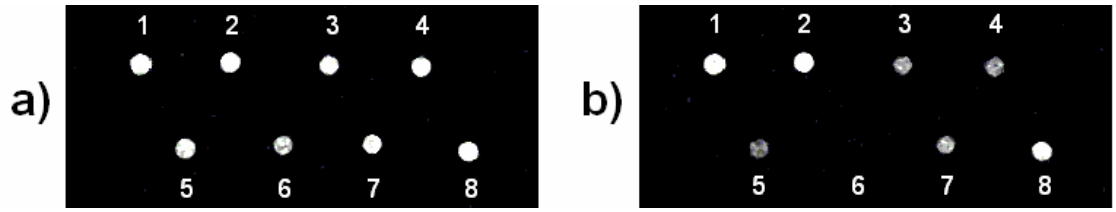

Figure 4.3: Images from CPMG sequence. a) Echo time 25 ms. b) Echo time 125 ms. See Figure 4.2 for sample descriptions numbered 1-8. At 125 ms (b), the cells transfected with *magA* and supplemented with iron (sample 6) can be clearly identified on the image in comparison to other samples.

Figure 4.4 shows iron staining of cells transfected with *magA*. The blue color of Figure 4.4d and 4.4e indicates the presence of iron.

Figure 4.4: Histology of whole cells using iron stain (Prussian blue) with nuclear fast red counter-stain. a) 293FT cells without Fe supplement (20X), b) 293FT cells with Fe supplement (20X). c) 293FT cells transfected with *magA* without Fe supplement (20X). d) 293FT cells transfected with *magA* with Fe supplement (20X). e) higher magnification (60X) of 293FT cells transfected with *magA* with Fe supplement. The sample with *magA* and iron supplement showed a blue color indicating the presence of iron. Cells were washed twice with PBS prior to mounting.

In vivo production of magnetic nanoparticles via *magA* expression

In order to demonstrate the production of magnetic nanoparticles in a mammalian system, the *magA* gene was expressed in a tetracycline/doxycycline inducible lentiviral vector. In addition to achieving stable cells capable of expressing *magA*, the inducible system allows specific control of *magA* gene expression in response to doxycycline. In this way effects of *magA* expression could be systematically studied by varying doxycycline administration. A clonal cell line, 2B5, was established from 293FT cells, following viral infection and confirmed by the presence of *magA*. This cell line was used in subsequent experiments described below.

To analyze the imaging potential of this cell line, MRI studies were performed in cell culture with and without the expression of *magA* by the addition of doxycycline, as well as with and without iron supplement as a source for producing the iron-oxide nanoparticles. The inset in Figure 4.5a shows two images taken from a multi-echo, Carr-Purcell-Meiboom-Gill (CPMG) sequence. Because iron-oxide particles shorten T2, the MRI signal in nanoparticle containing cells decays with echo time (TE) faster than that of normal cells, resulting in a darkening of the image and readily detectable contrast. The transverse relaxation rate (R2, $R2 \equiv 1/T2$), calculated from the imaging data, is also shown in Figure 4.5a. These results demonstrate no change in R2 without induction of gene expression and a significant increase in R2 upon induction and supplementation of iron. This cell line has been passaged continuously over 8 months with stable integration of the *magA* gene (verified by PCR) and exhibited consistent relaxation rates at all passages.

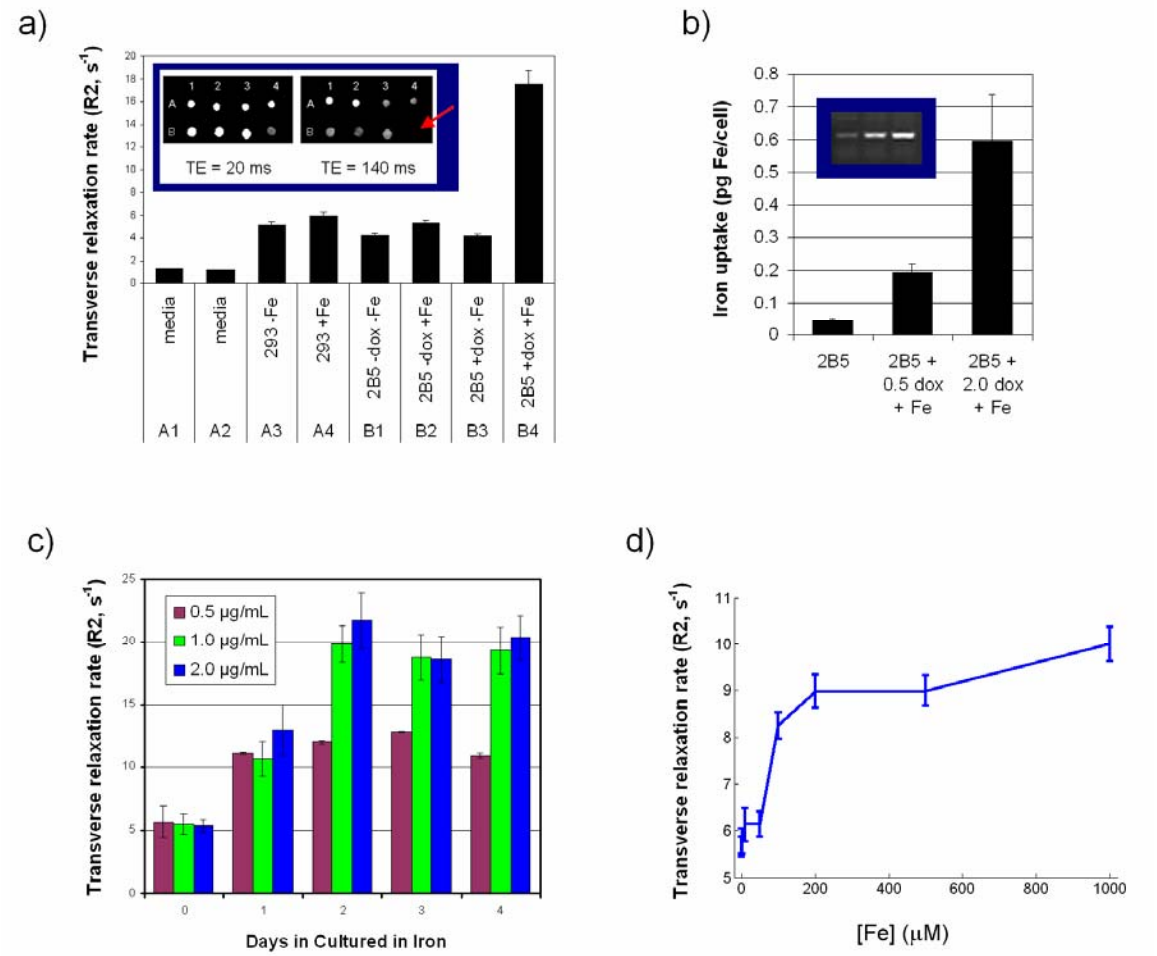

Figure 4.5: MRI of *magA* cell line. a) Transverse relaxation rates (R2) of cell cultures. Increased R2 indicates greater effect on MR signal. Cell line 2B5 shows no change in MR signal without induction and an approximately four-fold increase in R2 upon induction. Error bars are ± s.e.m. Inset shows T2-weighted images taken from CPMG sequence. These images show cell line 2B5 is capable of producing magnetic nanoparticles in sufficient quantities to create a visible contrast by MRI. At the shortest echo time (TE), all cells samples are bright, but as TE increases, cells producing nanoparticles exhibit attenuated signal in contrast to normal cells. The red arrow indicates the sample with the greatest relaxivity, 2B5 induced with doxycycline and supplemented with iron. b) Iron uptake in pg Fe/cell for 2B5 cells grown in various concentrations of doxycycline. Error bars are ± s.d. These differences are significant at $p<0.05$ for by two-tailed t-test. Inset shows results of RT-PCR detecting mRNA transcript of *magA* in 2B5 cells incubated with no dox, 0.5 µg/mL, and 2.0 µg/mL dox. c) Cell culture experiments indicating that a maximum R2 is achieved with a combination of 1.0 µg/mL doxycycline and incubation in iron for two days. Error bars are ± s.d. d) Iron-dosing results showing strong dependence on iron concentration below 200 µM Fe and less dependence above 200 µM for *in vitro* cell culture. Error bars are ± s.d.

To assess the iron uptake by these cells, an o-phenanthroline absorbance assay to measure average iron incorporated was used. The results in Figure 4.5b show an iron uptake of 0.59 ± .14 pg Fe/cell for cells incubated with 2 μg/mL doxycycline and 200 μM Fe for four days. This value fell to 0.19 ± .03 pg Fe/cell for cells incubated with 0.5 μg/mL doxycycline and 0.04 ± .01 pg Fe/cell for cells incubated without doxycycline. Note that the iron uptake shows a correlation with *magA* expression as detected with RT-PCR measurements shown in the inset (Figure 4.5b). This, taken together with relaxation rates measurements (Figure 4.5c), translates to a cellular relaxivity of R2 = 15.6 ± 1.8 mM^{-1} Fe^{-1} in cells at 3 Tesla. The iron uptake of 0.59 ± .14 pg Fe/cell found here is slightly lower than, but comparable to the iron uptake for transferrin-mediated MION uptake (range 0.61 – 1.54 pg Fe/cell) reported previously [9].

Figure 4.5c shows MR transverse relaxivity (R2) data from doxycycline dosing experiments on the cell line. These studies were conducted to gain insight into the induction of nanoparticle formation, as well as the amount of incubation time needed in the presence of doxycycline and iron media supplement. Of primary concern for assessing the feasibility of this approach for *in vivo* imaging is the ability to easily induce cells and the ability for the nanoparticles to form within a reasonable time frame. At 0.5 μg/mL doxycycline, the relaxivity increases from control, but reaches a plateau after one day of incubation with iron. At 1.0 and 2.0 μg/mL doxycycline, relaxivity increases nearly twice as high as with 0.5 μg/mL, to approximately 20 s^{-1}, reaching a plateau after two days of incubation with iron. According to these data, a maximum effect on MR

signal is reached with a combination of doxycycline at 1 μg/mL and two-day incubation in iron media (200 μM Fe). Figure 4.5d shows results of iron dosing response. As noted above, the maximum R2 achieved at a doxycycline dose of 0.5 μg/mL was not as high as that at larger doxycycline doses, even after allowing for increased time for the nanoparticles to form. In order to test whether increased iron supplement can overcome this barrier, iron supplement was varied for cells incubated with 0.5 μg/mL doxycycline (24 hours induction, followed by four day iron incubation). The results in Figure 4.5d indicate that although at very low concentrations, R2 increases with iron concentration, it levels off beyond an iron concentration of 200 μM. These dosing studies indicate that both gene expression level and iron availability are important factors in inducing R2.

In order to visualize the magnetic nanoparticles produced, electron microscopy was performed on the cell line after four days of induction and incubation with 200 μM ferric citrate (Figure 4.6). Because iron oxide is not as electron dense as gold and silver particles often used in electron microscopy, the iron oxide particles exhibit a moderate contrast in the cells. It is first noted that the particles are approximately 3-5 nm in diameter, spherical in shape, and homogeneous in size. Secondly, although magnetotactic bacteria tend to form magnetosomes in chains, here the particles do not appear in such a configuration. This can be expected as the anchoring of magnetosome vesicles to filaments within the cell, thereby creating the chain-like formations, is likely to be mediated by other magnetosome-related genes [103, 104]. Although the formation of chains and signal transduction of magnetic field into directed cell motility are necessary

functions for bacteria, they are not necessary for nanoparticle formation via the expression of *magA* and are not needed for MRI and other biological applications.

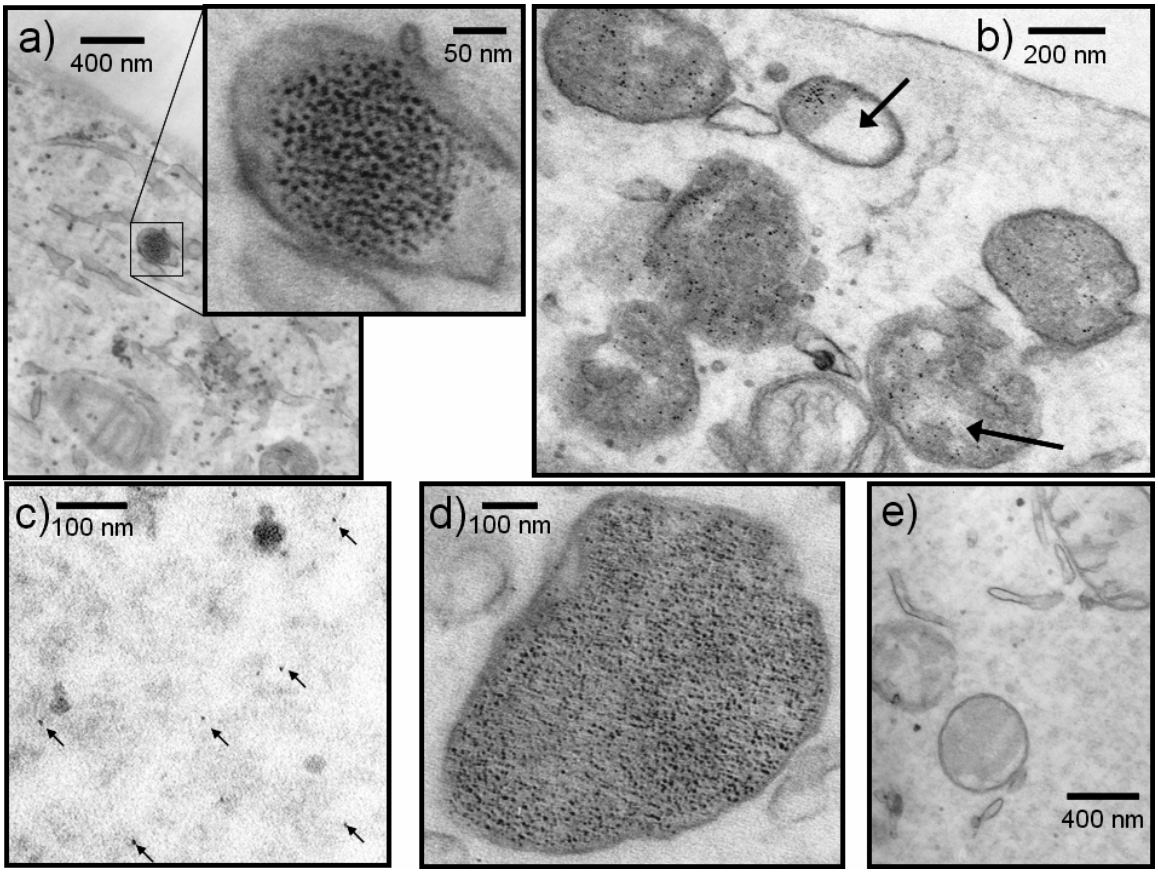

Figure 4.6: TEM images of cell line 2B5. Nanoparticles can be found within membrane enclosed vesicles. These vesicles, resembling endosomes, can be found individually (a) or in groups (b), with varying numbers of particles within, as can be seen when comparing vesicles in panels (b) and (d). Arrows in panel (b) show compartmentalization resembling the multivesicular bodies of the cellular degradation pathway. Particles can also be seen outside the vesicles (c), although they are less visible individually. Panel (e) shows uninduced cell line 2B5, lacking these magnetic particles.

As shown in Figure 4.6, in the gene-transferred cells, although particles can be found throughout the cell, they are most easily identified within membrane-enclosed structures. This clustering, leading to effectively larger magnetic particles, may in fact enhance the transverse relaxation effects of the nanoparticles on the MRI signal [44]. In Figure 4.6, these structures are often found near one another and often near the cell membrane with a varying number of magnetic particles within. As marked in Figure 4.6b, many of these structures appear to be compartmentalized, resembling endosomes known as multivesicular bodies [105]. In these structures, these various compartments are known to indicate the sorting of material to be degraded [106], suggesting that particles here may be directed towards a cellular degradation pathway.

Nevertheless, the exact fate of the particles produced here remains unknown. After MR imaging, cells incubated for an additional ten days without doxycycline or iron show a return to control values for relaxivity (data not shown). It is possible that, in the absence of new particle formation, the already-formed particles have simply been diluted by continued cell division. It is also possible that low pH, such as that present in maturing endosomes, breaks down the magnetic nanoparticles. In fact, lowering the pH to dissolve synthetic iron-oxide particles is often the first step in determining iron concentration for magnetic nanoparticles [41]. This possibility raises concern of potential adverse affects on cellular iron homeostasis and cell viability.

In order to address such concerns, a series of proliferation and cytotoxicity assays were performed at varying levels of gene induction with and without iron supplement. With a G6PD assay, no difference in the release of cytosolic G6PD was found among the different conditions (Figure 4.7a); as increased cytotoxicity would mean increased G6PD release, this result indicates absence of cytotoxicity with *magA* expression and iron uptake. Mitochondrial activity, hence cell proliferation, was assessed with a tetrazolium salt (MTT) assay and shows no statistically significant decrease in cell proliferation due to *magA* expression and iron uptake (Figure 4.7b). In addition, *magA* expression and iron uptake did not increase apoptosis (Figure 4.7c).

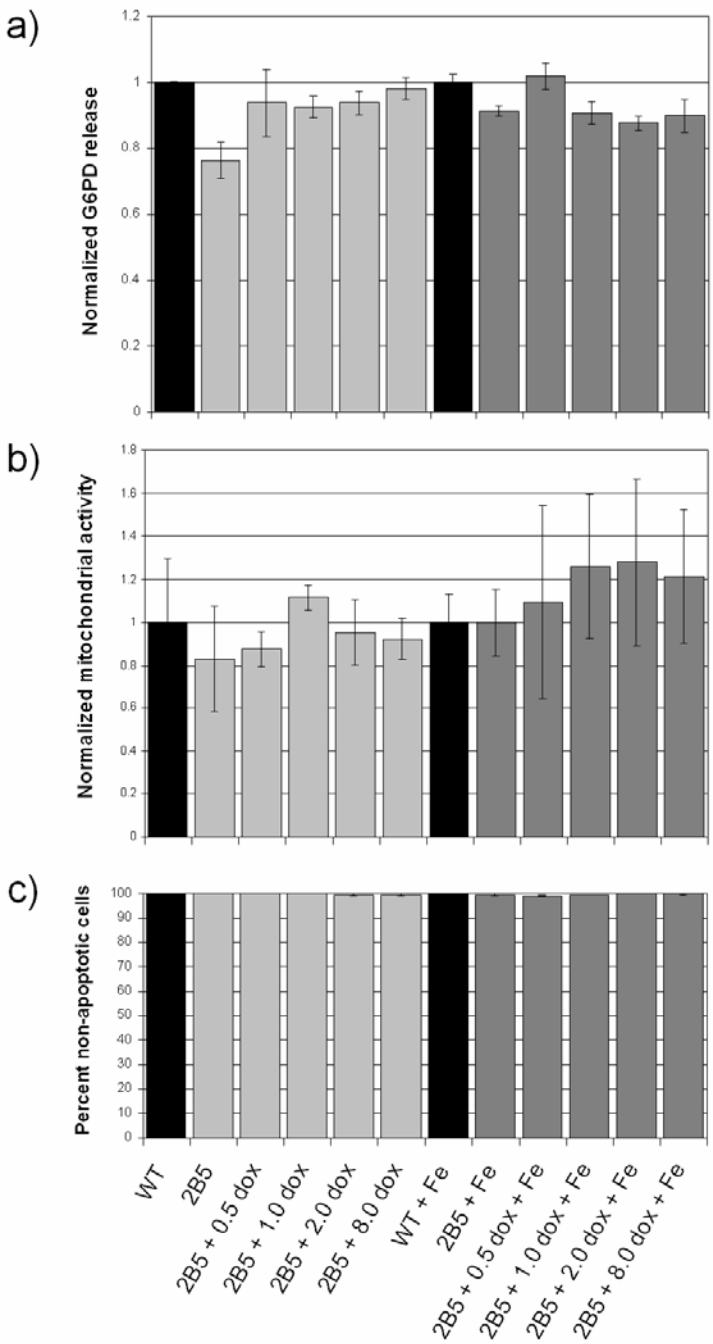

Figure 4.7: Results of cytotoxicity assays on 2B5 cell line. a) Results of G6PD assay showing no increased cytotoxicity as measured by G6PD release into medium. b) Results of MTT assay showing no significant decrease in cell proliferation. c) Results of apoptosis assay showing no increase in cellular apoptosis. Error bars are ± s.d.

To further characterize these nanoparticles, they were isolated from the cells using magnetic separation. Specifically, the cells were ruptured by incubating in water and vortexing, and the particles were pulled together from the cell debris via a small, iron-neodymium-boron magnet (Figure 4.8). In Figure 4.8b, particles can be seen aligned along magnetic field lines, depending on the direction of the magnet, much as what happens when iron filings are brought near a magnetic source.

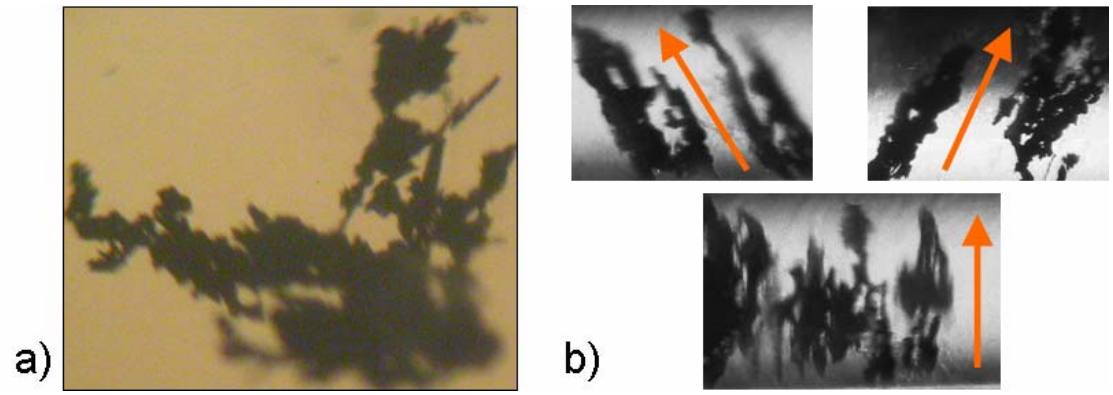

Figure 4.8: Magnetic nanoparticles isolated from mammalian cells. a) Magnetic nanoparticles can be isolated from cells by rupturing the cell membrane and using magnetic separation from cell debris. b) By application of a magnet (not seen in photo), these particles align along the field lines, in the direction of the magnetic field (indicated by arrow).

Figure 4.9 shows the results of X-ray powder diffraction (XRD) analysis of these particles. The results show the particles consist primarily of magnetite (Fe_3O_4) which is the form of iron oxide found in the magnetosomes of naturally occurring magnetotactic bacteria.

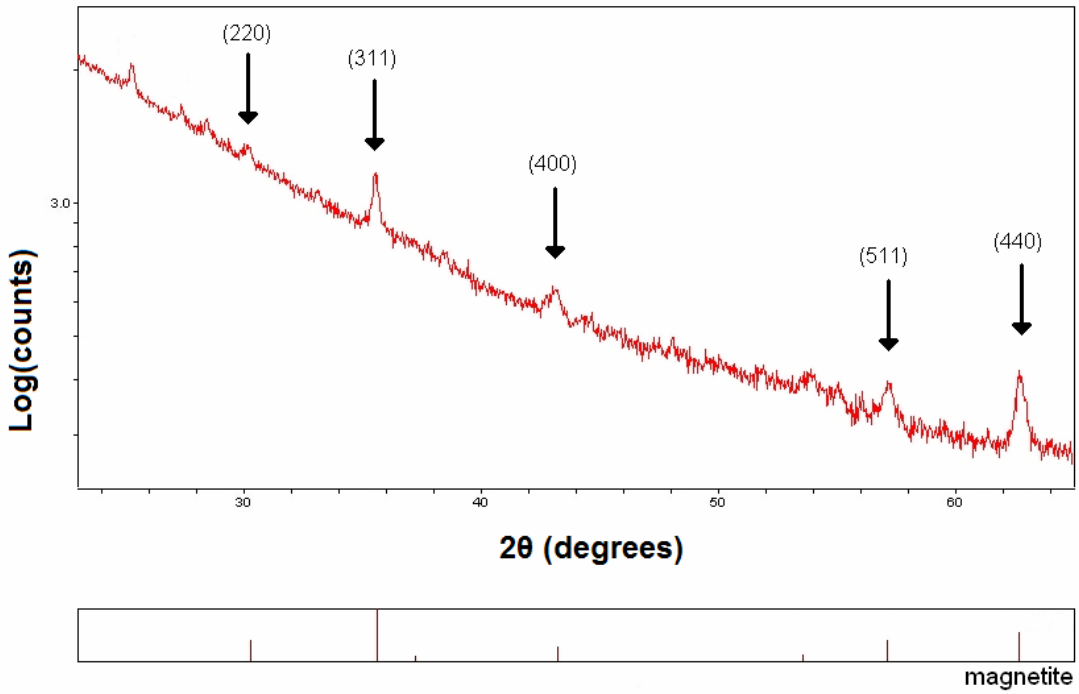

Figure 4.9: X-ray powder diffraction analysis of isolated nanoparticles. Arrows indicate important magnetite peaks. Numbers in parentheses are Miller indices of the reflections for major peaks of magnetite. Note that raw data, without baseline correction, is shown and the vertical scale is logarithmic making peak heights not readily comparable.

The fact that a single bacterial gene can lead to the formation of magnetic nanoparticles in a mammalian cell is an unexpected finding, raising questions to be answered. For instance, the exact process of particle formation remains unknown, although data in existing literature may shed some light in this regard. It is known that the MagA protein is present in both the cytoplasmic and magnetosome membranes of M. magneticum strain AMB-1 [101], and recent work showing that magnetosome vesicles are initially formed as invaginations of the cell membrane appears to confirm this [104]. MagA protein in the bacteria is therefore thought to concentrate iron within the vesicle.

The uptake of iron into the cell, however, is likely to be dependent on the cell type hosting the *magA* gene. Tissue culture studies of human cells [107] show direct transport of ferrous iron, Fe(II), which is soluble at physiological pH but rapidly oxidized to ferric iron in an aerobic environment. For the magnetotactic bacterium, M. magneticum AMB-1, it was found that ferrous sulphate and ferric gallate as iron sources enhanced magnetosome yield as compared with ferric quinate, an iron chelate often used, and it has been postulated that the size regulation of magnetite could be controlled by the coprecipitation of Fe(II) and Fe(III) via alkalization, much as can be found in *in vitro* methods [108]. The difference in iron environment of 293FT cells and magnetotactic bacteria is therefore one possible reason for the smaller size of the particles created here. In magnetotactic bacteria, magnetosomes are on the order of tens of nanometers in size whereas the particles here are only a few nanometers in diameter. It is also possible that there exist yet unknown genetic mechanisms by which specific magnetotactic bacterial strains are capable of maintaining their individual magnetosome dimensions.

One critical question for *in vivo* application is whether the formation of magnetic nanoparticles can occur *in vivo*. For *in vivo* experiments utilizing *magA* expression, cells must be able to make use of endogenous iron sources. Although ferritin expression has been shown to sequester endogenous iron, suggesting the availability of ionic iron *in vivo*, the precise source of iron remains unknown.

To show that the conditions for forming magnetosomes can be met *in vivo*, an experiment was conducted to demonstrate that cells can produce particles utilizing

endogenous iron sources after implantation. Here, cells were transplanted into the mouse brain. This model allows for a contralateral injection of control cells which can then be found on the same section by MRI and histology, in a single imaging acquisition. Additional rationale includes the reduced immune response of the brain, and its use in prior MRI studies of magnetic nanoparticle-based cell imaging [22, 93]. Uninduced 2B5R cells (a clonal cell line derived from 2B5 cells which constitutively expresses DsRed, see Methods) were transplanted into the mouse brain, along with a contralateral control transplantation with 293FT cells inducible for GFP with doxycycline. Cells were allowed to grow for five days post-transplantation during which they were induced via continuous supply of doxycycline in drinking water and food but without iron supplementation and subsequently imaged. Figure 4.10a shows the results of T2*-weighted imaging in one representative animal. On the right side of the figure (white arrow), *magA* positive cells induce significant MR signal loss while the GFP inducible cells, which do not express *magA*, do not show significant MR contrast on the contralateral side. The fluorescence histology in Figure 4.10b shows that GFP was in fact induced in control cells, confirming the delivery of doxycycline to the cells. The red fluorescence on the right side of Figure 4.10b confirms the presence of *magA* positive cells in conjunction with the location of these cells as seen by MRI in the figure.

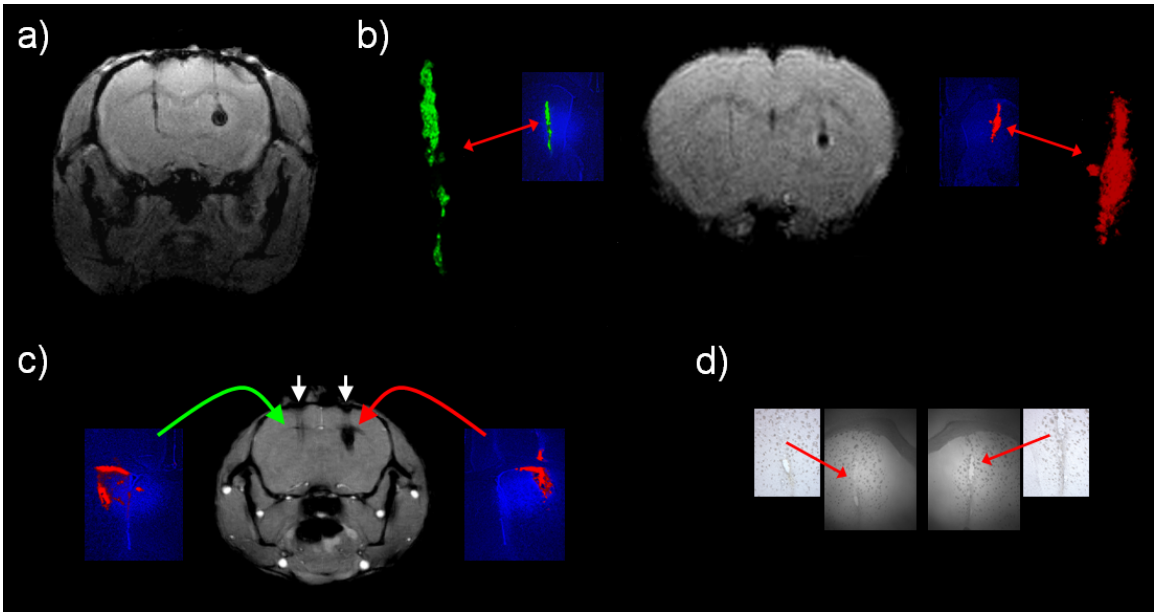

Figure 4.10: MRI of *magA* cells induced *in vivo*. a) T2*-weighted image of mouse brain with transplanted *magA* cells (right) and GFP control cells (left) after 5 days induction. These cells were neither induced nor incubated with iron supplement prior to transplantation. The *magA* cells (white arrow) exhibit significantly lower MRI signal, reflecting an increase in R2, suggesting that *magA* cells are able to use endogenous iron sources. The control cells on the left do not show such an effect. b) MRI of same mouse brain showing *magA* cells can still be readily seen by T2-weighted imaging, which is less sensitive than T2* with regard to magnetic nanoparticles. The fluorescence histology (not exactly registered to the MR image) confirms the presence of control (green) and *magA* positive (red) cells. Magnified green and red channels are also shown. c) T2* weighted MRI of transplanted 2B5R cells. Cells on the left were uninduced prior to the transplantation and those on the right were pre-induced in iron supplemented culture (magnetic particles formed in culture, prior to transplant). MRI images were obtained right after the transplantation. The similarity of the right side of Fig. 4a to that of Fig. 4c confirms that *magA* expression *in vivo* (utilizing endogenous iron) leads to similar MRI effects as that in iron supplemented culture. Fluorescence histology confirms the presence of 2B5R cells in both locations, however only cells on the right are capable of affecting the MR signal. White arrows indicate bore sites for the cell transplant. d) Brightfield histology section of the brain in (b) indicating the site of transplanted cells.

T2*-weighted imaging is often used for cell tracking because it is more sensitive to the field inhomogeneities created by magnetic nanoparticles [20], but it can exaggerate the spatial extent of cells. In Figure 4.10b, a T2 weighted image of the same slice as shown in Figure 4.10a is presented. The 2B5R cells produce sufficient particles *in vivo* to be detectable by T2-weighted imaging, which, although less sensitive to magnetic nanoparticles, shows a more representative spatial extent of the cells and may prove useful for future applications where better quantification is desired.

Figure 4.10c shows the results of a separate experiment intended to serve as a control, conducted to confirm that the observed MRI contrasts in Figure 4.10a are indeed due to the formation of magnetic nanoparticles in cells. In this experiment, the mouse was transplanted with uninduced 2B5R cells on one side (left side of image) and with 2B5R cells that were pre-induced and allowed to form magnetic nanoparticles in culture prior to transplantation on the contralateral side. Imaging was performed right after transplantation, without *in vivo* doxycycline induction. Fluorescence histology shows the presence of 2B5R cells on both sides, however, only induced cells on the right side are seen in MRI. The MRI contrast for the cells with particles formed *in vitro* (right side Figure 4.10c) is consistent with that shown on the right side of Figure 4.10a, confirming the particle formation (right side Figure 4.10a) in the *in vivo* induction experiment.

The needle tracks, likely containing edema due to the trauma of the injection, can be seen in all cases but show much less contrast than the cells containing particles. Although bleeding due to the injection could potentially result in an MRI artifact

mimicking iron accumulation, this is unlikely the cause of contrast for the right side of Figures 4.10a-4.10c, as similar contrast is not found in the contralateral transplants, and additional histology (Figure 4.10d) shows the lack of bleeding at the site of cell transplantation.

For *in vivo* applications, the lowest number of cells detectable will depend on the particular imaging system and resolution used. By varying the percentage of positive cells in cell pellets, it was found that 20% and 10% positive cells results in R2 of 13.1 ± 1.0 and 11.1 ± 0.4 s^{-1} respectively. These values represent an increase of greater than 200% over wild type making a voxel containing one in five to one in ten cells detectable by MRI. This suggests that a single positive cell is potentially detectable in a 50×50×50 μm^3 voxel, consistent with the findings of Weissleder et. al. [109] for transferrin-mediated MION uptake via expression of the transferrin receptor.

Taken together, these experiments demonstrate that, for the brain, expression of *magA in vivo* alters relaxivity without the addition of an exogenous iron source. Whether this result can be generalized to other tissues remains to be demonstrated.

Methods

Molecular Biology

The *magA* gene (provided by L.E. Bertani, California Institute of Technology) was cloned into a doxycycline inducible lentiviral vector to control the expression of *magA*. In this way, MRI changes could be correlated with gene expression via doxycycline administration. *magA* was constructed downstream of a tetracycline response element (TRE) under the control of a $_{mini}$CMV promoter activatable by rtTA2s-M2 (obtained from Dr. W. Hillen). The woodchuck hepatitis virus post-transcriptional regulatory element (WPRE) at the 3'LTR and an HIV-flap element at the 5'LTR were used. Replication defective lentivirus was generated by co-transfection of this vector, pΔ8.9 (composed of structural genes for virion assembly; obtained from Dr. C. Lois, MIT) and pVSV-G (Invitrogen, Inc.) into 293FT packaging cells (Invitrogen, Inc.). Culture medium was collected at 48 hours post transfection for 3 consecutive days at 24 hour intervals. The supernatant was centrifuged at 25,000 × g for 90 minutes. The viral pellet was re-suspended, aliquoted, titered and kept frozen at -80°C. This virus was used to infect 293FT cells. After several cell passages to ensure stable integration, single cells were picked and expanded to create clonal cell lines. Clonal cell lines were produced by suspending 200 cells in 20 mL and distributing into two 96-well plates. Wells resulting in single colonies were expanded into clonal cell lines. PCR was performed to confirm the presence of the *magA* gene to identify positive lines (Figure 4.11). Three clonal lines were evaluated for imaging and found to produce MRI signal changes. For the following experiments, one of these clonal cell lines, named 2B5, was used.

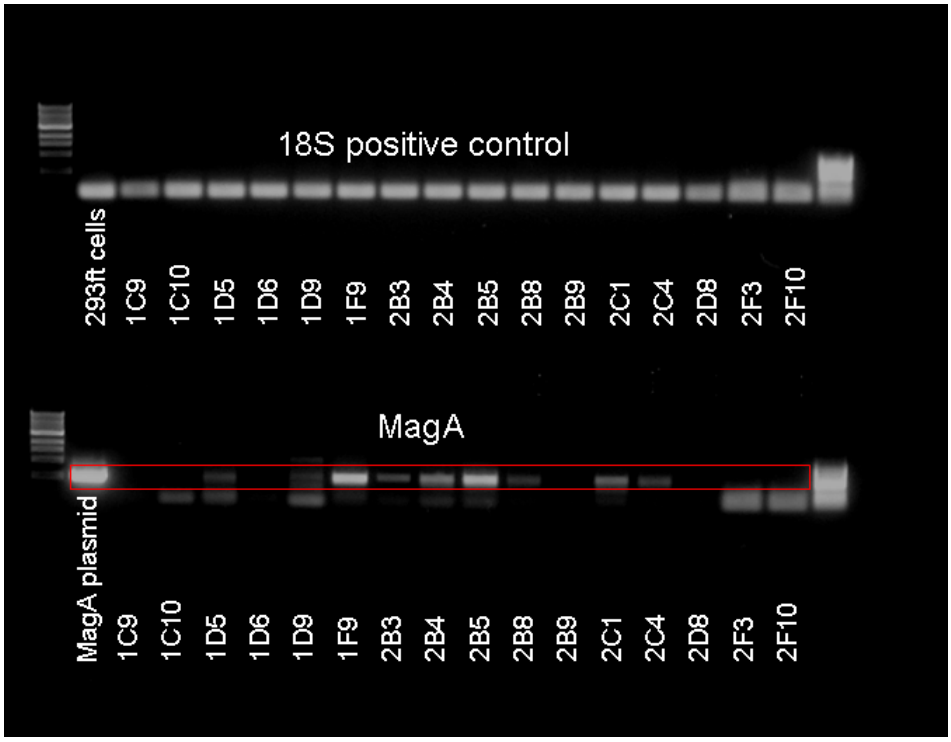

Figure 4.11: PCR results confirming the presence of *magA*.

MR Imaging of cells in culture

For cell culture imaging (Figure 4.5a), four plates were prepared for each cell line: 1) no doxycycline, no iron supplement, 2) no doxycycline, but with iron supplement, 3) with doxycycline, without iron, and 4) with doxycycline, with iron. The appropriate cell samples were incubated with 2 μg/mL doxycycline and/or 200 μM Fe (from ferric citrate) for four days. Error bars are ± standard error of measurement (s.e.m). For dosing experiments (Figure 4.5c), 2B5 cells were initially cultured under normal conditions. Doxycycline was added to media (0.5, 1.0 and 2.0 μg/mL) for 24 hours, after which media was removed and replaced with fresh media supplement with 200 μM iron (from

ferric citrate) for 1-4 days. For iron dosing (Figure 4.5d), cells were cultured with 0.5 μg/mL doxycycline for 24 hours, after which, media was removed and replaced with fresh media with varying iron concentration for four days.

In all cases, cells were trypsinized and collected. 10^7 cells in approximately 100 μl pellets were imaged using a Siemens 3T Trio MR scanner. T2 times and R2 (R2≡1/T2) were calculated by fitting the decay curves produced from a Carr-Purcell-Meiboom-Gill (CPMG) imaging sequence. For dosing experiments (Figure 4.5c and 4.5d), three measurements were made, and error bars are ± one standard deviation (s.d.). Imaging parameters were: TE = 20 – 400 ms in increments of 20 ms, TR 1500 ms, FOV 128×128, 0.5 mm in-plane, and a slice thickness of 1 mm. Image processing and analysis were performed using MATLAB processing software. Some statistical analysis was performed in Excel.

Iron uptake determination:

Iron uptake was determined using an o-phenanthroline procedure modified from a previously reported method [41]. 2B5 cells were grown under conditions of 0, 0.5 and 2.0 μg/mL doxycycline and 200 μM Fe for four days. Original 293FT cells were cultured in the presence of 200 μM Fe for four days to serve as a baseline. 2×10^6 cells were counted, pelleted, resuspended in water, and vortexed to rupture cell membranes. 0.15% v/v mercaptoacetic acid was added to each sample and incubated overnight prior to analysis. o-Phenanthroline was added, reaching a final concentration of 0.0075% w/v. Iron solutions for a standard curve were prepared from $FeSO_4$. Samples and standards

both contained 0.2% hydroxylamine hydrochloride to maintain iron in the 2+ state and sodium citrate (150 μL per mL of iron solution) to maintain an acidic pH for Fe-phenanthroline complex formation. Absorbance was read at 510 nm. Iron uptake due to *magA* was determined by subtracting total iron in the 293FT sample from the 2B5 test samples. Samples were measured in triplicate and error bars are given by ± s.d.

RT-PCR:

2B5 cells were grown under conditions of 0, 0.5 and 2.0 μg/mL doxycycline and 200 μM Fe for four days. First strand cDNA was created from DNase I-treated RNA using Superscript III (Invitrogen). Subsequent PCR was performed using *Taq* DNA polymerase (Invitrogen) over 35 cycles of 30 s at 94°C, 30 s at 60°C, and 30 s at 72°C. Primers utilized were forward: 5'-catcccgaactgacctatgc-3' and reverse: 5'-acgaacagcagcatcagc-3' resulting in a 200 base pair amplicon.

Electron microscopy:

2B5 cells were cultured with 2 μg/mL doxycycline and 200 μM Fe for four days. The cells were then fixed with 2.5% glutaraldehyde in 0.1 M cacodylate buffer followed by 1% OsO_4 in the same buffer. Cells were then dehydrated and embedded in Eponate resin. Ultrathin sections (60-70 nm) of cells were observed on a Hitachi H-7500 transmission electron microscope without counterstaining.

Cytotoxicity assays:

10^3 cells per well were plated in a 96-well plate and incubated for five days under the various conditions of doxycycline and with and without iron supplement as indicated in Figure 4.7. For the glucose-6-phosphate dehydrogenase (G6PD) assay which measures the release of cytosolic G6PD (increased release indicates cytotoxicity), 3 wells per condition were measured, along with a control in which the cells are lysed to release all G6PD into the assay medium (for quantification). Vendor protocol was followed (Molecular Probes/Invitrogen, Inc.). For the tetrazolium salt (MTT) assay, 4 wells per condition were measured according to vendor protocol (ATCC). For the apoptosis assay, 3 wells per condition were measured according to vendor protocol (Promega) with the modification of using Hoescht (5 minutes at room temperature), rather than propidium iodide to stain all cells (both apoptotic and nonapoptotic). Analysis was performed on Microsoft Excel, and error bars are ± s.d.

***In vivo* animal experiments:**

For *in vivo* particle formation experiments, a clonal cell line 2B5R was established by infection of 2B5 with a lentivirus containing DsRed under the constitutive control of the CMV promoter. Single cells were plated as above to produce the clonal cell line, 2B5R. In this way, cells could be also tracked via fluorescence imaging. Burr holes were made through the dorsal skull using coordinates chosen from a standard mouse atlas for injection into the striatum (+ 0.4 mm anterior and +/– 1.75 mm medial/lateral relative to bregma, and –2.5 mm ventral from dorsal surface of brain). For Figures 4.10a and 4.10b, uninduced 2B5R cells were transplanted into the mouse striatum shown on the

right. The contralateral side was transplanted with a 293FT cell line inducible for GFP, but not *magA*. In each case, the transplantation was made using a stereotaxic platform fitted with an automated injector and Hamilton syringe and using 10^5 cells suspended in a total volume of 4 μl in phosphate buffered saline (PBS). Cells were allowed to grow for five days, during which doxycycline was administered in the drinking water at 5 mg/mL and in the food at 200 ppm. On day 5, mice were imaged and sacrificed for histology. Three mice were studied with this protocol.

For the control experiment (Figure 4.10c), 2B5R cells were incubated in culture for four days with 2 μg/mL doxycycline and 200 μM Fe. In this way, cells produced magnetic nanoparticles in culture, prior to transplantation. Using the transplantation procedure described above, 10^5 of these pre-induced cells were transplanted (n=2 mice) on the right side of the brain. On the contralateral side (left side of image), 10^5 uninduced 2B5R cells were transplanted. In this case, imaging was performed immediately after transplantation.

In all cases, imaging was performed under anesthesia (1.5% isofluorane) on a 9.4T Bruker MR system fitted with a heated mouse cradle. MRI parameters for T2*-weighting are: FLASH sequence, TE 6.0 ms, TR 50 ms, FOV 256×256, 88 μm in-plane, slice thickness 0.450 mm and for T2-weighting: spin-echo sequence, TE 10.21 ms, TR 1000 ms, FOV 256×256, 86 μm in-plane, slice-thickness 0.654 mm. Animals were sacrificed post-imaging and brains collected for histology. Brains were fixed in 4% paraformaldehyde for one day, followed by two days in 30% sucrose. Tissue was

mounted in O.C.T. (Optimal Cutting Temperature) compound and 40 μm sections cut on a Leica CM3050S Cryostat (Nussloch, Germany). Sections were washed with PBS, stained with Hoechst for five minutes, and washed twice again with PBS, prior to mounting. Imaging was performed on an Olympus BX51 research microscope fitted with a Metamorph Imaging System. Figure 4.10d shows a brightfield image of the same section as seen in 4.10b, without any additional staining.

Conclusions

The ability to produce magnetic nanoparticles in a novel host cell type opens up the possibility of many additional biotechnological applications. For instance, many molecular imaging applications envision targeting contrast agents to specific receptors or cell surface ligands and disease specific markers. Synthetic particles, however, are often non-uniform, non-homogeneous in composition, and difficult to disperse evenly in solution, and the production of magnetosomes for biotechnological applications has been limited by the sensitivity of magnetotactic bacteria to oxygen, making these strains difficult to isolate and maintain in culture [87]. Particles formed by the expression of *magA* are highly uniform, and could potentially replace these sources of iron oxide particles. Additionally, particles produced by immune matched host cells will have less potential for triggering immune responses because they will not display foreign molecules to the subject of the imaging procedure. This is an advantage over simply

isolating and using magnetosomes from bacterial cells, as the coating derived from bacteria would contain molecules foreign to other animals and humans in which the contrast agent may be used. It may also be possible to modify the particle for targeting applications with genetic manipulation, rather than chemical modification, by expressing *magA* in cell lines which also express desired ligands/receptors on their membranes so that isolated particles would contain these molecules on their surface, thus avoiding the need to chemically attach such molecules to the contrast agent.

In summary, the present work sheds light on the process of natural magnetosome formation within the bacteria and opens up a new avenue for *in vivo* cellular and molecular imaging, including applications such as cell and transplant tracking, gene expression reporting by co-expressing *magA* with any gene of interest, and *in vivo* sensing of iron concentration. With a controllable system as described here, long-term MRI studies can be conducted in which uninduced cells are allowed to grow, migrate, divide and differentiate over a period of time in the absence of nanoparticle formation, minimizing the chances of the particles to interfere with normal cellular processes, and expression of *magA* can then be induced, to allow particles to form, just prior to imaging. Since MR imaging is non-invasive and the particles can be regenerated, *magA* based cell tracking and gene reporting allow new, longer term molecular imaging experiments not possible with traditional forms of contrast agents.

REFERENCES

1. Weissleder, R. and U. Mahmood, *Molecular imaging.* Radiology, 2001. **219**(2): p. 316-33.

2. Blankenberg, F.G. and H.W. Strauss, *Nuclear medicine applications in molecular imaging.* J Magn Reson Imaging, 2002. **16**(4): p. 352-61.

3. Shapiro, E.M., S. Skrtic, K. Sharer, J.M. Hill, C.E. Dunbar, and A.P. Koretsky, *MRI detection of single particles for cellular imaging.* Proc Natl Acad Sci U S A, 2004. **101**(30): p. 10901-6.

4. Slichter, C.P., *Principles of Magnetic Resonance*. 1980, Berlin: Springer.

5. Haacke, E.M., R.W. Brown, M.R. Thompson, and R. Venkatesan, *Magnetic Resonance Imaging: Physical Principles and Sequence Design*. 1999, New York: John Wiley and Sons.

6. Mornet, S., S. Vasseur, F. Grasset, and E. Duguet, *Magnetic nanoparticle design for medical diagnosis and therapy.* Journal of Materials Chemistry, 2004. **14**: p. 2161-2175.

7. Weissleder, R., *Target-Specific Superparamagnetic MR Contrast Agents.* Magnetic Resonance in Medicine, 1991. **22**: p. 209-212.

8. Remsen, L.G., C.I. McCormick, S. Roman-Goldstein, G. Nilaver, R. Weissleder, A. Bogdanov, K.E. Hellstrom, I. Hellstrom, R.A. Kroll, and E.A. Neuwelt, *MR of Carcinoma-Specific Monoclonal Antibody Conjugated to Monocrystalline Iron Oxide Nanoparticles: The Potential for Noninvasive Diagnosis.* American Journal of Neuroradiology, 1996. **17**: p. 411-418.

9. Moore, A., J.P. Basilion, E.A. Chiocca, and R. Weissleder, *Measuring transferrin receptor gene expression by NMR imaging.* Biochim Biophys Acta, 1998. **1402**(3): p. 239-49.

10. Bulte, J.W., S. Zhang, P. van Gelderen, V. Herynek, E.K. Jordan, I.D. Duncan, and J.A. Frank, *Neurotransplantation of magnetically labeled oligodendrocyte progenitors: magnetic resonance tracking of cell migration and myelination.* Proc Natl Acad Sci U S A, 1999. **96**(26): p. 15256-61.

11. Artemov, D., N. Mori, B. Okollie, and Z.M. Bhujwalla, *MR molecular imaging of the Her-2/neu receptor in breast cancer cells using targeted iron oxide nanoparticles.* Magn Reson Med, 2003. **49**(3): p. 403-8.

12. Josephson, L., J.M. Perez, and R. Weissleder, *Magnetic Nanosensors for the Detection of Oligonucleotide Sequences.* Angew. Chem. Int. Ed., 2001. **40**(17): p. 3204-3206.

13. Meiboom, S. and D. Gill, *Modified Spin-Echo Method for Measuring Nuclear Relaxation Times.* Review of Scientific Instruments, 1958. **29**(8): p. 688-691.

14. Gossuin, Y., A. Roch, R.N. Muller, and P. Gillis, *An evaluation of the contributions of diffusion and exchange in relaxation enhancement by MRI contrast agents.* J Magn Reson, 2002. **158**(1-2): p. 36-42.

15. Roch, A., R.N. Muller, and P. Gillis, *Theory of proton relaxation induced by superparamagnetic particles.* Journal of Chemical Physics, 1999. **110**(11): p. 5403-5411.

16. Gillis, P., F. Moiny, and R.A. Brooks, *On T(2)-shortening by strongly magnetized spheres: a partial refocusing model.* Magn Reson Med, 2002. **47**(2): p. 257-63.

17. Wolff, S.D. and R.S. Balaban, *Magnetization transfer contrast (MTC) and tissue water proton relaxation in vivo.* Magn Reson Med, 1989. **10**: p. 135-144.

18. Henkelman, R.M., G.J. Stanisz, and S.J. Graham, *Magnetization transfer in MRI: a review.* NMR Biomed, 2001. **14**(2): p. 57-64.

19. Ward, K.M., A.H. Aletras, and R.S. Balaban, *A new class of contrast agents for MRI based on proton chemical exchange dependent saturation transfer (CEST).* J Magn Reson, 2000. **143**(1): p. 79-87.

20. Bulte, J.W.M. and D.L. Kraitchman, *Iron oxide MR contrast agents for molecular and cellular imaging.* NMR in Biomedicine, 2004. **17**: p. 484-499.

21. Dyal, A., K. Loos, M. Noto, S.W. Chang, C. Spagnoli, K.V. Shafi, A. Ulman, M. Cowman, and R.A. Gross, *Activity of Candida rugosa lipase immobilized on gamma-Fe2O3 magnetic nanoparticles.* J Am Chem Soc, 2003. **125**(7): p. 1684-5.

22. Bulte, J.W., T. Douglas, B. Witwer, S.C. Zhang, E. Strable, B.K. Lewis, H. Zywicke, B. Miller, P. van Gelderen, B.M. Moskowitz, I.D. Duncan, and J.A. Frank, *Magnetodendrimers allow endosomal magnetic labeling and in vivo tracking of stem cells.* Nat Biotechnol, 2001. **19**(12): p. 1141-7.

23. Lewin, M., N. Carlesso, C.H. Tung, X.W. Tang, D. Cory, D.T. Scadden, and R. Weissleder, *Tat peptide-derivatized magnetic nanoparticles allow in vivo tracking and recovery of progenitor cells.* Nat Biotechnol, 2000. **18**(4): p. 410-4.

24. Dressman, D., H. Yan, G. Traverso, K.W. Kinzler, and B. Vogelstein, *Transforming single DNA molecules into fluorescent magnetic particles for detection and enumeration of genetic variations.* Proc Natl Acad Sci U S A, 2003. **100**(15): p. 8817-22.

25. Lanza, G.M., D.R. Abendschein, X. Yu, P.M. Winter, K.K. Karukstis, M.J. Scott, R.W. Fuhrhop, D.E. Scherrer, and S.A. Wickline, *Molecular imaging and targeted drug delivery with a novel, ligand-directed paramagnetic nanoparticle technology.* Acad Radiol, 2002. **9 Suppl 2**: p. S330-1.

26. Butler, J.P. and S.M. Kelly, *A model for cytoplasmic rheology consistent with magnetic twisting cytometry.* Biorheology, 1998. **35**(3): p. 193-209.

27. Wunderbaldinger, P., L. Josephson, and R. Weissleder, *Crosslinked iron oxides (CLIO): a new platform for the development of targeted MR contrast agents.* Acad Radiol, 2002. **9 Suppl 2**: p. S304-6.

28. Shen, T., R. Weissleder, M. Papisov, J. Alexei Bogdanov, and T.J. Brady, *Monocrystalline Iron Oxide Nanocompounds (MION): Physicochemical Properties.* Magnetic Resonance in Medicine, 1993. **29**: p. 599-604.

29. Bulte, J.W.M., R.A. Brooks, B.M. Moskowitz, J. L. H. Bryant, and J.A. Frank, *Relaxometry and Magnetometry of the MR Contrast Agent MION-46L.* Magnetic Resonance in Medicine, 1999. **42**: p. 379-384.

30. Jung, C.W. and P. Jacobs, *Physical and chemical properties of superparamagnetic iron oxide MR contrast agents: ferumoxides, ferumoxtran, ferumoxsil.* Magn Reson Imaging, 1995. **13**(5): p. 661-74.

31. Jung, C.W., *Surface properties of superparamagnetic iron oxide MR contrast agents: ferumoxides, ferumoxtran, ferumoxsil.* Magn Reson Imaging, 1995. **13**(5): p. 675-91.

32. Liu, Q. and Z. Xu, *Self-Assembled Monolayer Coatings on Nanosized Magnetic Particles Using 16-Mercaptohexadecanoic Acid.* Langmuir, 1995. **11**(12): p. 4617-4622.

33. Yee, C., G. Kataby, A. Ulman, T. Prozorov, H. White, A. King, M. Rafailovich, J. Sokolov, and A. Gedanken, *Self-Assembled Monolayers of Alkanesulfonic and -phosphonic Acids on Amorphous Iron Oxide Nanoparticles.* Langmuir, 1999. **15**(21): p. 7111-7115.

34. Harris, L.A., J.D. Goff, A.Y. Carmichael, J.S. Riffle, J.J. Harburn, T.G.S. Pierre, and M. Saunders, *Magnetite Nanoparticle Dispersions Stabilized with Triblock Copolymers.* Chemistry of Materials, 2003. **15**(6): p. 1367-1377.

35. Burke, N.A.D., H.D.H. Stover, and F.P. Dawson, *Magnetic Nanocomposites: Preparation and Characterization of Polymer-Coated Iron Nanoparticles.* Chemistry of Materials, 2002. **14**(11): p. 4752-4761.

36. Santra, S., R. Tapac, N. Theodoropoulou, J. Dobson, A. Hebard, and W. Tan, *Synthesis and Characterization of Silica-Coated Iron Oxide Nanoparticles in Microemulsion: The Effect of Nonionic Surfactants.* Langmuir, 2001. **17**(10): p. 2900-2906.

37. Lu, Y., Y. Yin, B.T. Mayers, and Y. Xia, *Modifying the Surface Properties of Superparamagnetic Iron Oxide Nanoparticles through A Sol-Gel Approach.* Nano Letters, 2002. **2**(3): p. 183-186.

38. Butterworth, M.D., L. Illum, and S.S. Davis, *Preparation of ultrafine silica- and PEG-coated magnetic particles.* Colloids and Surfaces A: Physiochemical and Engineering Aspects, 2001. **179**(1): p. 93-102.

39. Kim, D.K., M. Mikhaylova, Y. Zhang, and M. Muhammed, *Protective Coating of Superparamagnetic Iron Oxide Nanoparticles.* Chemistry of Materials, 2003. **15**(8): p. 1617-1627.

40. Perez, J.M., T. O'Loughin, F.J. Simeone, R. Weissleder, and L. Josephson, *DNA-based magnetic nanoparticle assembly acts as a magnetic relaxation nanoswitch allowing screening of DNA-cleaving agents.* J Am Chem Soc, 2002. **124**(12): p. 2856-7.

41. Nitin, N., L.E. LaConte, O. Zurkiya, X. Hu, and G. Bao, *Functionalization and peptide-based delivery of magnetic nanoparticles as an intracellular MRI contrast agent.* J Biol Inorg Chem, 2004. **9**(6): p. 706-12.

42. Dubertret, B., P. Skourides, D.J. Norris, V. Noireaux, A.H. Brivanlou, and A. Libchaber, *In Vivo Imaging of Quantum Dots Encapsulated in Phospholipid Micelles.* Science, 2002. **298**(5599): p. 1759-1762.

43. Gref, R., P. Couvreur, G. Barratt, and E. Mysiakine, *Surface-engineered nanoparticles for multiple ligand coupling.* Biomaterials, 2003. **24**(24): p. 4529-4537.

44. Perez, J.M., L. Josephson, T. O'Loughlin, D. Hogemann, and R. Weissleder, *Magnetic relaxation switches capable of sensing molecular interactions.* Nat Biotechnol, 2002. **20**(8): p. 816-20.

45. Wang, Y.X., S.M. Hussain, and G.P. Krestin, *Superparamagnetic iron oxide contrast agents: physicochemical characteristics and applications in MR imaging.* Eur Radiol, 2001. **11**(11): p. 2319-31.

46. Josephson, L., C.H. Tung, A. Moore, and R. Weissleder, *High-efficiency intracellular magnetic labeling with novel superparamagnetic-Tat peptide conjugates.* Bioconjug Chem, 1999. **10**(2): p. 186-91.

47. Weisskoff, R.M., C.S. Zuo, J.L. Boxerman, and B.R. Rosen, *Microscopic Susceptibility Variation and Transverse Relaxation: Theory and Experiment.* Magnetic Resonance in Medicine, 1994. **31**: p. 601-610.

48. Hardy, P. and R.M. Henkelman, *On the Transverse Relaxation Rate Enhancement Induced by Diffusion of Spins through Inhomogeneous Fields.* Magnetic Resonance in Medicine, 1991. **17**: p. 348-356.

49. Muller, R.N., P. Gillis, F. Moiny, and A. Roch, *Transverse relaxivity of particulate MRI contrast media: from theories to experiments.* Magn Reson Med, 1991. **22**(2): p. 178-82; discussion 195-6.

50. Gillis, P., F. Moiny, and R.A. Brooks, *On T2-Shortening by Strongly Magnetized Spheres: A Partial Refocusing Model.* Magnetic Resonance in Medicine, 2002. **47**: p. 257-263.

51. Johnsson, M., P. Hansson, and K. Edwards, *Spherical micelles and other self-assembled structures in dilute aqueous mixtures of poly(ethylene glycol) lipids.* Journal of Physcial Chemistry B, 2001. **105**: p. 8420-8430.

52. LaConte, L.E., N. Nitin, O. Zurkiya, D. Caruntu, C.J. O'Connor, X. Hu, and G. Bao, *Coating thickness of magnetic iron oxide nanoparticles affects R2 relaxivity*. 2006, Department of Biomedical Engineering, Georgia Institute of Technology and Emory University.

53. Tscharnuter, W., *Photon Correlation Spectroscopy in Particle Sizing.*, in *Encyclopedia of Analytical Chemistry*, R. Meyers, Editor. 2000, John Wiley & Sons Ltd.: Chichester. p. 5469-5485.

54. Sadeghi, M.M., J.S. Schechner, S. Krassilnikova, A.A. Gharaei, J. Zhang, N. Kirkiles-Smith, A.J. Sinusas, B.L. Zaret, and J.R. Bender, *Vascular cell adhesion molecule-1-targeted detection of endothelial activation in human microvasculature.* Transplant Proc, 2004. **36**(5): p. 1585-91.

55. Saul, J.M., A. Annapragada, J.V. Natarajan, and R.V. Bellamkonda, *Controlled targeting of liposomal doxorubicin via the folate receptor in vitro.* J Control Release, 2003. **92**(1-2): p. 49-67.

56. Kellar, K.E., D.K. Fujii, W.H. Gunther, K. Briley-Saebo, A. Bjornerod, M. Spiller, and S.H. Koenig, *Important considerations in the design of iron oxide nanoparticles as contrast agents for TI-weighted MRI and MRA.* Acad Radiol, 2002. **9 Suppl 1**: p. S34-7.

57. Kellar, K.E., D.K. Fujii, W.H. Gunther, K. Briley-Saebo, A. Bjornerud, M. Spiller, and S.H. Koenig, *NC100150 Injection, a preparation of optimized iron oxide nanoparticles for positive-contrast MR angiography.* J Magn Reson Imaging, 2000. **11**(5): p. 488-94.

58. Gossuin, Y., A. Roch, F. Lo Bue, R.N. Muller, and P. Gillis, *Nuclear magnetic relaxation dispersion of ferritin and ferritin-like magnetic particle solutions: a pH-effect study.* Magn Reson Med, 2001. **46**(3): p. 476-81.

59. Gillis, P. and S.H. Koenig, *Transverse relaxation of solvent protons induced by magnetized spheres: application to ferritin, erythrocytes, and magnetite.* Magn Reson Med, 1987. **5**(4): p. 323-45.

60. Arleth, L., B. Ashok, H. Onyuksel, P. Thiyagarajan, J. Jacob, and R.P. Hjelm, *Detailed structure of hairy mixed micelles formed by phosphatidylcholine and PEGylated phospholipids in aqueous media.* Langmuir, 2005. **21**(8): p. 3279-90.

61. Vergara, A., L. Paduano, V. Vitagliano, and R. Sartorio, *Mutual diffusion in aqueous solution of poly(ethyleneglycol) samples. Some comments on the effect of chain length and polydispersity.* Physical Chemistry Chemical Physics, 1999. **1**(23): p. 5377-5383.

62. Mohs, A.M., Y. Zong, J. Guo, D.L. Parker, and Z.R. Lu, *PEG-g-poly(GdDTPA-co-L-cystine): effect of PEG chain length on in vivo contrast enhancement in MRI.* Biomacromolecules, 2005. **6**(4): p. 2305-11.

63. Elmore, W.C., *The Magnetization of Ferromagnetic Colloids.* Physical Review, 1938. **54**: p. 1092-1095.

64. Josephson, L., J. Lewis, P. Jacobs, P.F. Hahn, and D.D. Stark, *The Effects of Iron Oxides on Proton Relaxivity.* Magnetic Resonance Imaging, 1988. **6**: p. 647-653.

65. Stark, D.D., R. Weissleder, G. Elizondo, P.F. Hahn, S. Saini, L.E. Todd, J. Wittenberg, and J.T. Ferrucci, *Superparamagnetic iron oxide: clinical application as a contrast agent for MR imaging of the liver.* Radiology, 1988. **168**(2): p. 297-301.

66. Weissleder, R., *Liver MR imaging with iron oxides: toward consensus and clinical practice.* Radiology, 1994. **193**(3): p. 593-5.

67. Weissleder, R., J.F. Heautot, B.K. Schaffer, N. Nossiff, M.I. Papisov, A. Bogdanov, Jr., and T.J. Brady, *MR lymphography: study of a high-efficiency lymphotrophic agent.* Radiology, 1994. **191**(1): p. 225-30.

68. Harisinghani, M.G., J. Barentsz, P.F. Hahn, W.M. Deserno, S. Tabatabaei, C.H. van de Kaa, J. de la Rosette, and R. Weissleder, *Noninvasive detection of clinically occult lymph-node metastases in prostate cancer.* N Engl J Med, 2003. **348**(25): p. 2491-9.

69. Seneterre, E., R. Weissleder, D. Jaramillo, P. Reimer, A.S. Lee, T.J. Brady, and J. Wittenberg, *Bone marrow: ultrasmall superparamagnetic iron oxide for MR imaging.* Radiology, 1991. **179**(2): p. 529-33.

70. Bulte, J.W., L.D. Ma, R.L. Magin, R.L. Kamman, C.E. Hulstaert, K.G. Go, T.H. The, and L. de Leij, *Selective MR imaging of labeled human peripheral blood mononuclear cells by liposome mediated incorporation of dextran-magnetite particles.* Magn Reson Med, 1993. **29**(1): p. 32-7.

71. Daldrup-Link, H.E., M. Rudelius, R.A. Oostendorp, M. Settles, G. Piontek, S. Metz, H. Rosenbrock, U. Keller, U. Heinzmann, E.J. Rummeny, J. Schlegel, and T.M. Link, *Targeting of hematopoietic progenitor cells with MR contrast agents.* Radiology, 2003. **228**(3): p. 760-7.

72. Moore, A., L. Josephson, R.M. Bhorade, J.P. Basilion, and R. Weissleder, *Human transferrin receptor gene as a marker gene for MR imaging.* Radiology, 2001. **221**(1): p. 244-50.

73. Ahrens, E.T., M. Feili-Hariri, H. Xu, G. Genove, and P.A. Morel, *Receptor-mediated endocytosis of iron-oxide particles provides efficient labeling of dendritic cells for in vivo MR imaging.* Magn Reson Med, 2003. **49**(6): p. 1006-13.

74. Tyagi, S. and F.R. Kramer, *Molecular beacons: probes that fluoresce upon hybridization.* Nat Biotechnol, 1996. **14**(3): p. 303-8.

75. Seppenwoolde, J.-H., M.A. Viergever, and C.J.G. Bakker, *Passive Tracking Exploiting Local Signal Conservation: The White Marker Phenomenon.* Magnetic Resonance in Medicine, 2003. **50**: p. 784-790.

76. Coristine, A.J., P. Foster, S.C. Deoini, C. Heyn, and B.K. Rutt. *Positive Contrast Labelling of SPIO Loaded Cells in Cell Samples and Spinal Cord Injury*. in *Proc. Intl. Soc. Mag. Reson. Med.* 2004. Kyoto, Japan.

77. Cunningham, C.H., T. Arai, P.C. Yang, M.V. McConnell, J.M. Pauly, and S.M. Conolly, *Positive contrast magnetic resonance imaging of cells labeled with magnetic nanoparticles.* Magn Reson Med, 2005. **53**(5): p. 999-1005.

78. Zimmer, C., S.C. Wright, Jr., R.T. Engelhardt, G.A. Johnson, C. Kramm, X.O. Breakefield, and R. Weissleder, *Tumor cell endocytosis imaging facilitates delineation of the glioma-brain interface.* Exp Neurol, 1997. **143**(1): p. 61-9.

79. Roberts, H.C., T.P. Roberts, S. Ley, W.P. Dillon, and R.C. Brasch, *Quantitative estimation of microvascular permeability in human brain tumors: correlation of dynamic Gd-DTPA-enhanced MR imaging with histopathologic grading.* Acad Radiol, 2002. **9 Suppl 1**: p. S151-5.

80. Gossuin, Y., A. Roch, R.N. Muller, and P. Gillis, *Relaxation induced by ferritin and ferritin-like magnetic particles: the role of proton exchange.* Magn Reson Med, 2000. **43**(2): p. 237-43.

81. Henkelman, R.M., X. Huang, Q.S. Xiang, G.J. Stanisz, S.D. Swanson, and M.J. Bronskill, *Quantitative interpretation of magnetization transfer.* Magn Reson Med, 1993. **29**(6): p. 759-66.

82. Lutsep, H.L., G.W. Albers, A. DeCrespigny, G.N. Kamat, M.P. Marks, and M.E. Moseley, *Clinical utility of diffusion-weighted magnetic resonance imaging in the assessment of ischemic stroke.* Ann Neurol, 1997. **41**(5): p. 574-80.

83. Desprechins, B., T. Stadnik, G. Koerts, W. Shabana, C. Breucq, and M. Osteaux, *Use of diffusion-weighted MR imaging in differential diagnosis between intracerebral necrotic tumors and cerebral abscesses.* AJNR Am J Neuroradiol, 1999. **20**(7): p. 1252-7.

84. Sun, P.Z., P.C. van Zijl, and J. Zhou, *Optimization of the irradiation power in chemical exchange dependent saturation transfer experiments.* J Magn Reson, 2005. **175**(2): p. 193-200.

85. Zurkiya, O. and X. Hu, *Off-resonance saturation as a means of generating contrast with superparamagnetic nanoparticles.* Magn Reson Med, 2006.

86. Blakemore, R., *Magnetotactic bacteria.* Science, 1975. **190**(4212): p. 377-9.

87. Bazylinski, D.A. and R.B. Frankel, *Magnetosome formation in prokaryotes.* Nat Rev Microbiol, 2004. **2**(3): p. 217-30.

88. Auricchio, A., R. Zhou, J.M. Wilson, and J.D. Glickson, *In vivo detection of gene expression in liver by 31P nuclear magnetic resonance spectroscopy employing creatine kinase as a marker gene.* Proc Natl Acad Sci U S A, 2001. **98**(9): p. 5205-10.

89. Kodibagkar, V.D., J. Yu, L. Liu, H.P. Hetherington, and R.P. Mason, *Imaging beta-galactosidase activity using (19)F chemical shift imaging of LacZ gene-reporter molecule 2-fluoro-4-nitrophenol-beta-d-galactopyranoside.* Magn Reson Imaging, 2006. **24**(7): p. 959-62.

90. Louie, A., *Design and characterization of magnetic resonance imaging gene reporters.* Methods Mol Med, 2006. **124**: p. 401-17.

91. Louie, A.Y., M.M. Huber, E.T. Ahrens, U. Rothbacher, R. Moats, R.E. Jacobs, S.E. Fraser, and T.J. Meade, *In vivo visualization of gene expression using magnetic resonance imaging.* Nat Biotechnol, 2000. **18**(3): p. 321-5.

92. Weissleder, R., A. Moore, U. Mahmood, R. Bhorade, H. Benveniste, E.A. Chiocca, and J.P. Basilion, *In vivo magnetic resonance imaging of transgene expression.* Nature Medicine, 2000. **6**(3): p. 351-354.

93. Genove, G., U. DeMarco, H. Xu, W.F. Goins, and E.T. Ahrens, *A new transgene reporter for in vivo magnetic resonance imaging.* Nat Med, 2005. **11**(4): p. 450-4.

94. Gossuin, Y., R.N. Muller, and P. Gillis, *Relaxation induced by ferritin: a better understanding for an improved MRI iron quantification.* NMR Biomed, 2004. **17**(7): p. 427-32.

95. Schuler, D. and R.B. Frankel, *Bacterial magnetosomes: microbiology, biomineralization and biotechnological applications.* Appl Microbiol Biotechnol, 1999. **52**(4): p. 464-73.

96. Nakamura, N., J.G. Burgess, K. Yagiuda, S. Kudo, T. Sakaguchi, and T. Matsunaga, *Detection and removal of Escherichia coli using fluorescein isothiocyanate conjugated monoclonal antibody immobilized on bacterial magnetic particles.* Anal Chem, 1993. **65**(15): p. 2036-9.

97. Nakamura, N., K. Hashimoto, and T. Matsunaga, *Immunoassay method for the determination of immunoglobulin G using bacterial magnetic particles.* Anal Chem, 1991. **63**(3): p. 268-72.

98. Fukuda, Y., Y. Okamura, H. Takeyama, and T. Matsunaga, *Dynamic analysis of a genomic island in Magnetospirillum sp. strain AMB-1 reveals how magnetosome synthesis developed.* FEBS Lett, 2006. **580**(3): p. 801-12.

99. Suzuki, T., Y. Okamura, R.J. Calugay, H. Takeyama, and T. Matsunaga, *Global gene expression analysis of iron-inducible genes in Magnetospirillum magneticum AMB-1.* J Bacteriol, 2006. **188**(6): p. 2275-9.

100. Nakamura, C., J.G. Burgess, K. Sode, and T. Matsunaga, *An iron-regulated gene, magA, encoding an iron transport protein of Magnetospirillum sp. strain AMB-1.* J Biol Chem, 1995. **270**(47): p. 28392-6.

101. Nakamura, C., T. Kikuchi, J.G. Burgess, and T. Matsunaga, *Iron-regulated expression and membrane localization of the magA protein in Magnetospirillum sp. strain AMB-1.* J Biochem (Tokyo), 1995. **118**(1): p. 23-7.

102. Matsunaga, T., Y. Okamura, Y. Fukuda, A.T. Wahyudi, Y. Murase, and H. Takeyama, *Complete Genome Sequence of the Facultative Anaerobic Magnetotactic Bacterium Magnetospirillum sp. strain AMB-1.* DNA Res, 2005. **12**(3): p. 157-66.

103. Scheffel, A., M. Gruska, D. Faivre, A. Linaroudis, J.M. Plitzko, and D. Schuler, *An acidic protein aligns magnetosomes along a filamentous structure in magnetotactic bacteria.* Nature, 2006. **440**(7080): p. 110-4.

104. Komeili, A., Z. Li, D.K. Newman, and G.J. Jensen, *Magnetosomes are cell membrane invaginations organized by the actin-like protein MamK.* Science, 2006. **311**(5758): p. 242-5.

105. Katzmann, D.J., G. Odorizzi, and S.D. Emr, *Receptor downregulation and multivesicular-body sorting.* Nat Rev Mol Cell Biol, 2002. **3**(12): p. 893-905.

106. Raiborg, C., T.E. Rusten, and H. Stenmark, *Protein sorting into multivesicular endosomes.* Current Opinion in Cell Biology, 2003. **15**: p. 446-455.

107. Conrad, M.E., J.N. Umbreit, E.G. Moore, L.N. Hainsworth, M. Porubcin, M.J. Simovich, M.T. Nakada, K. Dolan, and M.D. Garrick, *Separate pathways for cellular uptake of ferric and ferrous iron.* Am J Physiol Gastrointest Liver Physiol, 2000. **279**(4): p. G767-74.

108. Matsunaga, T., Y. Okamura, and T. Tanaka, *Biotechnological application of nano-scale engineered bacterial magnetic particles.* Journal of Materials Chemistry, 2004. **14**: p. 2099-2105.

109. Weissleder, R., A. Moore, U. Mahmood, R. Bhorade, H. Benveniste, E.A. Chiocca, and J.P. Basilion, *In vivo magnetic resonance imaging of transgene expression.* Nat Med, 2000. **6**(3): p. 351-5.